AN EXPLORATION OF NUMERICAL APPROACHES TO BOLTZMANN
EQUATION REGARDING HYDRODYNAMICS

A THESIS SUBMITTED TO
THE GRADUATE SCHOOL OF NATURAL AND APPLIED SCIENCES
OF
MIDDLE EAST TECHNICAL UNIVERSITY

BY

ALPER ŞAHIN

IN PARTIAL FULFILLMENT OF THE REQUIREMENTS
FOR
THE DEGREE OF MASTER OF SCIENCE
IN
ENGINEERING SCIENCES

SEPTEMBER 2019

Approval of the thesis:

AN EXPLORATION OF NUMERICAL APPROACHES TO BOLTZMANN EQUATION REGARDING HYDRODYNAMICS

submitted by **ALPER ŞAHIN** in partial fulfillment of the requirements for the degree of **Master of Science in Engineering Sciences Department, Middle East Technical University** by,

Prof. Dr. Halil Kalıpçılar
Dean, Graduate School of **Natural and Applied Sciences** _____

Prof. Dr. Murat Dicleli
Head of Department, **Engineering Sciences** _____

Prof. Dr. Hakan Işık Tarman
Supervisor, **Mechanical Engineering, METU** _____

Examining Committee Members:

Prof. Dr. Yusuf Özyörük
Aerospace Engineering, METU _____

Prof. Dr. Hakan Işık Tarman
Mechanical Engineering, METU _____

Assoc. Prof. Dr. Utku Kanoğlu
Aerospace Engineering, METU _____

Assoc. Prof. Dr. Cüneyt Sert
Mechanical Engineering, METU _____

Assist. Prof. Dr. Sıtkı Uslu
Mechanical Engineering, TOBB-ETU _____

Date: 18.09.2019

I hereby declare that all information in this document has been obtained and presented in accordance with academic rules and ethical conduct. I also declare that, as required by these rules and conduct, I have fully cited and referenced all material and results that are not original to this work.

Name, Surname: Alper Şahin

Signature:

ABSTRACT

AN EXPLORATION OF NUMERICAL APPROACHES TO BOLTZMANN EQUATION REGARDING HYDRODYNAMICS

Şahin, Alper
Master of Science, Engineering Sciences
Supervisor: Prof. Dr. Hakan Işık Tarman

September 2019, 111 pages

The Lattice Boltzmann Method (LBM) has become an alternative tool in computational fluid dynamics (CFD) techniques. While traditional CFD methods are based on Navier-Stokes equations that describe the fluid in terms of macroscopic quantities, LBM takes a mesoscopic description of the fluid thus closing the gap between macroscale and microscale. Overall, LBM provides a simple and efficient framework for simulation of fluid flows. In this approach, Boltzmann kinetic equation with BGK collision operator is discretized over a square lattice and solved to compute the evolution of a particle distribution function whose velocity moments are connected to the macroscopic primitive variables such as velocity and density.

In this study, we explore two main approaches in the velocity discretization of the Boltzmann equation, namely, Galerkin and Collocation approaches. The foundations leading to these approaches are systematically laid down and some numerical examples are presented. These examples include, plane channel (Poiseuille), flow over circular and square cylinders and flow over an array of cylinders. Comparisons with available analytic and other numerical techniques show a satisfactory agreement.

ÖZ

BOLTZMANN DENKLEMINE SAYISAL YAKLAŞIMLARIN HİDRODİNAMİK AÇIDAN BİR İNCELEMESİ

Şahin, Alper
Yüksek Lisans, Mühendislik Bilimleri
Tez Danışmanı: Prof. Dr. Hakan Işık Tarman

Eylül 2019, 111 sayfa

Lattice Boltzmann Yöntemi (LBY), Hesaplamalı Akışkanlar Dinamiği (HAD) yöntemlerinde alternatif bir araç haline gelmiştir. Geleneksel HAD metotları, akışkanı makroskopik büyüklükler olarak tanımlayan Navier-Stokes denklemlerine dayanırken, LBY, akışkanı mesoskopik tanımıyla ele alır, böylelikle bu durum makro ve mikro ölçek arasındaki boşluğu kapatmaktadır. Genel olarak LBY, akışkan akışı simülasyonları için basit ve verimli bir çerçeve çizmektedir. Bu yaklaşımda, BGK çarpışma operatörüyle Boltzmann kinetik denklemi, kare kafes üzerinde ayrıştırılır ve hız momentleri, hız ve yoğunluk gibi makroskobik ilkel değişkenlere bağlı olan bir parçacık dağılım fonksiyonunun gelişimini hesaplamak için çözülür.

Bu çalışmada, Boltzmann denklemindeki hız ayrıklaştırılması, Galerkin ve Kollokasyon yaklaşımı olmak üzere, iki ana yaklaşım ile araştırılmıştır. Bu yaklaşımlara yol açan temeller sistematik olarak masaya yatırılmış ve bir takım sayısal örnekler sunulmuştur. Bu örnekler, kanal akışı (Poiseuille), dairesel ve kare silindirler üzerindeki akış ile silindir dizilimleri üzerindeki akışları içermektedir. Mevcut analitik ve diğer sayısal yöntemler ile yapılan karşılaştırmalar tatmin edici bir uyuşma göstermektedir.

Anahtar Kelimeler: Lattice Boltzmann Yöntemi, Galerkin ve Kollokasyon yaklaşımı, Hesaplamalı Akışkanlar Dinamiği, kanal akışı, silinidir(ler)

To my aunt, who died at an early age, for all the love that she showed me that little
time..

ACKNOWLEDGEMENTS

TABLE OF CONTENTS

LIST OF TABLES

LIST OF FIGURES

FIGURES

LIST OF SYMBOLS

SYMBOLS

L	length scale
U	velocity scale
t_{conv}	time scale of convection
t_{diff}	time scale of diffusion
ν	kinematic viscosity
Re	Reynolds number
c_s	speed of sound
t_{sound}	time scale of sound
Ma	Mach number
$\vec{r}_i$	position vector of the ith molecule
m	mass of the fluid
$\vec{F}_i$	total force experienced by the molecule
Q	macroscopic quantities
q	microscopic quantities
l	characterizing scale of length
v_T	thermal velocity
k_B	Boltzmann constant
T	temperature
l_{mfp}	characterizing length scale in the mean free path
Kn	Knudsen number
n_i	Boolean number of particles
$\boldsymbol{v}_i$	discrete velocity
$\boldsymbol{x}$	position of the molecule
C_i	collision operator

f	probability distribution function
$\boldsymbol{v}$	velocity
t	time
$\boldsymbol{F}$	force
$\boldsymbol{a}$	acceleration
dt	time interval
C_{BGK}	BGK collision operator
τ	relaxation parameter
f^{eq}	equilibrium (Maxwellian) distribution
ν	viscosity
Pr	Prandtl number
$\boldsymbol{v}_{\alpha}$	discrete set of velocities
ϖ_{α}	weights
$H^{(n)}$	Hermite polynomials
$\omega(x)$	Gaussian exponential weight
p	pressure
$\boldsymbol{u}$	mean velocity
P_{ij}	pressure tensor
σ_{ij}	stress tensor
l_0	characteristic length
t_0	characteristic time
T_0	characteristic temperature
$\boldsymbol{a}^{(n)}(\boldsymbol{x},t)$	expansion coefficients
f^N	truncated representation of the distribution function
$\boldsymbol{U}$	Hermite coefficient vector
$\boldsymbol{A}$	spatial differential operation matrix
$\boldsymbol{B}$	spatial differential operation matrix
$\boldsymbol{N}$	nonlinear (collision) terms

$\boldsymbol{P}$	matrix of the eigenvectors
$\Lambda^{+/-}$	diagonal matrices
Δt	time step size
Δx	spatial step size
a, b, c, d	lattice constants
$\boldsymbol{\nabla}_i$	gradient operator
$\bar{\boldsymbol{\alpha}}$	direction index
$\boldsymbol{u}_w$	wall moving velocity
ρ_w	local fluid density
H	height of the lattice
U_∞	free-stream velocity
D	cylinder diameter
St	Strouhal number
f_s	vortex shedding frequency
C_D	drag coefficient
C_L	lift coefficient
F_x	total forces on the surface of the cylinder along the flow direction
F_y	force on the surface of the cylinder perpendicular to the flow direction

CHAPTER 1

INTRODUCTION

The mathematical models of fluid dynamics are mainly based on the conservation of mass, momentum and energy resulting in the continuity, Navier-Stokes and energy equations. This constitutes the so-called continuum approach where the macroscopic primitive quantities such as velocity, temperature, pressure, are assumed to vary continuously throughout the physical domain. The scale is macroscopic and may be characterized by a length scale L and a velocity scale U. Two different phenomena shape the macroscopic dynamics, namely, convection that occurs in the time scale $t_{conv} = L/U$ and diffusion that occurs in the time scale $t_{diff} = L^2/\nu$ where ν is the kinematic viscosity. Relative importance of these time scales give rise to the well-known Reynolds number $Re = t_{diff}/t_{conv} = UL/\nu$ that characterizes the dynamics of the macroscopic flow, as high Re flow, such as turbulence, and low Re flow, such as bioflows. Another characterizing macroscopic scale is the speed of sound c_s that gives rise to the time scale $t_{sound} = L/c_s$ determining how fast acoustic waves propagate in the fluid. When compared with the convective time scale gives rise to the Mach number $Ma = t_{sound}/t_{conv} = U/c_s$. Steady flow with $Ma \leq 0.3$ is considered to be incompressible.

The fact that the matter is made-up of individual molecules, on the other hand, forms the basis for an alternative representation of a fluid in the atomic level. The mathematical models in this finer description are based on the Newton's equation of motion $m\ddot{\vec{r}}_i = \vec{F}_i$ where m is the mass of the fluid molecule, $\vec{r}_i$ is the position vector of the ith molecule, and $\vec{F}_i$ is the total force experienced by the molecule. A molecular dynamics (MD) simulation (Mohamad, 2011) consists of solving these equations to

1

determine the position and the velocity of each molecule. The macroscopic quantities Q are then obtained from the microscopic quantities q by the ensemble averaging procedure: $Q = \langle q \rangle$. However, tracking the evolution of the molecules even for a small volume of fluid ($\sim 10^{23}$) in the six dimensional phase space consisting of the spatial coordinates and the velocities is impractical and it is limited to sub-micrometer systems only. The scale here is microscopic. The characterizing scales may be the size of the fluid atom or molecule l and the average thermal velocity $v_T = (k_B T/m)^{1/2}$ with Boltzmann constant k_B, and the temperature T. Note that $v_T \gg U$.

Mesoscopic description is then a viable option that lies between the macroscopic and the microscopic scales. The mathematical models in this description are developed based on the kinetic theory that tracks the evolution of its constituent molecules' distributions in the six dimensional phase space. A characterizing length scale in this description is the mean free path l_{mfp}, $l \ll l_{mfp} \ll L$, which is the distance travelled between two successive collisions. The mean time between successive collisions is then $t_{mfp} = l_{mfp}/v_T$. Kinetic theory in principle is restricted to the case of a dilute gas which the molecules spend little time colliding and collisions occur one-on-one basis. These exclude dense gases and liquids where the molecules are closer and constantly interact. Since the molecular radius is neglected in this description, collisions involving more than two particles are events that occur with probability zero, and therefore can be neglected for all practical purposes. In this context, a useful parameter is the Knudsen number, $Kn = l_{mfp}/L$ that is the ratio between the mesoscopic and macroscopic length scales. For $Kn \ll 1$, the continuum description is valid while for $Kn \sim 1$, kinetic theory description becomes valid. The von Karman relation states that Knudsen and Mach numbers are related by $Kn \propto Ma/Re$.

Figure 1.1 shows a general geometry schematic of a hybrid scheme. Velocity gradients, which are small gradients, are placed in shadowed region and continuum

equations are solved in that region. In dotted region, atomistic description is used in large gradients. In below figure, from C to P, for molecular dynamic simulations, boundary conditions ensured by continuum solutions. From P to C, for continuum simulations, boundary conditions ensured by atomistic solutions (Nie et al., 2004).
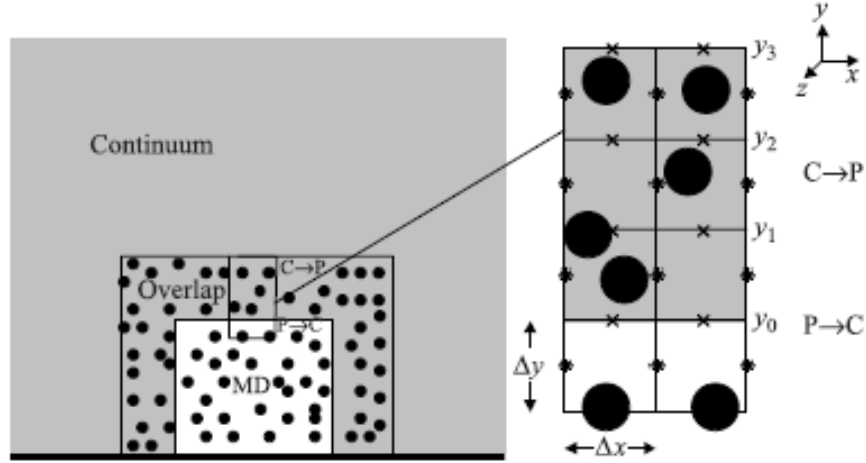
Figure 1.1. Schematic of the hybrid method. (Nie et al., 2004)

The use of mesoscopic methods as an alternative tool for computational fluid dynamics (CFD) was started in 1980s with the lattice-gas methods. The basic idea is building a simplified kinetic model based on mesoscopic and microscopic process fundamentals. The conventional methods of macroscopic dynamics are insufficient for understanding the microscopic physics in details. By using mesoscopic methods, however, one can analyse dynamics of the macroscopic fluid flows behaviour as if many microscopic particles are in the system (Kadanoff, 1986). Solving complex kinetic equations and tracking all of the particles in MD simulations become easier by development of the kinetic equation simplification. The advantages of molecular dynamics such as simple implementation of the boundary conditions and definite physical models with fully parallel algorithms provided by kinetic equation. (S. Chen et al., 1998). Besides providing microscopic dynamics at interfaces between fluids and

3

fluid to solids in feasible ways, this method can work as a solver for the Navier–Stokes equation like conservation equations in the bulk flow (L. Chen et al., 2014).

Over the last few years, the interest in discrete mesoscopic CFD methods was increased. One can include lattice gas automata (LGA), and the lattice Boltzmann method (LBM) into this context. These methods have the advantages of molecular dynamics in modelling fluids as discrete particles, thus, allowing the microscopic physics responsible for many complex fluid phenomena to be modelled fundamentally. Nevertheless LBM is building on a particle model with averaged macroscopic physical behaviour. In addition, they can be easily implemented on computational algorithms and the simulations can be performed with more efficiency and speed (Yepez, 1993). However these methods still have lots of rooms for improvements, because they are relatively new compared to the conventional methods (Gergova, 2002).

1.1. Lattice Gas Automaton

The basic idea goes back to von Neumann (von Neumann, 1966) who developed the cellular automaton (CA) as an idealization of a physical system in which space and time are discrete. In this idealization, the physical quantities take only a finite set of values over regular rectangular or triangular lattices that form the cells. In discretized space, each linked lattice nodes have local state variables and significant rules of updating. The automata are described in terms of configurations and transition concepts. In configuration rule of a system, all nodes have a designation of their states in cellular space. Configuration dynamics are achieved by transition rules. For configuration rules, particles are designated to the nodes and the transition rules are considerably easy and finite (Lim, 1990). Out of the sum of these transition rules emerges a collective complex behaviour that are not obviously extrapolated from the individual rules.

In early lattice-gas automaton (LGA) models, the fluid is treated as a set of particles residing on the nodes in a two-dimensional square lattice and allowed to move along the lattice lines to any of the four nearest neighbouring nodes. The collision between particles are designed to follow head-on rule that the colliding two particles will turn around 90° after the collision (He et al., 1997). Mathematically, the motion in this model can be described by the discrete kinetic equations:

$$n_i(\boldsymbol{x} + \boldsymbol{v}_i, t + 1) = n_i(\boldsymbol{x}, t) + C_i \tag{1.1}$$

where $n_i(\boldsymbol{x}, t)$ is the Boolean number of particles,

$$n_i(\boldsymbol{x}, t) = \begin{cases} 0 & \text{particle absence at node } \boldsymbol{x} \text{ and time } t \\ 1 & \text{particle presence at node } \boldsymbol{x} \text{ and time } t \end{cases}$$

moving with discrete velocity $\boldsymbol{v}_i$ at node $\boldsymbol{x}$ to its adjacent sites and C_i is the collision operator representing the influence of particle collisions (Koda, 2013). The insufficient symmetry of the square lattice was discovered to restrict LGA to be a computational model for hydrodynamic flows. This led researchers (Frisch et al., 1986; Wolfram, 1986) to introduce their hexagonal model known as FHP model. This model uses a triangular lattice on which each node has six nearest neighbours. Consequently, FHP collision rule includes more cases. The implementation of FHP involves two operations, streaming and collision. In streaming operation, all particles move through the lattice to a neighbouring site in the velocity direction. In collision operation, these particles interact and scatter when they reach at their lattice sites (S. Chen et al., 1998).

The main drawback of LGA is its noisy nature in simulating hydrodynamics. This limited its success and led to the discovery that instead of discrete particles, modelling based on an advecting number density distribution eliminated the noisiness of the method and allowed implementation of a more general collision operator in LBM. By recovering the Navier-Stokes equation using Chapman-Enskog expansion (H. Chen et al., 1992), LBM has become an alternative tool especially for complex CFD problems such as multi-component, multi-phase flows (Higuera et al., 1989) and physiological

problems such as cardiovascular flows and flow in lungs and in breathing passages (Xia et al., 2002). However, earlier LBM had not been known as a CFD tool in engineering community (Qian et al., 1992) due to its restriction to regular lattices (Amati et al., 1997) that was inherited from the original LGA (Frisch et al., 1986). Due to its use of number density distribution in LBM, replacing the Boolean population of LGA, this restriction has become unnecessary in LBM (Cao et al., 1997; He et al., 1996).

1.2. Lattice Boltzmann Equation

LBM originates from the LGA model and at its heart lies the probability distribution function $f(x, v, t)$ that gives the probability of finding a molecule at position x with a velocity v at a time t or the expected number of particles $f(x, v, t)dxdv$ in a phase space volume element $dxdv$ (Sukop et al., 2006). The distribution function is connected to macroscopic variables such as the mass density

$$\rho(x, t) = \int f(x, v, t)\, dv, \tag{1.2a}$$

the momentum density

$$\rho(x, t)u(x, t) = \int v\, f(x, v, t)\, dv, \tag{1.2b}$$

and the total energy density

$$\rho(x, t)E(x, t) = \frac{1}{2}\int |v|^2\, f(x, v, t)\, dv. \tag{1.2c}$$

These are actually moment integrals of f weighted with some functions of v and integrated over the velocity space. The considerations of the internal energy due to the random motion of the particles lead to the macroscopic internal energy density as the moment

$$\rho(x, t)e(x, t) = \frac{1}{2}\int |v - u|^2\, f(x, v, t)\, dv. \tag{1.2d}$$

In the presence of an external force $\boldsymbol{F}$, the particles in this distribution will be accelerated by $\boldsymbol{a}$. If we follow the movements of particles in a phase space volume element during a time interval dt, the number of particles is conserved, thus

$$f(\boldsymbol{x} + \boldsymbol{v}dt, \boldsymbol{v} + \boldsymbol{a}dt, t + dt)d\boldsymbol{x}d\boldsymbol{v} = f(\boldsymbol{x}, \boldsymbol{v}, t)d\boldsymbol{x}d\boldsymbol{v} \qquad (1.3)$$
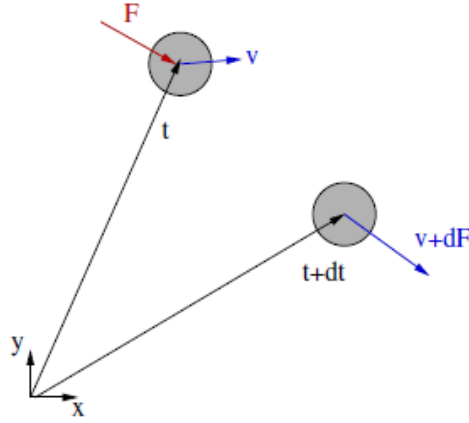
Figure 1.2. Effect of an external force $\boldsymbol{F} = m\boldsymbol{a}$ on velocity where m is the molecular mass. (Boix, 2013)

The intermolecular collisions taking place within a gas, however, cause changes to the distribution whose effect is summed up by the collision operator $C(f)$ leading to a more realistic equation:

$$f(\boldsymbol{x} + \boldsymbol{v}dt, \boldsymbol{v} + \boldsymbol{a}dt, t + dt)d\boldsymbol{x}d\boldsymbol{v} - f(\boldsymbol{x}, \boldsymbol{v}, t)d\boldsymbol{x}d\boldsymbol{v} = C(f)d\boldsymbol{x}d\boldsymbol{v}dt. \quad (1.4)$$

In the limit $dt \rightarrow 0$, it reduces to the classical Boltzmann equation (Succi 2001):

$$\frac{\partial f}{\partial t} + \boldsymbol{v} \cdot \nabla_x f + \boldsymbol{a} \cdot \nabla_v f = C(f). \qquad (1.5)$$

The last two terms on the left-hand side of (1.5) represent the net number of particles entering the infinitesimal phase-space volume $d\boldsymbol{x}d\boldsymbol{v}$ centered at $(\boldsymbol{x}, \boldsymbol{v})$ as the result of inertial motion of particles between collisions and the external force **F,** respectively, while the second term on the right-hand side represents the net number of particles

entering that same volume as the result of instantaneous and purely local collisions. The collision operator must fulfil the conservation of the mass

$$\int C(f)d\boldsymbol{v} = 0 \tag{1.6a}$$

the total momentum

$$\int \boldsymbol{v}\, C(f)d\boldsymbol{v} = 0 \tag{1.6b}$$

and the total energy conditions

$$\int \boldsymbol{v} \cdot \boldsymbol{v}\, C(f)d\boldsymbol{v} = 0 \tag{1.6c}$$

due to the assumption that the collisions do not create nor destroy molecules. The general Boltzmann collision operator is rather complicated and the collision operator used in the LBM is based on much simpler BGK collision operator (Bhatnagar et al., 1954)

$$C_{BGK}(f) = -\frac{f - f^{eq}}{\tau} \tag{1.7}$$

where τ is the relaxation parameter towards the equilibrium (Maxwellian) distribution

$$f^{eq} = \rho \left(\frac{1}{2\pi RT}\right)^{3/2} exp\left(-\frac{|\boldsymbol{v} - \boldsymbol{u}|^2}{2RT}\right) \tag{1.8}$$

with the specific gas constant R and density ρ. The relaxation parameter τ is closely related to the viscosity v. BGK collision operator satisfies the conservation requirements (1.6) and facilitates the evolution of f towards f^{eq} as governed by the relaxation parameter τ. However it is still an approximation to Boltzmann's original collision operator in that BGK collision operator predicts a Prandtl number ($Pr = \kappa/v$, the ratio of viscous v and thermal κ diffusivity coefficients) of $Pr = 1$ while the original operator predicts $Pr \approx 2/3$, a value validated experimentally for monatomic gases.

The Boltzmann equation is a continuous equation and it is necessary to construct corresponding discrete equations for computational modelling. The first step in the discretization process involves the discretization of the moment equations (1.2) in the velocity space:

$$\int f(\boldsymbol{x}, \boldsymbol{v}, t) \, d\boldsymbol{v} \cong \sum_{\alpha} \varpi_\alpha f(\boldsymbol{x}, \boldsymbol{v}_\alpha, t), \qquad (1.9a)$$

$$\int \boldsymbol{v} \, f(\boldsymbol{x}, \boldsymbol{v}, t) \, d\boldsymbol{v} \cong \sum_{\alpha} \varpi_\alpha \boldsymbol{v}_\alpha f(\boldsymbol{x}, \boldsymbol{v}_\alpha, t), \qquad (1.9b)$$

$$\frac{1}{2}\int |\boldsymbol{v}|^2 \, f(\boldsymbol{x}, \boldsymbol{v}, t) \, d\boldsymbol{v} \cong \frac{1}{2}\sum_{\alpha} \varpi_\alpha |\boldsymbol{v}_\alpha|^2 f(\boldsymbol{x}, \boldsymbol{v}_\alpha, t), \qquad (1.9c)$$

where $\{\boldsymbol{v}_\alpha\}$ is a discrete set of velocities and ϖ_α are the corresponding weights. This is introduced into the Boltzmann equation (1.5) with the BGK collision operator (1.7) to get (BGK-Boltzmann)

$$\frac{\partial f_\alpha}{\partial t} + \boldsymbol{v}_\alpha \cdot \nabla_x f_\alpha = -\frac{1}{\tau}(f_\alpha - f_\alpha^{eq}) \qquad (1.10)$$

where $f_\alpha = f(\boldsymbol{x}, \boldsymbol{v}_\alpha, t)$ and the external force is omitted. This decouples the velocity space and the physical space and the resulting equation is called the continuous Lattice Boltzmann Equation (LBE). The discretization in the physical space (time and space) can be performed by different numerical techniques, such as the finite difference (He et al., 1996), finite volume (Xi et al., 1999), finite element methods (Li et al., 2005).

Discretization of (1.10) in space and time with finite difference formulas leads to the (discrete) lattice Boltzmann equation:

$$f_\alpha(\boldsymbol{x} + \boldsymbol{v}_\alpha \Delta t, t + \Delta t) - f_\alpha(\boldsymbol{x}, t) \qquad (1.11)$$
$$= -\frac{\Delta t}{\tau}(f_\alpha(\boldsymbol{x}, t) - f_\alpha^{eq}(\boldsymbol{x}, t)).$$

This form is widely used as a computational tool for the simulation of fluid flow. The evolution of the distribution function is approximated over a lattice having each lattice

site located at $\boldsymbol{x}$ and connected to the neighbouring lattice sites along the directions $\boldsymbol{v}_\alpha$. The implementation takes successive streaming (propagation) and collision (relaxation) substeps.

An alternative approach is to use a Galerkin procedure based on Hermite polynomial expansion in velocity space (Tölke et al., 2000). The equilibrium distribution function f^{eq} is of Gaussian exponential form, thus, it can be expressed in terms of Hermite polynomials $\{H^{(n)}(x)\}$ that are orthogonal under a weighted inner product

$$\int_{-\infty}^{\infty} H^{(n)}(x) H^{(m)}(x)\, \omega(x) dx = n!\, \delta_{nm} \tag{1.12}$$

with Gaussian exponential weight $\omega(x) = \frac{1}{\sqrt{2\pi}}\exp(-x^2/2)$. This can also be applied to the unknown distribution function f itself:

$$f(\boldsymbol{x}, \boldsymbol{v}, t) \cong \omega(\boldsymbol{v}) \sum_{n=0}^{N} \frac{1}{n!} a^{(n)}(\boldsymbol{x}, t) H^{(n)}(\boldsymbol{v}) \tag{1.13}$$

where the expansion coefficients can be obtained by Galerkin projection onto the space spanned by the Hermite polynomials as

$$a^{(n)}(\boldsymbol{x}, t) = \int_{-\infty}^{\infty} f(\boldsymbol{x}, \boldsymbol{v}, t)\, H^{(n)}(\boldsymbol{v})\, d\boldsymbol{v} \tag{1.14}$$

It turns out that the discrete set of velocities $\{\boldsymbol{v}_\alpha\}$ used in LBM are, in fact, the Gaussian-Hermite quadrature nodes. The Galerkin projection when applied to the residual resulting from substituting the truncated representations of f and f^{eq} yields a system of hyperbolic partial differential equations that can be solved with available numerical techniques free of a lattice structure.

10

1.3. Thesis Objectives

In this thesis, our objective is to explore the collocation and Galerkin projection approaches to numerically solve the Boltzmann equation with the BGK collision operator. The physical configurations of Plane Poiseuille flow will be used as the test problems. In addition, flow past circular cylinder(s) and a square cylinder configurations are simulated by LBM. The explorations are performed to understand the theory and the implementation of this promising alternative technique for computational modelling of the fluid flow phenomena.

After the perspective introduction to the analytics and numerics of LBM in Chapter1, Chapter 2 presents the Boltzmann equation from the kinetic theory to its discretization in Galerkin and collocation approaches. In Chapter 3, Galerkin approach is presented in detail and implemented numerically to solve planar Poiseuille flow whose analytic solution is known. Collocation approach leading to LBM is presented in Chapter 4. The implementation issues, namely boundary conditions and stability, on the square lattice are discussed and planar Poiseuille flow is used as a numerical test case. Some further numerical examples, such as flow over circular, square and an array of cylinders are presented in Chapter 5. It is finalized by a discussion in Chapter 6. Hermite polynomials and Gauss-Hermite quadrature that are the main tools used in Galerkin and collocation approaches, are presented in the Appendix.

CHAPTER 2

BOLTZMANN EQUATION AND ITS DISCRETIZATION

As mentioned in the introduction LBM operates in the mesoscopic scales of l_{mfp}, t_{mfp} based on the mean free path between successive collisions. Kinetic theory commonly provides a kinetic description of dilute monatomic gases at this scale, thus it underlies the LBM.

2.1. Kinetic Theory and the Equilibrium Distribution Function

In the mesoscopic description, the particle distribution function $f(\boldsymbol{x}, \boldsymbol{v}, t)$ is the fundamental variable representing the density of particles in the phase space with the velocity $\boldsymbol{v} = (v_x, v_y, v_z) = (v_1, v_2, v_3)$ at position $\boldsymbol{x} = (x, y, z) = (x_1, x_2, x_3)$ and time t. It can be considered as a generalization of macroscopic density $\rho(\boldsymbol{x}, t)$. It is, in fact, connected to macroscopic variables like the density and the fluid velocity $\boldsymbol{u}(\boldsymbol{x}, t)$ from its moments over the velocity space (1.2). Using the ideal gas law $p = \rho RT$ and the internal energy $\rho e = \frac{3}{2} \rho RT$ due to the molecular translation in three spatial dimensions, both pressure p and temperature T can also be formulated as a moment

$$p = \rho RT = \frac{2}{3} \rho e = \frac{1}{3} \int |\boldsymbol{v} - \boldsymbol{u}|^2 \, f(\boldsymbol{x}, \boldsymbol{v}, t) \, d\boldsymbol{v} \qquad (2.1)$$

When a gas has been left alone for sufficiently long, the collisions between molecules tend to even out the distribution of particle velocities in a gas around the mean velocity $\boldsymbol{u}$, thus, the distribution function $f(\boldsymbol{x}, \boldsymbol{v}, t)$ reaches an equilibrium distribution $f^{eq}(\boldsymbol{c})$ where $\boldsymbol{c} = \boldsymbol{v} - \boldsymbol{u} = (c_x, c_y, c_z)$ is the relative (intrinsic) velocity and f^{eq} should be

only a function of the speed $|c| = c$ of the particles, thus $f^{eq}(c)$. Together with the independence of the distribution in each direction, this implies

$$f^{eq}(c) = f^{eq}(c_x)f^{eq}(c_y)f^{eq}(c_z) = \Phi(c_x^2 + c_y^2 + c_z^2)$$

for some function Φ where only the velocity dependence is shown. An appropriate form of the distribution function should then be $f^{eq}(c) = A\exp(-Bc^2)$ so that

$$f^{eq}(c) = A^3 \exp\left(-B(c_x^2 + c_y^2 + c_z^2)\right) = A^3 \exp(-Bc^2).$$

The number of particles having speed between c and $c + dc$ can be considered geometrically as lying between two shells of the sphere with radii c and $c + dc$ having a volume $4\pi c^2 dc$. Therefore, the probability distribution is

$$f^{eq}(c)d\boldsymbol{c} = A^3 \exp(-Bc^2) \, 4\pi c^2 dc \tag{2.2}$$

Substituting this expression in

$$\rho RT = \frac{2}{3}\rho e = \frac{1}{3}\int c^2 f^{eq}(c)d\boldsymbol{c}$$

and using the fact that $\rho = \int f^{eq}(c) \, d\boldsymbol{c}$, we get

$$f^{eq} = \rho \left(\frac{1}{2\pi RT}\right)^{3/2} exp\left(-\frac{c^2}{2RT}\right) \tag{2.3}$$

This is Maxwell's derivation that is later re-derived by Boltzmann by using statistical mechanics arguments. It is therefore called Maxwell-Boltzmann equilibrium distribution. It can be verified that $\boldsymbol{f^{eq}}$ satisfies the moment integrals (1.2) as $\boldsymbol{f}$.

2.2. The Boltzmann Equation and Macroscopic Conservation Equations

The classical Boltzmann equation (1.5) is actually an advection equation. While terms on left hand side represent the distribution function f being advected with the velocity $\boldsymbol{v}$ under the forces affecting this velocity, the source term $C(f)$ on the right hand side represents the local redistribution of f due to two-body collisions, thus, $C(f) \equiv$

14

$Q(f, f)$ is a bilinear quantity. It models all possible outcomes of two-particle collisions and is of the form of a complicated quadratically nonlinear integral over the velocity space.

The replacement of the collision operator by a simpler but high fidelity expression is the key factor in facilitating the numerical approaches to the Boltzmann equation. BGK collision operator (1.7) proved very useful in this respect that (a) it conserves the collision invariants (1.6) as expected from a collision operator because the collisions are assumed not to create nor destroy molecules and (b) it captures the relaxation of f towards the equilibrium distribution f^{eq}, i.e. $C_{BGK}(f^{eq}) = 0$ as stated by Boltzmann's H-theorem. The collisional relaxation towards f^{eq} is determined by the relaxation parameter τ. It, in fact, embodies a whole spectrum of relaxation scales lumped as a single value (Succi 2001). It might look like an oversimplification of the collision process, however, $C_{BGK}(f)$ carries the nonlinearity of the classical operator $C(f)$ because f^{eq} depends nonlinearly on the fluid speed $\boldsymbol{u}$, the temperature T which are linear functionals (1.2) of f.

Classically, the link between mesoscopic Boltzmann kinetics and macroscopic conservation equations (Navier-Stokes equations) was shown by the Chapman-Enskog analysis (S. Chen et al., 1998); (Frisch et al., 1986) based on the asymptotic expansions with the expansion parameter ϵ recognized as Knudsen number, thus providing a derivation valid for low Knudsen number (or low Mach number). This subject will further be taken up in Chapter 4.

Alternatively, macroscopic conservation equations can be constructed by taking velocity moments of the BGK-Boltzmann equation

$$\frac{\partial f}{\partial t} + v_i \frac{\partial f}{\partial x_i} = \frac{1}{\tau} (f^{eq} - f) \tag{2.4}$$

where the zeroth, first and second velocity moments lead to the macroscopic conservation equations for mass, momentum and energy, respectively. In fact, the

moment integrals lead to vanishing right-hand side of (2.4) due to (1.6). The zeroth moment of (2.4) is

$$\int \left\{ \frac{\partial f}{\partial t} + v_i \frac{\partial f}{\partial x_i} \right\} d\boldsymbol{v} = \int \left\{ \frac{1}{\tau}(f^{eq} - f) \right\} d\boldsymbol{v}. \tag{2.5}$$

In the phase space, the variables $(\boldsymbol{x}, \boldsymbol{v}, t)$ are independent, so the temporal and spatial derivatives commute with the velocity integral and f vanishes sufficiently fast as $|\boldsymbol{v}| \to \infty$. Thus, it can be shown using (1.2a) that (2.4) yields the continuity equation

$$\frac{\partial \rho}{\partial t} + \frac{\partial(\rho u_i)}{\partial x_i} = 0. \tag{2.6}$$

The first moment of (2.4)

$$\int v_j \left\{ \frac{\partial f}{\partial t} + v_i \frac{\partial f}{\partial x_i} \right\} d\boldsymbol{v} = \int v_j \left\{ \frac{1}{\tau}(f^{eq} - f) \right\} d\boldsymbol{v} \tag{2.7}$$

can be rearranged by using $v_i v_j = (v_i - u_i)(v_j - u_j) + v_i u_j + v_j u_i - u_i u_j$ and

$$\frac{\partial}{\partial x_i} \int v_i v_j f d\boldsymbol{v} = \frac{\partial}{\partial x_i} \underbrace{\int (v_i - u_i)(v_j - u_j) f d\boldsymbol{v}}_{P_{ij}} + \frac{\partial}{\partial x_i} \underbrace{\int (v_i u_j + v_j u_i - u_i u_j) f d\boldsymbol{v}}_{\rho u_i u_j}$$

to get the momentum equation

$$\frac{\partial(\rho u_j)}{\partial t} + \frac{\partial(\rho u_i u_j)}{\partial x_i} = -\frac{\partial P_{ij}}{\partial x_i}. \tag{2.8}$$

where P_{ij} is the pressure tensor and the stress tensor is $\sigma_{ij} = p\delta_{ij} - P_{ij}$ with the pressure $p = \frac{1}{d} tr(P_{ij}) = \theta\rho$. Similarly, the second moment of (2.4) can be reduced to the conservation equation for the total energy $\rho E = \frac{3}{2}\rho c^2 + \frac{1}{2}\rho|\boldsymbol{u}|^2$ (Cushman-Roisin et al., 2018). The above equations are to be closed by defining constitutive relations such as for σ_{ij} or by introducing an explicit distribution function f. In fact, assuming $f \approx f^{eq}$ results in the Euler momentum equation lacking the viscous stress tensor. This indicates that the phenomenon of viscous dissipation is connected to non-equilibrium, i.e. $(f - f^{eq})$.

16

2.3. The Boltzmann Equation and the Hermite Polynomials

An alternative approach in approximating the Boltzmann equation is proposed by Grad (1949b) by expanding the distribution function f in terms of orthogonal Hermite polynomials in velocity space. This expansion is convenient in that the expansion coefficients are exactly the velocity moments of the distribution function (1.2). This results in 13-moment system including stress σ_{ij} and energy flux q_i in addition to $\rho, \boldsymbol{u}, \theta$ (Grad, 1949b).

For convenience, the BGK-Boltzmann equation (2.4) is normalized by using the characteristic velocity $c_s = \sqrt{RT_0}$ that also provides characteristic length l_0 and time t_0 scales by $l_0 = c_s t_0$ where T_0 is the characteristic temperature. The equilibrium distribution f^{eq} then takes the simpler dimensionless form:

$$f^{eq} = \rho \left(\frac{1}{2\pi\theta}\right)^{d/2} exp\left(-\frac{c^2}{2\theta}\right) \tag{2.9}$$

in d-Dimensions and the ideal-gas equation of state becomes $\boldsymbol{p} = \boldsymbol{\rho\theta}$. The procedure starts with the expansion of the distribution function $\boldsymbol{f}$ in terms of the Hermite orthonormal polynomials $\boldsymbol{H}^{(n)}$ in velocity space $\boldsymbol{v}$:

$$f(\boldsymbol{x}, \boldsymbol{v}, t) = \omega(\boldsymbol{v}) \sum_{n=0}^{\infty} \frac{1}{n!} a^{(n)}(\boldsymbol{x}, t) \cdot \boldsymbol{H}^{(n)}(\boldsymbol{v}) \tag{2.10}$$

where the expansion coefficients $\boldsymbol{a}^{(n)}(\boldsymbol{x}, t)$ are given by

$$\boldsymbol{a}^{(n)}(\boldsymbol{x}, t) = \int_{-\infty}^{\infty} f(\boldsymbol{x}, \boldsymbol{v}, t)\, \boldsymbol{H}^{(n)}(\boldsymbol{v})\, d\boldsymbol{v} \tag{2.11}$$

with the weight function

$$\omega(\boldsymbol{v}) = \left(\frac{1}{2\pi}\right)^{d/2} exp\left(-\frac{|\boldsymbol{v}|^2}{2}\right). \tag{2.12}$$

The exponential form of the weight function associated with the Hermite polynomials makes them convenient to express f^{eq} which is itself in exponential form (2.3). Here,

the index (n) also stands for the rank of the tensors $\boldsymbol{a}^{(n)}$ and $\boldsymbol{H}^{(n)}$. Some mathematical properties of the Hermite polynomials are presented in the Appendix.

The first three expansion coefficients are directly associated with the fundamental macroscopic variables:

$$a^{(0)} = \int_{-\infty}^{\infty} f(\boldsymbol{x}, \boldsymbol{v}, t) \, H^{(0)}(\boldsymbol{v}) \, d\boldsymbol{v} = \rho, \tag{2.13a}$$

$$a_i^{(1)} = \int_{-\infty}^{\infty} f(\boldsymbol{x}, \boldsymbol{v}, t) \, H_i^{(1)}(\boldsymbol{v}) \, d\boldsymbol{v} = \rho u_i, \tag{2.13b}$$

$$a_{ij}^{(2)} = \int_{-\infty}^{\infty} f(\boldsymbol{x}, \boldsymbol{v}, t) \, H_{ij}^{(2)}(\boldsymbol{v}) \, d\boldsymbol{v} = P_{ij} + \rho\left(u_i u_j - \delta_{ij}\right). \tag{2.13c}$$

Hermite series expansion of the equilibrium distribution function f^{eq} in velocity space can be constructed similarly:

$$f^{eq}(\rho, u, \theta, \boldsymbol{v}) = \omega(\boldsymbol{v}) \sum_{n=0}^{\infty} \tfrac{1}{n!} a^{(n),eq}(\rho, u, \theta) \cdot H^{(n)}(\boldsymbol{v}) \tag{2.14}$$

where

$$\boldsymbol{a}^{(n),eq}(\rho, u, \theta) = \int_{-\infty}^{\infty} f^{eq}(\rho, u, \theta, \boldsymbol{v}) \, \boldsymbol{H}^{(n)}(\boldsymbol{v}) \, d\boldsymbol{v}. \tag{2.15}$$

Since the equilibrium distribution function f^{eq} in (2.9) has the same form as the weight function (2.12), it can be written as

$$f^{eq} = \frac{\rho}{\theta^{d/2}} \, \omega\left(\frac{\boldsymbol{v} - \boldsymbol{u}}{\sqrt{\theta}}\right).$$

The integrals in (2.15) can then be written as

$$\boldsymbol{a}^{(n),eq} = \frac{\rho}{\theta^{d/2}} \int_{-\infty}^{\infty} \omega\left(\frac{\boldsymbol{v} - \boldsymbol{u}}{\sqrt{\theta}}\right) \boldsymbol{H}^{(n)}(\boldsymbol{v}) \, d\boldsymbol{v} = \frac{\rho}{\theta^{d/2}} \int_{-\infty}^{\infty} \omega(\gamma) \, \boldsymbol{H}^{(n)}\left(\sqrt{\theta}\boldsymbol{\gamma} + \boldsymbol{u}\right) d\boldsymbol{\gamma}$$

where $\boldsymbol{\gamma} = (\boldsymbol{v} - \boldsymbol{u})/\sqrt{\theta}$ is substituted in the integral and computed by using the properties of the Hermite polynomials to get the first three expansion coefficients:

$$a^{(0),eq} = \rho, \tag{2.16a}$$

$$a_i^{(1),eq} = \rho u_i, \tag{2.16b}$$

$$a_{ij}^{(2),eq} = \rho\big(u_i u_j + (\theta - 1)\delta_{ij}\big). \tag{2.16c}$$

Note that $a_{ij}^{(2),eq} - a_{ij}^{(2)} = \sigma_{ij}$. The explicit form of the Hermite expansion (2.14) can now be written up to the 2nd order moments

$$f^{eq} \approx f^{(0)} = \omega(\boldsymbol{v})\rho\Big\{1 + \boldsymbol{v}\cdot\boldsymbol{u} + \tfrac{1}{2}[(\boldsymbol{v}\cdot\boldsymbol{u})^2 - |\boldsymbol{u}|^2 + (\theta - 1)(|\boldsymbol{v}|^2 - d)]\Big\} \tag{2.17}$$

For an isothermal system ($\theta = 1$), some terms vanish (Shan et al., 2006).

Due to the orthogonality of Hermite polynomials, the individual velocity moments of the distribution function is not effected by the truncated expansion

$$f(\boldsymbol{x},\boldsymbol{v},t) \approx f^N(\boldsymbol{x},\boldsymbol{v},t) = \omega(\boldsymbol{v})\sum_{n=0}^{N}\tfrac{1}{n!}a^{(n)}(\boldsymbol{x},t)\cdot\boldsymbol{H}^{(n)}(\boldsymbol{v}) \tag{2.18}$$

Now that f^N/ω is a finite linear combination of Hermite polynomials, it is itself a polynomial of degree $\leq N$ in $\boldsymbol{v}$, thus

$$f^N(\boldsymbol{x},\boldsymbol{v},t)\boldsymbol{H}^{(n)}(\boldsymbol{v}) = \omega(\boldsymbol{v})p(\boldsymbol{x},\boldsymbol{v},t) \tag{2.19}$$

where $p(\boldsymbol{x},\boldsymbol{v},t)$ is a polynomial of degree $\leq 2N$ in $\boldsymbol{v}$. The Gauss-Hermite quadrature permits the exact evaluation of the integral

$$\boldsymbol{a}^{(n)} = \int_{-\infty}^{\infty}\omega(\boldsymbol{v})\,p(\boldsymbol{x},\boldsymbol{v},t)\,d\boldsymbol{v} = \sum_{\alpha=1}^{q}w_\alpha\,p(\boldsymbol{x},\boldsymbol{v_\alpha},t). \tag{2.20}$$

for the integrand p is a polynomial of degree $\leq 2N + 1$ and that $q = (N + 1)/2$. Here, $\boldsymbol{v_\alpha}$ and w_α are the Gauss-Hermite quadrature nodes and weights, respectively, and $\boldsymbol{v_\alpha}$ are the roots of the Hermite polynomial of order q. Some properties of Gauss-Hermite quadrature are presented in the Appendix. This provides an alternative method of evaluation of the expansion coefficients (2.11) in discrete form

$$a^{(n)}(x,t) = \sum_{\alpha=1}^{q} \frac{w_\alpha}{\omega(v_\alpha)} f^N(x, v_\alpha, t) H^{(n)}(v_\alpha). \qquad (2.21)$$

The expansion coefficients up to the 2nd order in (2.13) and (2.16) are sufficient to obtain an associated with the fundamental macroscopic variables, namely, ρ, u, σ.

The high accuracy evaluation of the integrals in discrete form based on the Gauss-Hermite quadrature in (2.20) leads the way for the discretization of the velocity moments in (1.2) and eventually the Boltzmann equation. Gauss-Hermite quadrature evaluation of the velocity moments in (1.2) gives

$$\rho = \sum_{\alpha=1}^{q} \frac{w_\alpha}{\omega(v_\alpha)} f^N(x, v_\alpha, t), \qquad (2.22a)$$

$$\rho u = \sum_{\alpha=1}^{q} \frac{w_\alpha}{\omega(v_\alpha)} v_\alpha f^N(x, v_\alpha, t), \qquad (2.22b)$$

$$P + \rho uu = \sum_{\alpha=1}^{q} \frac{w_\alpha}{\omega(v_\alpha)} v_\alpha v_\alpha f^N(x, v_\alpha, t), \qquad (2.22c)$$

where the last moment is defined in (2.13c). By absorbing the quadrature weights in f^N by $f_\alpha(x,t) = w_\alpha f^N(x, v_\alpha, t)/\omega(v_\alpha)$, these moments can be written as follows:

$$\rho = \sum_{\alpha=1}^{q} f_\alpha, \qquad (2.23a)$$

$$\rho u = \sum_{\alpha=1}^{q} v_\alpha f_\alpha, \qquad (2.23b)$$

$$P + \rho uu = \sum_{\alpha=1}^{q} v_\alpha v_\alpha f_\alpha. \qquad (2.23c)$$

The BGK-Boltzmann equation (2.4) is now discretized by directly evaluating at $\boldsymbol{v}_\alpha$ and multiplying by the constant $w_\alpha/\omega(\boldsymbol{v}_\alpha)$ to get:

$$\frac{\partial f_\alpha}{\partial t} + \boldsymbol{v}_\alpha \cdot \boldsymbol{\nabla} f_\alpha = -\frac{1}{\tau}\left(f_\alpha - f_\alpha^{(0)}\right) \qquad (2.24a)$$

where $f_\alpha^{(0)}$ is obtained from (2.17) as follows:

$$f_\alpha^{(0)} = w_\alpha \rho \left\{ 1 + \boldsymbol{v}_\alpha \cdot \boldsymbol{u} + \tfrac{1}{2}[(\boldsymbol{v}_\alpha \cdot \boldsymbol{u})^2 - |\boldsymbol{u}|^2 + (\theta - 1)(|\boldsymbol{v}_\alpha|^2 - d)] \right\} \quad (2.24b)$$

This is the Lattice Boltzmann equation. The discretization in space over lattice and time leads to the Lattice Boltzmann method whose implementation is presented in Chapter 4.

The discretization leading to the Lattice Boltzmann equation (2.24) is, in fact, the collocation discretization where the residue resulting from substituting the truncated representation f^N of f into BGK-Boltzmann equation (2.4) is forced to vanish at the collocation (Gauss-Hermite quadrature nodes) points $\boldsymbol{v}_\alpha$. An alternative approach of discretization is based on Galerkin projection of the residue onto the space spanned by the Hermite polynomials. This results in a system of partial differential equations for the evolution of the expansion coefficients $\boldsymbol{a}^{(n)}(\boldsymbol{x}, t)$ instead. The formulation and the numerical implementation are presented in Chapter 3.

CHAPTER 3

DISCRETIZATION BY GALERKIN PROCEDURE

This discretization method involves using trial and test functions in terms of Hermite polynomials in velocity space as presented in Chapter 2 for the discretization of the Boltzmann equation using the Galerkin projection procedure. In this chapter, the formulation is presented for a 2D problem ($d = 2$).

3.1. Galerkin Procedure

The residual resulting from the substitution of the truncated representation f^N of the distribution function f in (2.18) into the BGK-Boltzmann equation (2.4)

$$R\left(\boldsymbol{a}^{(n)}, \boldsymbol{v} \right) \equiv \frac{\partial f^N}{\partial t} + \boldsymbol{v} \cdot \frac{\partial f^N}{\partial x} + \frac{1}{\tau}\left(f^N - f^{(0)} \right) \tag{3.1}$$

is projected onto the space of Hermite polynomials and set to zero

$$\int_{-\infty}^{\infty} R\left(\boldsymbol{a}^{(n)}, \boldsymbol{v} \right) \boldsymbol{H}^{(n)}(\boldsymbol{v}) d\boldsymbol{v} = 0 \tag{3.2}$$

for $n \leq N$ to get the Galerkin equations for the expansion coefficients $\boldsymbol{a}^{(n)}(\boldsymbol{x}, t)$. In accordance with the discussion in Chapter 2, it suffices to choose $N = 2$ and thus $f^{(0)}$ of (2.17) is taken for $d = 2$ as

$$f^{(0)} = \omega(\boldsymbol{v})\rho \left\{ 1 + \boldsymbol{v} \cdot \boldsymbol{u} + \tfrac{1}{2}[(\boldsymbol{v} \cdot \boldsymbol{u})^2 - |\boldsymbol{u}|^2 + (\theta - 1)(|\boldsymbol{v}|^2 - 2)] \right\} \tag{2.17}$$

For notational convenience, the macroscopic associations of the expansion coefficients in (2.13) are rewritten in 2D as

$$a_1 \equiv a^{(0)} = \int_{-\infty}^{\infty} f(\boldsymbol{x}, \boldsymbol{v}, t) \, H^{(0)}(\boldsymbol{v}) \, d\boldsymbol{v} = \rho, \tag{3.3a}$$

$$a_2 \equiv a_1^{(1)} = \int_{-\infty}^{\infty} f(\boldsymbol{x}, \boldsymbol{v}, t) \, H_1^{(1)}(\boldsymbol{v}) \, d\boldsymbol{v} = \rho u_1, \qquad (3.3b)$$

$$a_3 \equiv a_2^{(1)} = \int_{-\infty}^{\infty} f(\boldsymbol{x}, \boldsymbol{v}, t) \, H_2^{(1)}(\boldsymbol{v}) \, d\boldsymbol{v} = \rho u_2, \qquad (3.3c)$$

$$a_4 \equiv a_{12}^{(2)} = \int_{-\infty}^{\infty} f(\boldsymbol{x}, \boldsymbol{v}, t) \, H_{12}^{(2)}(\boldsymbol{v}) \, d\boldsymbol{v} = \rho u_1 u_2 - \sigma_{12}, \qquad (3.3d)$$

$$a_5 \equiv a_{11}^{(2)} = \int_{-\infty}^{\infty} f(\boldsymbol{x}, \boldsymbol{v}, t) \, H_{11}^{(2)}(\boldsymbol{v}) \, d\boldsymbol{v} = \rho u_1^2 - \sigma_{11}, \qquad (3.3e)$$

$$a_6 \equiv a_{22}^{(2)} = \int_{-\infty}^{\infty} f(\boldsymbol{x}, \boldsymbol{v}, t) \, H_{22}^{(2)}(\boldsymbol{v}) \, d\boldsymbol{v} = \rho u_2^2 - \sigma_{22}. \qquad (3.3f)$$

By using the properties of the Hermite polynomials in the Appendix, Galerkin equations for the expansion coefficients $\boldsymbol{a}^{(n)}(\boldsymbol{x}, t)$ are obtained as:

$$\frac{\partial a_1}{\partial t} + \left(\frac{\partial a_2}{\partial x_1} + \frac{\partial a_3}{\partial x_2} \right) = 0, \qquad (3.4a)$$

$$\frac{\partial a_2}{\partial t} + \left(\frac{\partial a_1}{\partial x_1} + \frac{\partial a_5}{\partial x_1} + \frac{\partial a_4}{\partial x_2} \right) = 0, \qquad (3.4b)$$

$$\frac{\partial a_3}{\partial t} + \left(\frac{\partial a_4}{\partial x_1} + \frac{\partial a_1}{\partial x_2} + \frac{\partial a_6}{\partial x_2} \right) = 0, \qquad (3.4c)$$

$$\frac{\partial a_4}{\partial t} + \left(\frac{\partial a_3}{\partial x_1} + \frac{\partial a_2}{\partial x_2} \right) = -\frac{1}{\tau} \left(a_4 - \frac{a_2 a_3}{a_1} \right), \qquad (3.4d)$$

$$\frac{\partial a_5}{\partial t} + 2 \frac{\partial a_2}{\partial x_1} = -\frac{1}{\tau} \left(a_5 - \frac{a_2^2}{a_1} \right), \qquad (3.4e)$$

$$\frac{\partial a_6}{\partial t} + 2 \frac{\partial a_3}{\partial x_2} = -\frac{1}{\tau} \left(a_6 - \frac{a_3^2}{a_1} \right). \qquad (3.4f)$$

3.2. Connection to Macroscopic Equations

Chapman-Enskog expansion is a classical procedure that is used to show the connection between the Boltzmann equation and the macroscopic equations. It is based on an asymptotic expansion in powers of Knudsen number (Kn) which also measures the level of departure from equilibrium in the distribution function f. The

procedure leads to the Navier-Stokes equations from the Boltzmann equations for small Kn. In the case of the Galerkin equations (3.4), Tölke, et. al. (2000) used the following argument in order to recover the macroscopic equations:

The equations (3.4d-f) are rewritten in the form

$$\frac{\partial}{\partial t}\underbrace{\begin{bmatrix} a_4 \\ a_5 \\ a_6 \end{bmatrix}}_{g(t)} + \frac{1}{\tau}\begin{bmatrix} a_4 \\ a_5 \\ a_6 \end{bmatrix} + \underbrace{\begin{bmatrix} \partial a_3/\partial x_1 + \partial a_2/\partial x_2 - \frac{1}{\tau}(a_2 a_3/a_1) \\ 2\,\partial a_2/\partial x_1 - \frac{1}{\tau}(a_2^2/a_1) \\ 2\,\partial a_3/\partial x_2 - \frac{1}{\tau}(a_3^2/a_1) \end{bmatrix}}_{C} = 0 \qquad (3.5)$$

and considered on the time interval $[0, T_0]$ where T_0 is an intermediate time scale small enough $\tau \ll T_0 \ll T_1$ so that the macroscopic values like density and momentum can be taken as time independent, say C. Here, T_1 is the macroscopic time scale and the relaxation time τ is of the order of the collision time. The equation (3.5) can then be idealized as

$$\frac{\partial g(t)}{\partial t} + \frac{1}{\tau}g(t) + C = 0, \qquad t \in [0, T_0] \qquad (3.6)$$

whose solution is

$$g(t) = -\tau C + c_1 exp\left(-\frac{1}{\tau}t\right). \qquad (3.7)$$

Thus, $g(t)$ decays exponentially fast to steady state as τ (or the mean free path or the Mach number) becomes very small. Thus, (3.5) can be solved for the expansion coefficients a_4, a_5, a_6 to get

$$a_4 = \left(\frac{a_2 a_3}{a_1}\right) - \tau\left(\frac{\partial a_3}{\partial x_1} + \frac{\partial a_2}{\partial x_2}\right), \qquad (3.8a)$$

$$a_5 = \left(\frac{a_2^2}{a_1}\right) - 2\tau\frac{\partial a_2}{\partial x_1}, \qquad (3.8b)$$

$$a_6 = \left(\frac{a_3^2}{a_1}\right) - 2\tau\frac{\partial a_3}{\partial x_2}. \qquad (3.8c)$$

Substituting (3.8) into (3.4a-c) and expressing the coefficients a_i in terms of macroscopic variables (3.3) yields the macroscopic equations:

$$\frac{\partial \rho}{\partial t} + \frac{\partial \rho u_1}{\partial x_1} + \frac{\partial \rho u_2}{\partial x_2} = 0, \tag{3.9a}$$

$$\frac{\partial \rho u_1}{\partial t} + \frac{\partial \rho u_1^2}{\partial x_1} + \frac{\partial \rho u_1 u_2}{\partial x_2} + \frac{\partial \rho}{\partial x_1} = \frac{\partial \sigma_{11}}{\partial x_1} + \frac{\partial \sigma_{12}}{\partial x_2}, \tag{3.9b}$$

$$\frac{\partial \rho u_2}{\partial t} + \frac{\partial \rho u_2^2}{\partial x_2} + \frac{\partial \rho u_1 u_2}{\partial x_1} + \frac{\partial \rho}{\partial x_2} = \frac{\partial \sigma_{21}}{\partial x_1} + \frac{\partial \sigma_{22}}{\partial x_2}, \tag{3.9c}$$

$$\sigma_{ij} = \tau \left(\frac{\partial \rho u_i}{\partial x_j} + \frac{\partial \rho u_j}{\partial x_i} \right). \tag{3.9d}$$

Here the relationship (3.9d) between the stresses and the flow field gives the expression for the kinematic viscosity as $v = \tau$. The equation of state is $p = \rho$ for the isothermal system $\theta = 1$.

3.3. Discretization in the Time-Space Domain

The system of equations (3.4) can be written in the form:

$$\frac{\partial U}{\partial t} + A \frac{\partial U}{\partial x_1} + B \frac{\partial U}{\partial x_2} = N(U) \tag{3.10}$$

where U is the Hermite coefficient vector

$$U(x_1, x_2, t) = [a_1 \quad a_2 \quad a_3 \quad a_4 \quad a_5 \quad a_6]^T,$$

A and B are the spatial differential operation matrices, and N are the nonlinear (collision) terms. The system (3.10) is discretized by using a second order upwind scheme on a uniform mesh in space and a first order explicit Euler scheme in time. The matrices A and B are split into A^+, A^-, B^+ and B^- matrices corresponding to their eigenvalues $1, -1, \sqrt{3}, -\sqrt{3}, 0, 0$ such that

$$A^+ = P\Lambda^+ P^{-1} \qquad \text{and} \qquad A^- = P\Lambda^- P^{-1}$$

where P is the matrix of the eigenvectors of A and $\Lambda^{+/-}$ are diagonal matrices. After similar splitting for B, they become:

$$
A^{+} = \begin{bmatrix}
\sqrt{3}/6 & 1/2 & 0 & 0 & \sqrt{3}/6 & 0 \\
1/2 & \sqrt{3}/2 & 0 & 0 & 1/2 & 0 \\
0 & 0 & 1/2 & 1/2 & 0 & 0 \\
0 & 0 & 1/2 & 1/2 & 0 & 0 \\
\sqrt{3}/3 & 1 & 0 & 0 & \sqrt{3}/3 & 0 \\
0 & 0 & 0 & 0 & 0 & 0
\end{bmatrix},
$$

$$
A^{-} = \begin{bmatrix}
-\sqrt{3}/6 & 1/2 & 0 & 0 & -\sqrt{3}/6 & 0 \\
1/2 & -\sqrt{3}/2 & 0 & 0 & 1/2 & 0 \\
0 & 0 & -1/2 & 1/2 & 0 & 0 \\
0 & 0 & 1/2 & -1/2 & 0 & 0 \\
-\sqrt{3}/3 & 1 & 0 & 0 & -\sqrt{3}/3 & 0 \\
0 & 0 & 0 & 0 & 0 & 0
\end{bmatrix},
$$

$$
B^{+} = \begin{bmatrix}
\sqrt{3}/6 & 0 & 1/2 & 0 & 0 & \sqrt{3}/6 \\
0 & 1/2 & 0 & 1/2 & 0 & 0 \\
1/2 & 0 & \sqrt{3}/2 & 0 & 0 & 1/2 \\
0 & 1/2 & 0 & 1/2 & 0 & 0 \\
0 & 0 & 0 & 0 & 0 & 0 \\
\sqrt{3}/3 & 0 & 1 & 0 & 0 & \sqrt{3}/3
\end{bmatrix},
$$

$$
B^{-} = \begin{bmatrix}
-\sqrt{3}/6 & 0 & 1/2 & 0 & 0 & -\sqrt{3}/6 \\
0 & -1/2 & 0 & 1/2 & 0 & 0 \\
1/2 & 0 & -\sqrt{3}/2 & 0 & 0 & 1/2 \\
0 & 1/2 & 0 & -1/2 & 0 & 0 \\
0 & 0 & 0 & 0 & 0 & 0 \\
-\sqrt{3}/3 & 0 & 1 & 0 & 0 & -\sqrt{3}/3
\end{bmatrix}.
$$

Numerical scheme reads as follows (Hirsch, 2007):

$$[U]_{i,j}^{n+1} = [U]_{i,j}^n - \frac{\Delta t}{2\Delta x} \big(A^+ \big(3[U]_{i,j}^n - 4[U]_{i-1,j}^n + [U]_{i-2,j}^n \big) +$$

$$A^- \big(-[U]_{i+2,j}^n + 4[U]_{i+1,j}^n - 3[U]_{i,j}^n \big) +$$

$$B^+ \big(3[U]_{i,j}^n - 4[U]_{i,j-1}^n + [U]_{i,j-2}^n \big) +$$

$$B^- \big(-[U]_{i,j+2}^n + 4[U]_{i,j+1}^n - 3[U]_{i,j}^n \big) \big) + \Delta t \, N \big([U]_{i,j}^n \big) \quad (3.11)$$

where $[U]_{i,j}^n = U(i\Delta x, j\Delta x, n\Delta t)$ with Δt denoting the time step size and Δx the spatial step size. For stability, $\Delta t < 2\tau$ and $\tau \ll \Delta x$ (Mei et al., 1998).

3.4. Steady State Plane Poiseuille Flow

The formulation above is implemented in the numerical simulation of steady state plane Poiseuille flow. The advantage of such a flow is its geometric simplicity and availability of an exact solution. The subtlety is in the implementation of the pressure gradient that drives the flow. Conventionally, the pressure gradient is implemented as a volume force in the momentum equation. In order to conform the formulation above, however, the pressure gradient is implemented as an initialization of the pressure variable in the form of a linear profile. It should be noted that in the Boltzmann equation setting, density and pressure are tied together by an ideal gas equation of state $p = \rho\theta$ ($p = \rho$ for isothermal system $\theta = T/T_0 = 1$).

For the numerical experiment, the fluid with viscosity $\nu = 0.01 \ m^2/s$ is driven by a pressure gradient of 0.0008 Pa/m in a channel segment of horizontal and vertical dimensions of 1 m. These values dictate a steady state centreline velocity of $u_1|_{x=0.5} = 0.01$. The numerical convergence to the steady Poiseuille parabolic profile through the transients is shown in Figure 3.1 for a 64×64 grid. Further shown in Figure 3.2 are the steady state profiles of the macroscopic physical variables that appear in (3.2). They are in agreement with the expected Poiseuille flow profiles for the associated physical flow variables.
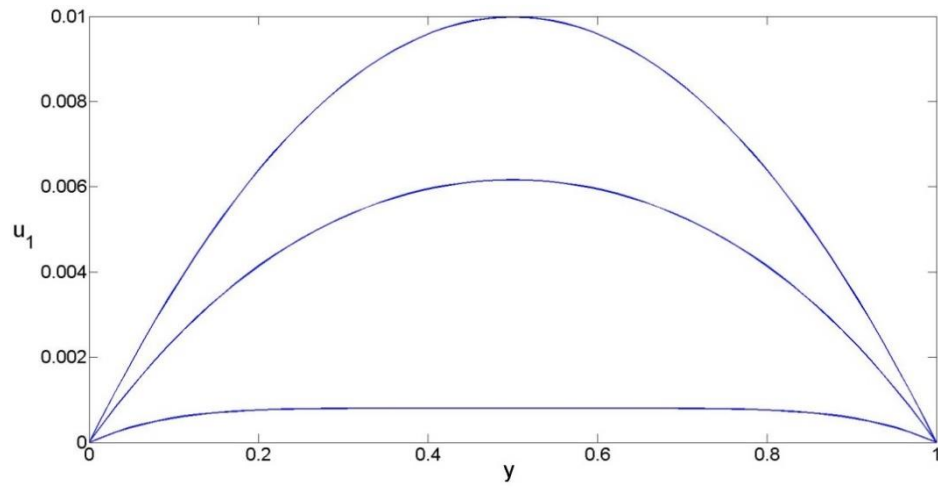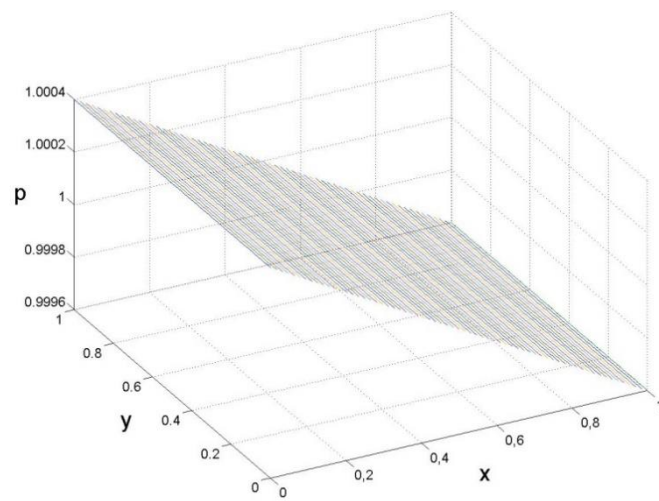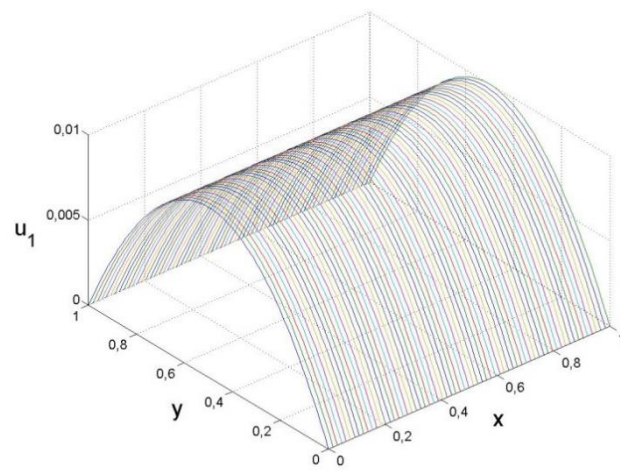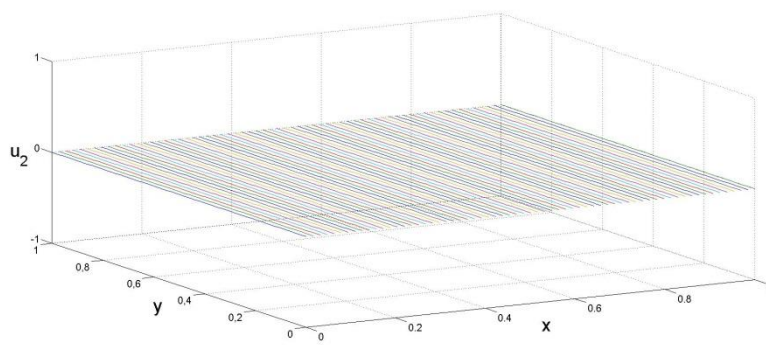
28

Figure 3.1. *Numerical convergence of the Poiseuille velocity profile for a* 64×64 *grid.*
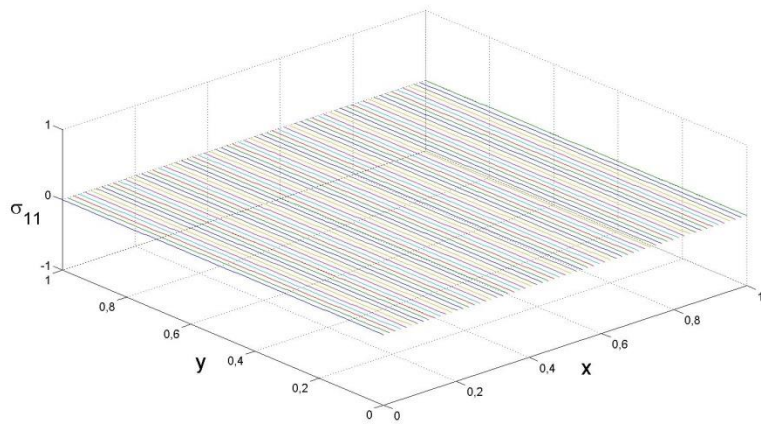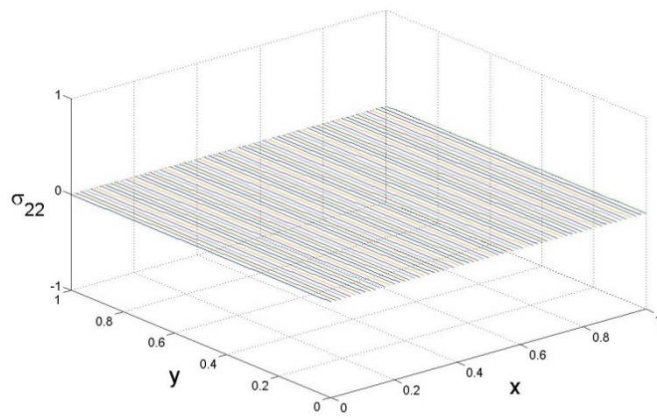

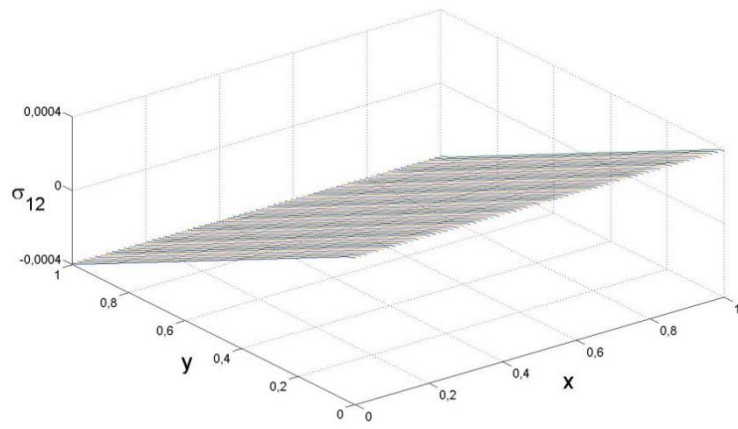(a)

(b)

(c)

(d)

(e)

31

(f)

Figure 3.2. Profiles of flow variables as in (3.3) associated with the Poiseuille flow.

CHAPTER 4

LATTICE BOLTZMANN METHOD

Introducing the Gauss-Hermite quadrature in computing the velocity moment integrals in Chapter 2 resulted in the expressions for the macroscopic variables in (2.23) and led to the Lattice Boltzmann equation (2.24). While this equation is discrete in velocity, it is still continuous in time and space. It embodies two processes: streaming and collision. It is clear from (2.24) that the streaming process is linear while the nonlinearity enters through the collision process. A numerical solution thus requires further discretization in time with step size Δt and in space with step size Δx. In the presence of a set of discrete velocities $\boldsymbol{v_\alpha}$, the numerical solution of the Lattice Boltzmann equation involves streaming from $(\boldsymbol{x}, t)$ to $(\boldsymbol{x} + \boldsymbol{v_\alpha}\Delta t, t + \Delta t)$ under the effect of the BGK collision operator $C(f_\alpha) = -(f_\alpha - f_\alpha^{(0)})/\tau$. The neighbourhoods $\boldsymbol{x} + \boldsymbol{v_\alpha}\Delta t$ around $\boldsymbol{x}$ created by the discrete velocity set $\{\boldsymbol{v_\alpha}\}$ form a lattice and the resulting numerical procedure is called the Lattice Boltzmann Method (LBM).

4.1. The Lattice

In LBM, the spatial evolution of the distribution function as governed by the velocity discretized Boltzmann equation takes place locally in a fixed lattice. In the streaming process, along the defined directions, each node connects to its adjacent node in each lattice as in Figure 4.1. Connecting the lattice nodes are the links set as a result of the particular directions and magnitudes of the set of discrete velocities. In addition, on each lattice node resides the distribution function (Boix, 2013)

In literature, different kinds of lattice configurations are in use and labelled by their arrangements in the form DdQq. In this naming convention, d represents the physical

dimension while q represents the number of velocity directions. For example, in D2Q9 lattice arrangement, lattice span is in two dimensions and it has 9 possible velocity directions. One of these velocity directions is for non-moving particle which has zero velocity.
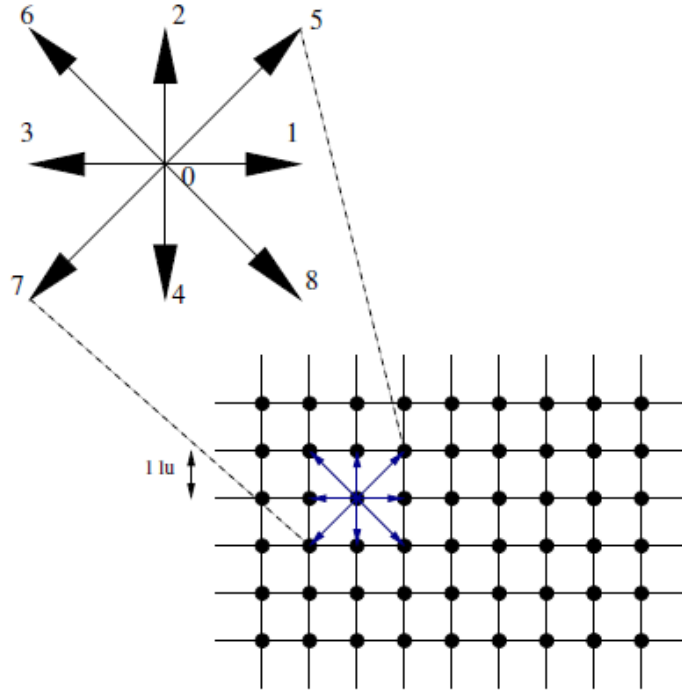
Figure 4.1. *Lattice example on 2D geometry (Boix, 2013).*

Most commonly used lattice arrangements to simulate hydrodynamics are D1Q3, D2Q9, D3Q15, D3Q19 and D3Q27 (see Figures 4.2-4.4). The three lattice configurations in 3D are ordered in decreasing computational efficiency such as memory and computing power requirements. However, D3Q15, D3Q19 have been shown to lack some degree of isotropy in comparison to D3Q27. Thus, D3Q27 is a good choice for flows with high dynamical degrees of freedom such as for turbulent flow modelling. In fact, symmetry and isotropy of the lattice arrangement are the two important requirements in choosing a suitable lattice for the underlying physics. In order to simulate advection-diffusion problems, for example, lower level of isotropy

may be sufficient such as D2Q4 that is suitable for simulation of heat conduction (Wolf-Gladrow, 2000). Other lattice arrangements are square lattice (D2Q4), triangular lattice (D2Q7) (McNamara et al., 1988), D2Q13-WB (Weimar et al., 1993), D2Q21 (Fahner, 1991), D3Q15 and Thermal LBMs D2Q13-FHP (multi-speed FHP model).
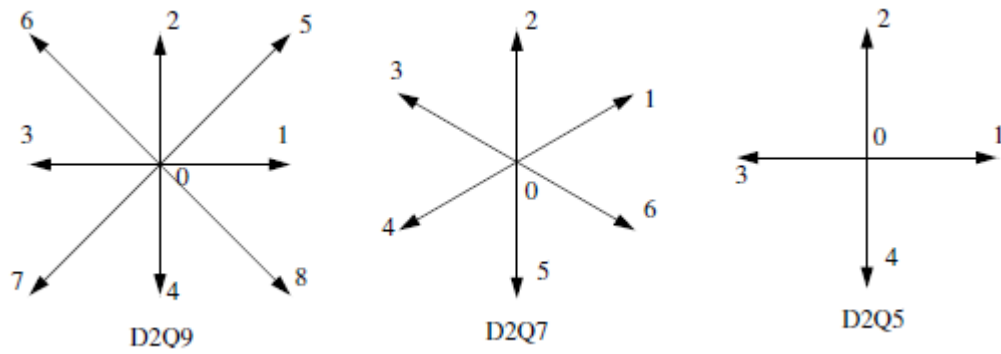
Figure 4.2. *D2Q9, D2Q7 and D2Q5 arrangements*
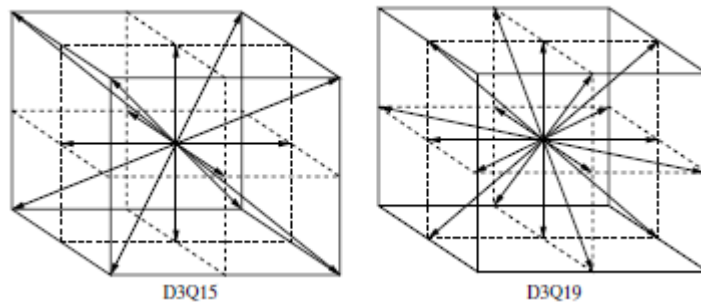
Figure 4.3. *3D lattice models*
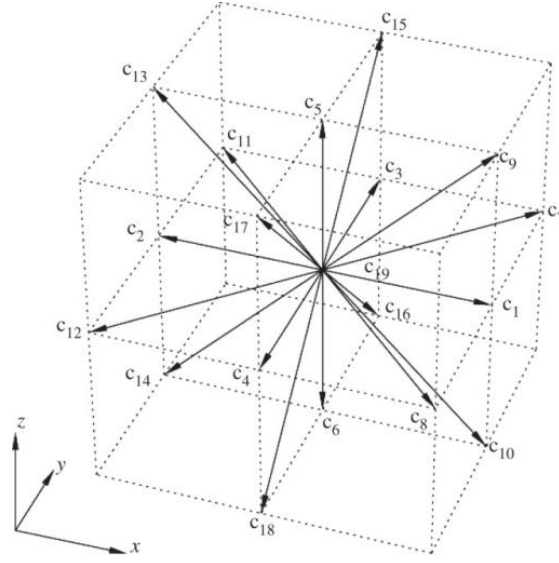
Figure 4.4. Illustration of D3Q19 model with nine lattice node (Pontrelli et al., 2007)

In Chapter 2, the velocity discretization is obtained using Gauss-Hermite quadrature rule giving a suitable set of discrete velocities $\boldsymbol{v}_\alpha$ and the corresponding weights w_α. The resulting set are:

Table 4.1. *Lattice configurations as constructed as tensor products of Gauss-Hermite quadrature rule.*

Notation	Velocities, $\boldsymbol{v}_\alpha$	No.	$|\boldsymbol{v}_\alpha|$	w_α
D1Q3	(0)	1	0	2/3
	(± 1)	2	1	1/6
D2Q9	$(0,0)$	1	0	4/9
	$(\pm 1,0), (0,\pm 1)$	4	1	1/9
	$(\pm 1,\pm 1)$	4	$\sqrt{2}$	1/36
D3Q27	$(0,0,0)$	1	0	8/27
	$(\pm 1,0,0), (0,\pm 1,0)\ (0,0,\pm 1)$	6	1	2/27
	$(\pm 1,\pm 1,0), (\pm 1,0,\pm 1), (0,\pm 1,\pm 1)$	12	$\sqrt{2}$	1/54
	$(\pm 1,\pm 1,\pm 1)$	8	$\sqrt{3}$	1/216

Yet another consideration in deriving the lattice configurations is physical namely, the isotropy of the lattice (Satoh, 2011). Sufficiency of isotropy in the lattice configuration depends on the underlying physics of the model. The isotropy considerations lead to the following conditions:

$$\sum_\alpha w_\alpha = 1,$$

$$\sum_\alpha w_\alpha \boldsymbol{v}_{\alpha,i} = 0,$$

$$\sum_\alpha w_\alpha \boldsymbol{v}_{\alpha,i} \boldsymbol{v}_{\alpha,j} = \delta_{ij},$$

$$\sum_\alpha w_\alpha \boldsymbol{v}_{\alpha,i} \boldsymbol{v}_{\alpha,j} \boldsymbol{v}_{\alpha,k} = 0,$$

$$\sum_\alpha w_\alpha \boldsymbol{v}_{\alpha,i} \boldsymbol{v}_{\alpha,j} \boldsymbol{v}_{\alpha,k} \boldsymbol{v}_{\alpha,m} = (\delta_{ij}\delta_{km} + \delta_{ik}\delta_{jm} + \delta_{im}\delta_{jk}),$$

$$\sum_\alpha w_\alpha \boldsymbol{v}_{\alpha,i} \boldsymbol{v}_{\alpha,j} \boldsymbol{v}_{\alpha,k} \boldsymbol{v}_{\alpha,m} \boldsymbol{v}_{\alpha,n} = 0. \tag{4.1}$$

together with the weights w_α to be non-negative. Thus, it is required that all velocity moments up to the fifth order are to be satisfied for LBM to be suitable for modelling hydrodynamics (see Table A.1 in the Appendix). In order to simulate advection-diffusion problems, for example, lower level of isotropy may be sufficient.

4.2. Lattice Equilibrium Distribution Function

The equilibrium distribution function (2.9) for an isothermal system ($\theta = 1$) can also be written in the form:

$$\boldsymbol{f}^{eq} = \frac{\rho}{(2\pi)^{d/2}} exp\left(-\frac{|\boldsymbol{v} - \boldsymbol{u}|^2}{2}\right)$$

$$= \frac{\rho}{(2\pi)^{d/2}} exp\left(-\frac{|\boldsymbol{v}|^2}{2}\right) exp\left(-\frac{|\boldsymbol{u}|^2 - 2\boldsymbol{v} \cdot \boldsymbol{u}}{2}\right).$$

It can be expanded in Taylor series about the stationary state, $u = \boldsymbol{0},$ to get

$$f^{eq} = \frac{\rho}{(2\pi)^{d/2}} exp\left(-\frac{|v|^2}{2}\right)\left[1 + v \cdot u + \frac{1}{2}((v \cdot u)^2 - |u|^2) \cdots \right].$$

The general form of the lattice equilibrium distribution function up to $O(|u|^2)$ can be written as

$$f_\alpha^{eq} = \rho[a + b \, v_\alpha \cdot u + c \, (v_\alpha \cdot u)^2 + d \, |u|^2]. \tag{4.2}$$

where a, b, c, d are lattice constants. This expansion is valid only for small velocities u, or small Mach number u/c_s. Note that this form introduces second order nonlinearity as in the Navier-Stokes equations.

The constraints (2.23) that f_α^{eq} should also satisfy can be used to determine the coefficients in (4.2). Since the values of these unknown coefficients depend on the lattice configuration, we consider D2Q9 as an example (Satoh, 2011). It can be shown that it yields the form

$$f_\alpha^{eq} = \omega_\alpha \rho \left[1 + 3 \, v_\alpha \cdot u + \frac{9}{2} \, (v_\alpha \cdot u)^2 - \frac{3}{2} \, |u|^2\right] \tag{4.3}$$

where ω_α are the Gauss-Hermite quadrature weights corresponding to D2Q9 (see Table 4.1). The apparent discrepancy when (4.3) is compared with (2.24b) can be resolved by a scaling of $1/\sqrt{3}$. This quantity often named as the sound speed c_s in LBM literature for its appearance in the relation between the pressure and the density $p = c_s^2 \rho$, but it is simply a scaling factor or pseudo-sound-speed as it is termed in Nourgaliev (2003). By introducing this scaling factor c_s in (4.3), it takes the form

$$f_\alpha^{eq} = \omega_\alpha \rho \left[1 + \frac{v_\alpha \cdot u}{c_s^2} + \frac{1}{2}\frac{(v_\alpha \cdot u)^2}{c_s^4} - \frac{1}{2}\frac{|u|^2}{c_s^2}\right]. \tag{4.4}$$

Thus, lattice equilibrium distribution function (4.3) will be used for the lattice configuration D2Q9 with the reference sound speed $c_s = 1/\sqrt{3}$, so that $p = \rho/3$ in an isothermal system.

4.3. Macroscopic Conservation Equations

Chapman-Enskog analysis provides the macroscopic connection by establishing the non-equilibrium contributions to f in the form of a perturbation expansion about f^{eq} as Knudsen number $Kn \to 0$. This expansion is motivated by attempts to solve BGK-Boltzmann equation (2.4) written in the form

$$f^{eq} = f + \tau \underbrace{\left(\frac{\partial f}{\partial t} + v_i \frac{\partial f}{\partial x_i} \right)}_{Df/Dt}$$

and used in the following construction (N. X. Chen et al., 2017):

$$f = f^{eq} - \tau \frac{Df}{Dt} = f^{eq} - \tau \frac{D}{Dt} \left(f^{eq} - \tau \frac{Df}{Dt} \right)$$

$$= f^{eq} - \tau \frac{Df^{eq}}{Dt} + \tau^2 \frac{D^2 f^{eq}}{Dt^2} - \cdots \tag{4.5}$$

The relaxation parameter τ is of the order of Kn and so as $Kn \to 0$, (4.5) is a perturbation expansion (Latt et. al., 2008).

Chapman-Enskog analysis proceeds with an expansion of f_α in (2.24a) in the form:

$$f_\alpha = f_\alpha^{eq} + \epsilon f_\alpha^{(1)} + \epsilon^2 f_\alpha^{(2)} + \cdots$$

and with a multiscale expansion

$$\frac{\partial}{\partial t} = \epsilon \frac{\partial}{\partial t_1} + \epsilon^2 \frac{\partial}{\partial t_2} + \cdots \qquad \text{and} \qquad \frac{\partial}{\partial x} = \epsilon \frac{\partial}{\partial x_1} + \cdots$$

where it is assumed that the diffusion time scale t_1 is much slower than the convection time scale t_2 (S. Chen et al., 1998); (Frisch et al., 1986). While f_α^{eq} also satisfies (2.23), $f_\alpha^{(k)}$ should satisfy the following constraints

$$\sum_{\alpha=1}^{q} f_\alpha^{(k)} = 0, \qquad \sum_{\alpha=1}^{q} \boldsymbol{v}_\alpha f_\alpha^{(k)} = \boldsymbol{0}. \tag{4.6}$$

Substituting these expansions in the Lattice Boltzmann equation (2.24a), one obtains the following equations (Zhang, 2011):

$$\epsilon^0: \qquad \frac{\partial f_\alpha^{eq}}{\partial t_1} + \boldsymbol{v}_\alpha \cdot \boldsymbol{\nabla}_1 f_\alpha^{eq} = -\frac{1}{\tau} f_\alpha^{(1)}. \qquad (4.7a)$$

$$\epsilon^1: \qquad \frac{\partial f_\alpha^{(1)}}{\partial t_2} + \left(1 - \frac{2}{\tau}\right)\left[\frac{\partial f_\alpha^{(1)}}{\partial t_1} + \boldsymbol{v}_\alpha \cdot \boldsymbol{\nabla}_1 f_\alpha^{(1)}\right] = -\frac{1}{\tau} f_\alpha^{(2)}. \qquad (4.7b)$$

where $\boldsymbol{\nabla}_1$ is the gradient operator based on the spatial variable $\boldsymbol{x}_1$. By taking velocity moments of these equations and using the relations (2.16) and (4.6), one obtains the mass and momentum equations:

$$\frac{\partial \rho}{\partial t} + \frac{\partial (\rho u_i)}{\partial x_i} = 0 \qquad (4.8a)$$

$$\frac{\partial (\rho u_j)}{\partial t} + \frac{\partial \Pi_{ij}^{(0)}}{\partial x_i} + \frac{2\tau - 1}{2}\frac{\partial \Pi_{ij}^{(1)}}{\partial x_i} = 0. \qquad (4.8b)$$

For the lattice configuration D2Q9 and thus using (4.3) and (4.7a), one gets:

$$\Pi_{ij}^{(0)} = \sum_{\alpha=1}^{q} \boldsymbol{v}_{\alpha,i}\boldsymbol{v}_{\alpha,j} f_\alpha^{eq} = p\delta_{ij} + \rho u_i u_j,$$

$$\Pi_{ij}^{(1)} = \sum_{\alpha=1}^{q} \boldsymbol{v}_{\alpha,i}\boldsymbol{v}_{\alpha,j} f_\alpha^{(1)} = \frac{\partial \rho u_i}{\partial x_j} + \frac{\partial \rho u_j}{\partial x_i}.$$

For small enough density fluctuations, the momentum equation (4.8b) becomes equivalent to the Navier-Stokes equations (S. Chen et al., 1998). The coefficient of $\partial \Pi_{ij}^{(1)}/\partial x_i$ in (4.8b) gives the kinematic viscosity as $\nu = (2\tau - 1)/2$.

4.4. Lattice Boltzmann Model

Velocity discretized Boltzmann equation with a general collision operator C_α,

$$\frac{\partial f_\alpha}{\partial t} + \boldsymbol{v}_\alpha \cdot \boldsymbol{\nabla} f_\alpha = C_\alpha(\boldsymbol{x}, t)$$

can be solved for each velocity (characteristics) direction $\boldsymbol{v}_\alpha$ at $(\boldsymbol{x}, t)$ to get

$$f_\alpha(\boldsymbol{x} + \boldsymbol{v}_\alpha \Delta t, t + \Delta t) - f_\alpha(\boldsymbol{x}, t) = \int_0^{\Delta t} C_\alpha(\boldsymbol{x} + \boldsymbol{v}_\alpha \xi, t + \xi) \, d\xi.$$

In order to arrive at a fully discretized model, the right-hand side must be approximated. The classical Lattice Boltzmann method uses a one-point polynomial interpolation of the integrand at $(\boldsymbol{x}, t)$ to get

$$f_\alpha(\boldsymbol{x} + \boldsymbol{v}_\alpha \Delta t, t + \Delta t) - f_\alpha(\boldsymbol{x}, t) = \Delta t \, C_\alpha(\boldsymbol{x}, t). \tag{4.9}$$

This is, in fact, first order explicit forward Euler discretization along the characteristics direction $\boldsymbol{v}_\alpha$. Substituting the BGK collision operator into (4.9) leads to

$$f_\alpha(\boldsymbol{x} + \boldsymbol{v}_\alpha \Delta t, t + \Delta t) = f_\alpha(\boldsymbol{x}, t) - \frac{\Delta t}{\tau} \left(f_\alpha(\boldsymbol{x}, t) - f_\alpha^{eq} \right). \tag{4.10}$$

In the numerical implementation of (4.10), two separate stages can be identified. One comes from discretization along the characteristics, $f_\alpha(\boldsymbol{x} + \boldsymbol{v}_\alpha \Delta t, t + \Delta t) - f_\alpha(\boldsymbol{x}, t)$, called the streaming (or propagation) step and the other comes from the local collision operator $\frac{\Delta t}{\tau} \left(f_\alpha(\boldsymbol{x}, t) - f_\alpha^{eq} \right)$, called the collision step. The implementation requires q populations of f_α to be stored at each lattice location $(\boldsymbol{x}, t)$. In the collision step, each population $f_\alpha(\boldsymbol{x}, t)$ updated by the local collisions to become

$$f_\alpha^*(\boldsymbol{x}, t) = f_\alpha(\boldsymbol{x}, t) - \frac{\Delta t}{\tau} \left(f_\alpha(\boldsymbol{x}, t) - f_\alpha^{eq} \right). \tag{4.11}$$

In the streaming step, the collision updated population $\boldsymbol{f}_\alpha^*(\boldsymbol{x}, t)$ streams along the caharacteristics direction $\boldsymbol{v}_\alpha$ to populate the neighbouring lattice point $(\boldsymbol{x} + \boldsymbol{v}_\alpha \Delta \boldsymbol{t}, \boldsymbol{t} + \Delta \boldsymbol{t})$:

$$f_\alpha(x + v_\alpha \Delta t, t + \Delta t) = f_\alpha^*(x, t). \qquad (4.12)$$

In Figure 4.5, the effect of the streaming step for a inner node is illustrated.

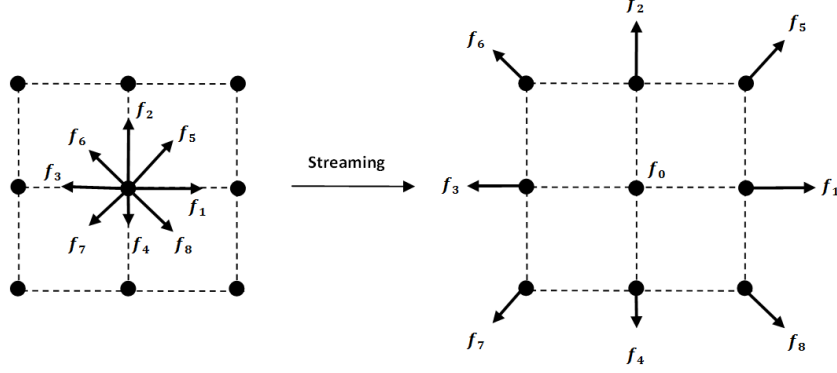*Figure 4.5.* *Streaming process of a lattice nodes (Bao et al., 2011).*

The velocity sets are chosen in such a way that any spatial vector $v_\alpha \Delta t$ points from one lattice site to a neighbouring lattice site. This guarantees that the populations f_α always reach another lattice site during a time step Δt, rather than being trapped between them.

4.5. Boundary Conditions in Lattice Boltzmann Method

Boundary conditions are very important for stability and precision in the numerical implementation. Macroscopic pressure and velocity fields are computed by using the particle population distribution in LBM. Therefore, the conventional boundary conditions of the fluid are to be specified in terms of the particle distribution function. This gives some degrees of freedom at the boundary lattice sites (Latt et al., 2008). Because of that, defining velocity and pressure boundary conditions at a certain node does not entirely describe the state of a boundary lattice site (Koda, 2013).

4.5.1. Bounce-Back Scheme

These boundaries, also called no-slip condition boundaries, are the typical boundaries for simulating the interaction of fluids with a non-moving wall without slip. They are also used to simulate the flow around a stationary obstacle. They are used largely because they ensure the mass, momentum and energy conservation (Mohamad, 2011) and due to their simplicity, numerical stability and accuracy.

As the name implies, when a particle is coming towards the solid boundary it bounces back into the flow domain (Ho et al., 2009) as seen in Fig. 4.6
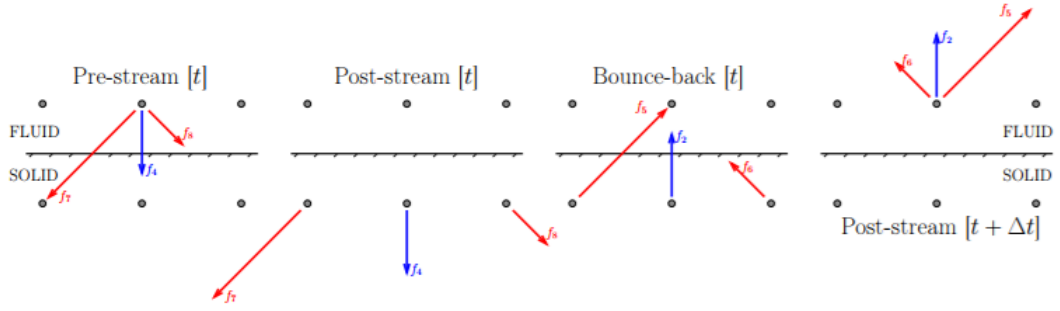

Figure 4.6. Bounce-back boundary condition effect on the distribution function values (Mele, 2013)

There are two basic approaches in implementing the bounce-back scheme, and they produce different results. The first one suggests that the solid boundary should be placed half way between the solid node and the fluid node as shown in the right-hand side of Fig. 4.7. The other scheme suggests placing the solid boundary on a node directly as shown in the left-hand side of Fig. 4.7. It has been shown that the first scheme is second-order accurate while the second scheme is only first-order accurate (Bao et al., 2011; Gallivan et al., 1997; Mele, 2013).

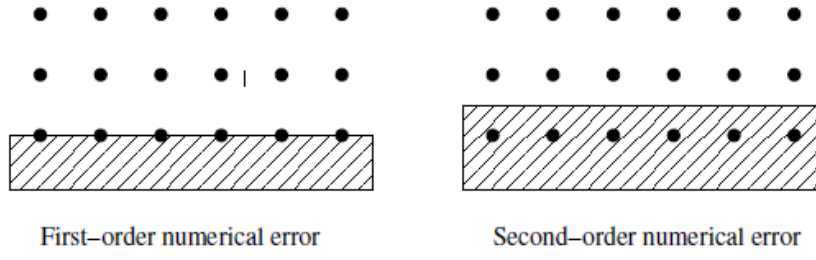First–order numerical error   Second–order numerical error

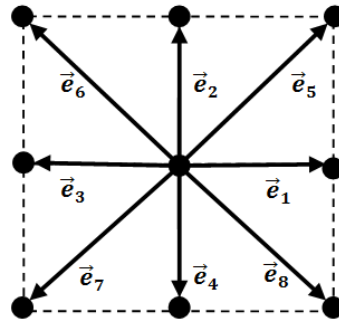*Figure 4.7.* *The two different approaches for bounce-back boundaries (Boix, 2013).*

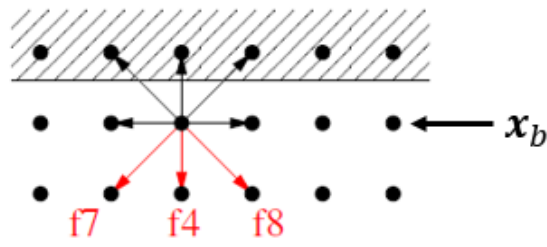*Figure 4.8.* *Illustration of D2Q9 model with nine lattice node. (Bao et al., 2011).*

Figure 4.9. *D2Q9 bounce-back boundary in the north direction (Boix, 2013).*

The bounce-back conditions for the first scheme can be formulated as

$$f_{\bar{\alpha}}(\boldsymbol{x}_b, t + \Delta t) = f_{\alpha}^*(\boldsymbol{x}_b, t) \tag{4.13}$$

where $\boldsymbol{x}_b$ refers to the fluid node at the boundary and $\bar{\boldsymbol{\alpha}}$ the direction index such that $\boldsymbol{v}_{\bar{\alpha}} = -\boldsymbol{v}_{\alpha}$. This is demonstrated using the lattice configuration D2Q9 in Figs. 4.8-4.9. If the node in contact with a boundary node is considered, it is shown in Fig. 4.9 that there are no streamed distribution function values from the solid node. Therefore, there are only three unknowns in the distribution function field at the fluid node, namely, f_4, f_7, and f_8. These values can be obtained by the bounce-back conditions

$$f_4 = f_2, \qquad f_7 = f_5, \qquad f_8 = f_6. \tag{4.14}$$

Thus, the streaming does not provide any values for f_4, f_7, and f_8, it is the bounce-back conditions (4.14) that provide the values for these unknowns at the boundary (Boix, 2013). The bounce-back conditions (4.13) for a wall moving with a velocity $\boldsymbol{u}_w$ can be modified to read

$$f_{\bar{\alpha}}(\boldsymbol{x}_b, t + \Delta t) = f_{\alpha}^*(\boldsymbol{x}_b, t) - 2w_{\alpha}\rho_w \frac{\boldsymbol{v}_{\alpha} \cdot \boldsymbol{u}_w}{c_s^2} \tag{4.15}$$

where ρ_w may be taken as the local fluid density at $\boldsymbol{x}_b$ (Krüger et al., 2016).

4.5.2. Zou-He Velocity and Pressure Boundary Conditions

In some problems, flow models come with specified pressure and velocity at the boundary. The LBM treatment of this specific pressure and velocity boundary conditions were firstly developed by Zou & He (Zou et al., 1997).

In the case of the given velocity $\boldsymbol{u}_L = (\boldsymbol{u}_x, \boldsymbol{u}_y)$ at the left wall in Fig. 4.10, after the streaming process, streaming $\boldsymbol{f}_0, \boldsymbol{f}_2, \boldsymbol{f}_3, \boldsymbol{f}_4, \boldsymbol{f}_6$ and $\boldsymbol{f}_7$ are known, while $\boldsymbol{f}_1, \boldsymbol{f}_5, \boldsymbol{f}_8$ and $\boldsymbol{\rho}$ are unknown.
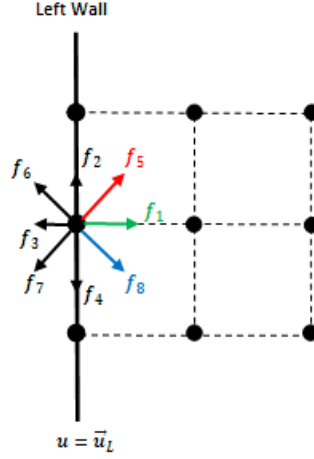
Figure 4.10. Illustration of Zou-He velocity BC (Bao et al., 2011)

Zou-He boundary conditions offer to formulate a linear system for f_1, f_5, f_8 and ρ by considering the equations (2.23a) and (2.23b). After rearrangement of the equations, one gets:

$$f_1 + f_5 + f_8 = \rho - (f_0 + f_2 + f_3 + f_4 + f_6 + f_7), \qquad (4.16a)$$

$$f_1 + f_5 + f_8 = \rho u_x + (f_3 + f_6 + f_7), \qquad (4.16b)$$

$$f_5 - f_8 = \rho u_y - f_2 + f_4 - f_6 + f_7. \qquad (4.16c)$$

By using (4.16a) and (4.16b), the density is determined as follows:

$$\rho = \frac{1}{1 - u_x} [f_0 + f_2 + f_4 + 2(f_3 + f_6 + f_7)]. \qquad (4.17)$$

A fourth equation needed to solve for f_1, f_5, f_8 is obtained based on the hyphothesis, suggested by Zou and He (Zou et al., 1997) that the bounce-back rule also holds for the non-equilibrium part of the distribution function normal to the boundary, i.e.

$$f_1 - f_1^{eq} = f_3 - f_3^{eq}. \qquad (4.18)$$

Once f_1 is determined from (4.18) with (4.3), the equations (4.16b-c) can be used to obtain f_5, f_8 as follows:

$$f_1 = f_3 + \frac{2}{3}\rho u_x \tag{4.19a}$$

$$f_5 = f_7 - \frac{1}{2}(f_2 - f_4) + \frac{1}{6}\rho u_x + \frac{1}{2}\rho u_y \tag{4.19b}$$

$$f_8 = f_6 + \frac{1}{2}(f_2 - f_4) + \frac{1}{6}\rho u_x - \frac{1}{2}\rho u_y \tag{4.19c}$$

Here, (4.19a) also follows from (4.15) by the use of (4.3).

If pressure (density) is specified on the boundary, (4.17) can be used to get

$$u_x = 1 - \frac{[f_0 + f_2 + f_4 + 2(f_3 + f_6 + f_7)]}{\rho}. \tag{4.20}$$

Now that f_1 is known from (4.19a), f_5, f_8 can be obtained similarly using (4.20).

4.6. Stability

The explicit discretization of the BGK-Boltzmann equation in (4.10) imposes some stability restrictions on the time step Δt and on the lattice constant $\Delta x = v_\alpha \Delta t$. The following argument may be used to obtain a stability constraint (Wolf-Gladrow, 2000): For an initially uniform flow, i.e. $f_\alpha(x, t_0) = f_\alpha(t_0)$, the kinetic equation becomes

$$f_\alpha(t + \Delta t) = f_\alpha(t) - \frac{\Delta t}{\tau}(f_\alpha(t) - f_\alpha^{eq}) \tag{4.21}$$

that is the flow will remain uniform at all later times. Furthermore, mass and momentum density are conserved and thus retain their initial value $\rho(x, t) = \rho(t_0) = \rho_0$ and $\rho(x, t)u(x, t) = \rho(t_0)u(t_0) = \rho_0 u_0$. Since the equilibrium distribution, f^{eq} does not depend on x and t explicitly, i.e. $f_\alpha^{eq} = f_\alpha^{eq}(\rho_0, u_0)$, we have

$$f_\alpha(t + \Delta t) = f_\alpha(t) - \frac{\Delta t}{\tau}(f_\alpha(t) - f_\alpha^{eq}(\rho_0, u_0)) \tag{4.22}$$

Subtracting $f_\alpha^{eq}(\rho_0, u_0)$ from both sides, it becomes

$$\tilde{f}_\alpha(t+1) = \left(1 - \frac{\Delta t}{\tau}\right)\tilde{f}_\alpha(t) \qquad (4.23)$$

where $\tilde{f}_\alpha(t) = f_\alpha(t) - f_\alpha^{eq}(\rho_0, u_0)$. Stability of the evolution requires the magnitude of $\tilde{f}_\alpha(t)$ does not increase with time, i.e. $\left|\tilde{f}_\alpha(t+\Delta t)\right| \leq \left|\tilde{f}_\alpha(t)\right|$. This is realized when $|1 - (\Delta t/\tau)| < 1$ or $\tau/\Delta t > 1/2$.

4.7. A Numerical Example: Steady-State Plane Poiseuille Flow and Grid Independence Study

Poiseuille flow is studied within the scope of Hagen-Poiseuille theory and developed from NS equations. In this theory, Poiseuille flow is considered to be incompressible and laminar.

It is one of the basic flow configurations to compare the numerical algorithms with the analytical results (Boix, 2013). Axial velocity profile of the flow pattern can be seen in Fig. 4.11.
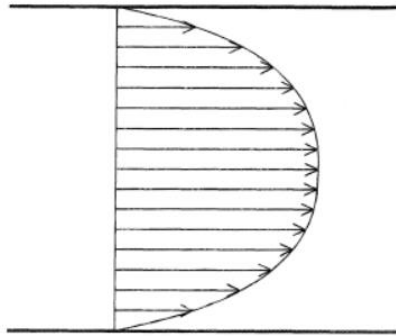

Figure 4.11. Axial velocity profile of the Poiseuille flow

The LBM-BGK model is applied for solving the plane Poiseuille flow. The flow is driven by a pressure gradient applied through the inlet and the outlet of the channel. Schematic of the flow geometry is given in Fig. 4.12.
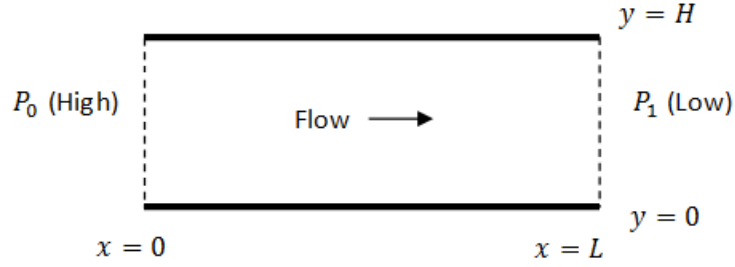

Figure 4.12. Schematic of Poiseuille flow (Bao et al., 2011)

In order to determine the exact solution, symmetry and incompressibility of the flow are used. Thus velocity components u and v do not have any horizontal variation and also we can consider v equal to zero. The Navier-Stokes equations then reduce to

$$\mu \frac{\partial^2 u}{\partial y^2} = \frac{\partial p}{\partial x} \tag{4.24}$$

where

$$\frac{\partial p}{\partial x} = \frac{P_1 - P_0}{L} \equiv \frac{\Delta P}{L}$$

The initial and boundary conditions are

$$u(x, y, 0) = v(x, y, 0) = 0; \quad p(x, y, 0) = P_{avg}$$
$$u(x, 0, t) = v(x, 0, t) = 0; \quad u(x, H, t) = v(x, H, t) = 0$$
$$p(0, y, t) = P_0; \quad p(L, y, t) = P_1$$

49

where P_0 is the inlet and P_1 is the outlet pressure at the channel and $P_{avg} = (P_0 + P_1)/2$. As a result, the exact solution to Poiseuille flow is obtained as:

$$u(x, y, t) = \frac{\Delta p}{2\mu L} y(y - H) \tag{4.25}$$

$$v(x, y, t) = 0 \tag{4.26}$$

After getting macroscopic conservation equations by integrating velocity moments of the BGK-Boltzmann equation, viscosity of the fluid can be described as below, in the light of Section 3.2:

$$\mu = \rho c_s^2 \left(\tau - \frac{1}{2}\right) \tag{4.27}$$

Thus, the relaxation paramater, τ, is related to the viscosity of the fluid.

In simulation, constant velocity profile applied at the inlet and the outlet of the channel and walls of the channel are no-slip boundaries. In the lattice, these conditions are converted to mesoscopic boundary conditions in terms of distribution functions as mentioned in Section 4.5. Density is determined by using Eq. 4.17 and $u_x \equiv u$ is determined by using Eq. 4.20.

The constant velocity at the inlet, after some distance, gets developed and velocity profile takes its final shape. We have taken $L=50$, $H=20$, viscosity of the fluid as 0.2 m/s^2. After 10000 iterations, the system achieved a stationarity and converging to the Poiseuille parabolic profile.

To analyze and compare this velocity profile with the analytical results, a grid convergence study is performed. For this, at the center of the channel, maximum velocity values for different spatial resolutions are used. In grid independence study, we also used Grid Convergence Index (CGI) based on the Richardson extrapolation, which is presented by Roache (1994). This is a method for obtaining a higher order approximation of a quantity from a series of lower order discrete values. The CGI, however, is a measure of how far the computed value is away from the value of the asymptotic numerical value as $h \to 0$. A small value of CGI indicates that the computation is within the asymptotic range.

We calculate the CGI for fine-medium and medium-coarse mesh to compare the grid resolutions and consider the accuracy of the solution as mentioned in Jozsa et al. (2016).

For this study, maximum velocity at the center of the channel generated by the LBM simulations with BGK collision model are used labelled by u_1, u_2, u_3 in the order of decreasing resolution and the order of convergence p is calculated as follow:

$$p = ln\left(\frac{(u_3 - u_2)}{(u_2 - u_1)}\right)/ln(r) \qquad (4.28)$$

where r is the grid refinement ratio. Based on this order of convergence, the asymptotic value $u_{h \to 0}$ as zero grid spacing is approached can be estimated by using the formula

$$u_{h \to 0} = u_1 + \frac{u_1 - u_2}{r^p - 1} \qquad (4.29)$$

that uses the computed centerline velocity values u_1, u_2 on two grid spacing h_1 and h_2 (h_1 is the finer spacing). Here, r is h_2/h_1 where in our case it is equal to 3. We get the $h \to 0$ value as 0.20747 which is the result of Richardson extrapolation.

To find grid convergence quality, grid convergence index is calculated between the refinement steps. We calculated the CGI over three grids for coarse to medium (3 to 2) and medium to fine (2 to 1) as follow:

$$CGI = \frac{F_s|e|}{r^p - 1} \qquad (4.30)$$

where F_s is the safety factor chosen as 1.25 as in the literature (Roache, 1994). and e is the error between each grid calculated by $(u_2 - u_3)/u_2$ for medium to coarse grid and $(u_1 - u_2)/u_1$ for fine to medium grid.

The asymptotic range of convergence, defined by,

$$\frac{CGI_{2,3}}{r^p x CGI_{1,2}} \cong 1 \qquad (4.31)$$

can then be used to check the asymptotic range of convergence, which should be approximately 1 for the solutions to be well within the asymptotic range of convergence.

All calculated values are given in Table 4.2 for this grid convergence study. All values have been given for three different grid spacing. The CGI and the evident order is given from the coarse to medium and medium to fine mesh. As can be seen on Table 4.2, $u/u_{max} \cong 1$ and we choose the square grid of size 150x60.

Table 4.2. *Grid convergence study*

	u/u_{max}			$CGI_{1,2}$	$CGI_{2,3}$	asymptotic range of convergence
n_x x n_y	17 x 7	50 x 20	150 x 60			
	0.9900	0.9975	0.99436	1.78192	1.41426	1.01951

As shown in the Fig. 4.13, computed velocity profile matches closely with the analytical solution.
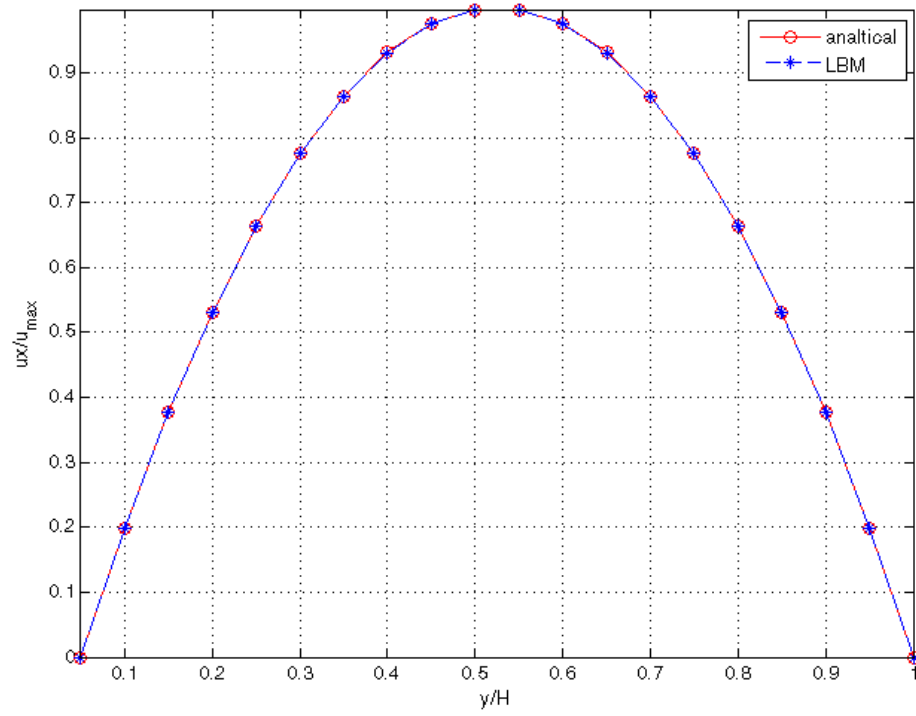

Figure 4.13. Schematic of Poiseuille flow

CHAPTER 5

FURTHER NUMERICAL EXAMPLES USING THE LATTICE BOLTZMANN METHOD

In this thesis, LBM is applied to circular and square cylinders in the form of arrays to simulate flow characteristic. Velocity contours are plotted for flow visualization. For characterizing the flow, parameters such as lift and drag coefficients are computed and compared with the results in the literature.

5.1. Simulation of Flow Past a Circular Cylinder

The incompressible flow past a bluff body like a stationary cylinder is a classical problem in fluid mechanics which has been studied for years (Roshko, 1954), (Tritton, 1959). With its physics and a many applications, it attracted researchers for over decades and various theoretical and experimental investigations have been performed on this problem. In spite of its simple geometry, the flow past a circular cylinder problem is studied as a reference model for more complex flows (Sen et al., 2009).
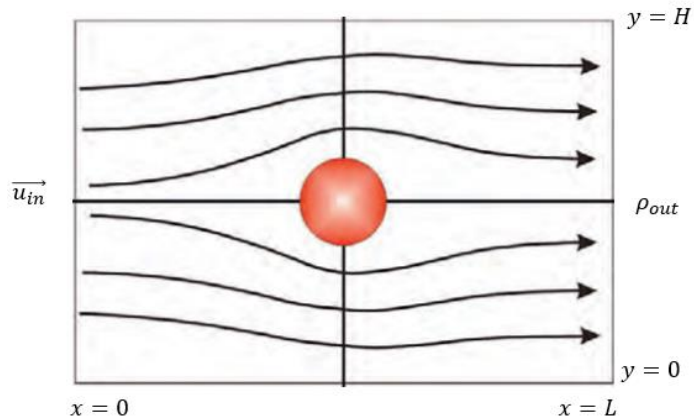
Figure 5.1. Illustration of flow past a cylinder

When the Reynolds number is small, the flow is laminar as depicted in Fig. 5.1. However if Reynolds number exceeds a critical value, the laminar flow loses its stability and some vortices appear in the wake.

Before presenting numerical simulation of the flow past a circular cylinder, here are some physical and analytical descriptions of the flow:

In laminar flow, the fluid in the boundary layer over the cylinder surface moves slower that the fluid outside the layer. Increasing the flow speed causes flow separation and in turn triggers swirling eddies in the wake region behind the cylinder known as the Karman vortex street. (von Kármán, 1911)

For flow past a cylinder, Reynolds number is defined as

$$Re = \frac{U_\infty D}{v} \qquad (5.1)$$

where U_∞ is the free-stream velocity and D is the cylinder diameter and v is the kinematic viscosity. It is an important quantity characterizing the flow behavior, such as laminar, transitory or turbulent.

Strouhal number is another dimensionless number which characterizes the vortex shedding frequency and defined as

$$St = \frac{f_s D}{U_\infty} \qquad (5.2)$$

where f_s is the vortex shedding frequency. Around approximately $Re \cong 49$, the Strouhal number shows a sharp transition (Khan, 2011).

In some previous experimental studies (Norberg, 1987; Roshko, 1954) a relation between Reynolds and Strouhal numbers was established. With these experimental results, researchers were able to provide a fit for this relation at stable flow regimes. However, for the irregular flow regimes, Strouhal number was observed to be unpredictable due the nature of the underlying fluid motion (Khan, 2011).

After these studies, a very precise fit was obtained by Henderson (1995) for the Reynolds and Strouhal number relationship up to $Re = 1000$. This relation is;

$$St = 0.2417 - 0.8328 Re^{-0.4808} \exp(-0.001895 Re) \qquad (5.3)$$

For flow around a circular cylinder, a relationship for the drag coefficient, C_D, (Roshko, 1954) in a two-dimensional flow, can be expressed as

$$C_D = \frac{2 F_x}{\rho U_\infty^2 D} \qquad (5.4)$$

where F_x is the sum of pressure and viscous forces on the surface of the cylinder acting along the flow direction.

Similarly, the lift coefficient is defined as

$$C_L = \frac{2 F_y}{\rho U_\infty^2 D} \qquad (5.5)$$

where F_y is the force on the surface of the cylinder acting perpendicular to the flow direction.

Drag and lift coefficients give a dimensionless idea of the force which is exerted on the obstacle along and normal to the flow's direction (Portinari, 2015).

For stability of the LBM with BGK collision operator, $|\boldsymbol{u}_{max}|(\tau)$ denotes the stability map. Before the occurrence of instability, this map shows us maximum possible velocity magnitude for a given relaxation time τ. The sufficient condition for numerical stability in LBM-BGK is $\tau/\Delta t \geq 1/2$, as long as $f_a^{eq} \geq 0$ for all a (See Eqn. 4.23). By using Eqn. 4.4, we can provide the following bound:

$$|\boldsymbol{u}_{max}| < \sqrt{\frac{1}{3}\frac{\Delta x}{\Delta t}} \approx 0.577\frac{\Delta x}{\Delta t} \tag{5.6}$$

for the $\boldsymbol{u}_{max}$. In addition, the optimal stability condition $\tau/\Delta t \geq 1$ can be stated for the BGK collision operator, as long as if $f_0^{eq} > 0$. From these relations, the velocity magnitude condition can be obtained as (Krüger et al., 2016):

$$|\boldsymbol{u}_{max}| < \sqrt{\frac{2}{3}\frac{\Delta x}{\Delta t}} \tag{5.7}$$

As a result, the maximum velocity magnitude $|\boldsymbol{u}_{max}|$ remains bounded under two stability conditions. Namely, sufficient stability condition for $1/2 < \tau/\Delta t$ and optimal stability condition for $\tau/\Delta t \geq 1$.

For circular cylinder case, we consider a 2D channel with a steady Poiseuille flow and applied D2Q9 lattice configuration. The circular cylinder obstacle has a diameter D and is immersed on the vertical center in a rectangular channel (Fig. 5.1). This channel has 15D length and 6D height. We initialise the system by taking $f_a(\boldsymbol{x}, t = 0) = f_a^{eq}(\rho = 1, \boldsymbol{u} = 0)$. The maximum velocity of the inlet profile set as $u_{max} = 0.1$ which is the maximum velocity per unit lattice for each time step.

Bounce-back BCs, are applied on the cylinder as well as at the upper and lower no slip walls of the channel. At the inlet, pressure driven fully developed flow condition is applied. The inlet region was chosen to be long enough (3D length) to avoid long transitory time and to improve convergence performance. At the outlet, uniform pressure profile is applied.

The bounce-back scheme at walls is applied as shown in Fig. 5.2 for the lower wall

$$f_2(x, y_1, t + \Delta t) = f_4^*(x, y_1, t + \Delta t),$$
$$f_5(x, y_1, t + \Delta t) = f_7^*(x, y_1, t + \Delta t), \tag{5.8}$$
$$f_6(x, y_1, t + \Delta t) = f_8^*(x, y_1, t + \Delta t).$$

and for the upper wall:

$$f_4(x, y_1, t + \Delta t) = f_2^*(x, y_N, t + \Delta t),$$
$$f_7(x, y_1, t + \Delta t) = f_5^*(x, y_N, t + \Delta t), \tag{5.9}$$
$$f_8(x, y_1, t + \Delta t) = f_6^*(x, y_N, t + \Delta t).$$
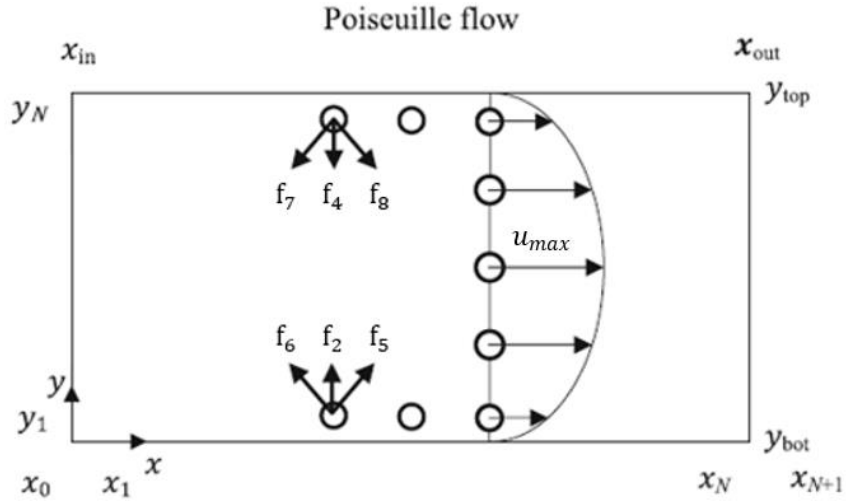

Figure 5.2. *Poiseuille flow with boundary populations (Krüger et al., 2016).*

For the inlet and outlet, we imposed open boundary conditions. This makes computational domain compatible with the physics of the problem, namely transparent boundaries. For the implementation of the open boundaries, a method similar to the bounce back method is applied which is called anti-bounce back method defined by

$$f_{\bar{\alpha}}(\boldsymbol{x}_b, t + \Delta t) = -f_{\alpha}^*(\boldsymbol{x}_b, t) + 2w_{\alpha}\rho_w \left[1 + \frac{(\boldsymbol{v}_{\alpha} \cdot \boldsymbol{u}_w)^2}{2c_s^4} - \frac{(\boldsymbol{u}_w)^2}{2c_s^2}\right] \quad (5.10)$$

where the boundary is located $\Delta x/2$ outside the boundary node. $\boldsymbol{u}_w$ is estimated by $\boldsymbol{u}_w = \boldsymbol{u}(\boldsymbol{x}_b) + 1/2[\boldsymbol{u}(\boldsymbol{x}_b) - \boldsymbol{u}(\boldsymbol{x}_{b+1})]$, where $\boldsymbol{x}_b$ and $\boldsymbol{x}_{b+1}$ are the boundary node and its neighbour along inward normal to the boundary. To find ρ_w, bounce back rule is used as in Eqn. 4.15.

By setting $p_{out} = 1$, inlet pressure can be written as $p_{in} = p_{out} + \Delta p$. By relating pressure and u_{max}, which is chosen above, pressure difference can be defined as (see Fig. 5.2) (Krüger et al., 2016)

$$\frac{\Delta p}{x_{out} - x_{in}} = \frac{8\mu u_{max}}{(y_{top} - y_{bot})^2} \quad (5.11)$$

When applying curved boundary conditions, we used staircase approximation of the boundary and the bounce back scheme. As can be seen in Fig. 5.3, white circles represent the exterior fluid nodes, grey circles represent the external boundary nodes and black circles represent the solid nodes. Populations moving through v_a from x_b to x_s bounce back at x_w.
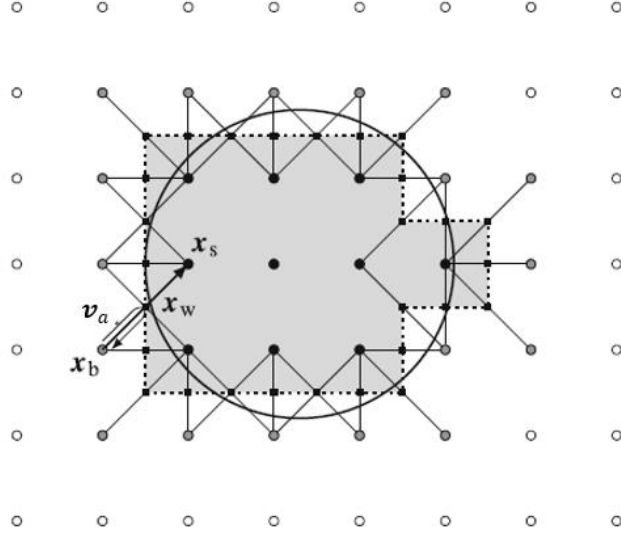
Figure 5.3. Representation of the staircase approximation of a circular cylinder (Krüger et al., 2016).

In using Eqn. 4.15, halfway bounce back scheme requires the identification of all lattice links, $\boldsymbol{v}_a$. A post collision population $f_\alpha^*(\boldsymbol{x}_b, t)$ which would propagate through a wall from a boundary node $\boldsymbol{x}_b$ to a solid node $\boldsymbol{x}_s = \boldsymbol{x}_b + \boldsymbol{v}_\alpha \Delta t$ is instead reflected half-way to the solid node at the wall location $\boldsymbol{x}_w = \boldsymbol{x}_b + 1/2\boldsymbol{v}_\alpha \Delta t$ and returns to $\boldsymbol{x}_b$. $\boldsymbol{u}_w = \boldsymbol{u}(\boldsymbol{x}_w, t + 1/2\Delta t)$ is the velocity of the wall, ρ is the fluid density at $\boldsymbol{x}_w$ and the index $\bar{a}$ defines $\boldsymbol{v}_{\bar{a}} = -\boldsymbol{v}_\alpha$. In practical implementations, ρ is often taken as the fluid density at $\boldsymbol{x}_b$.

In the following simulations, 150 grid points in x-direction and 60 grid points in y-direction are used with time step value of 0.04.

In the light of Eqn. 4.27, Reynolds number can be written as (Krüger et al., 2016)

$$Re = \frac{DU}{v} = \frac{DU}{c_s^2 \left(\tau - \frac{1}{2}\right)} \tag{5.12}$$

For the values $Re = 100$ and $c_s = \frac{1}{\sqrt{3}}$ (see Eqns. 4.3 and 4.4), the relaxation parameter τ is calculated as 0.56 where the viscosity of the fluid is 0.02. With these values, optimal stability condition, $\tau/\Delta t \geq 1$, is satisfied in this case. (see Section 4.6)

For this case, corresponding computed vorticity contours at a predifined time are shown in Fig. 5.4.
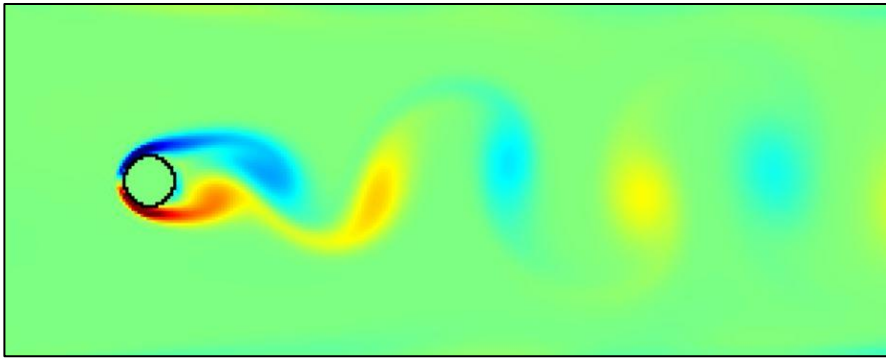

Figure 5.4. Vorticity contours of flow past a circular cylinder at Re=100

In order to see the flow developing, drag and lift coefficient values, which are given in Figs. 5.5 and 5.6, are calculated by using F_x and F_y. These force values are computed using the simulation flow field.
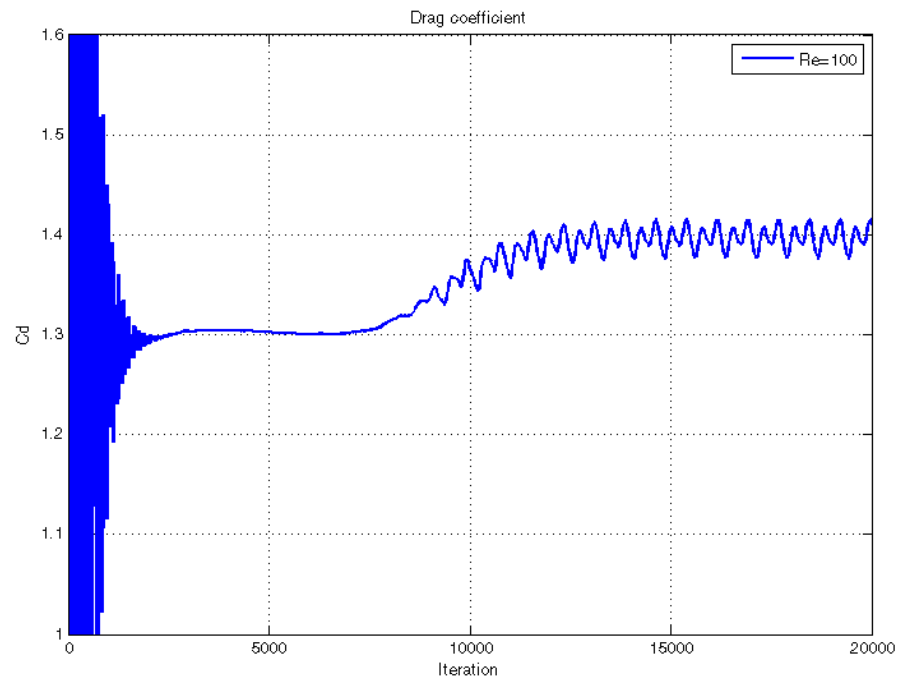
Figure 5.5. *Time history of drag coefficient for circular cylinder for Re=100.*
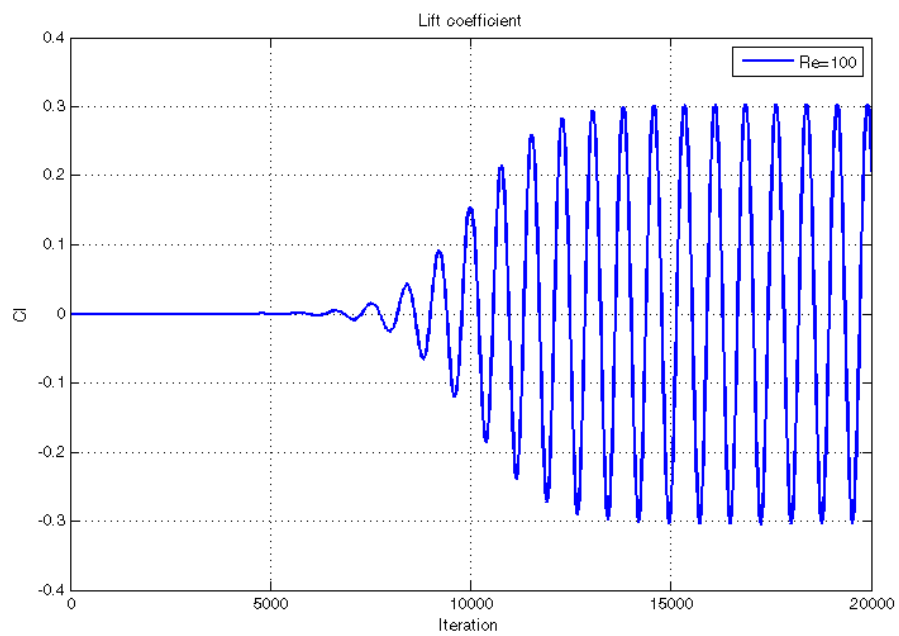

Figure 5.6. *Time history of lift coefficient for circular cylinder for Re=100.*

63

After the transients die down and the flow becomes developed, time series of the drag and lift coefficient values are shown in Figs. 5.7 and 5.8.
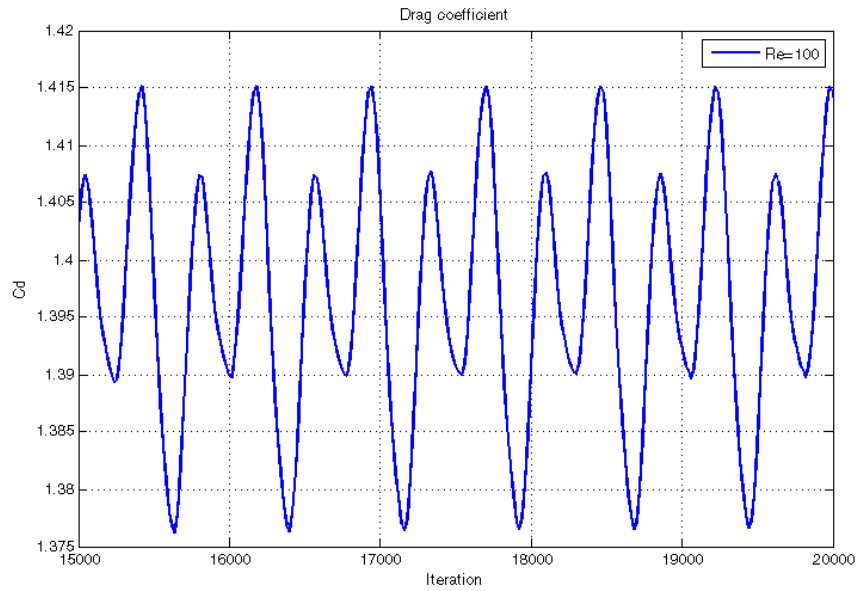

Figure 5.7. *Drag coefficient for circular cylinder between 15000-20000 iteration for Re=100.*
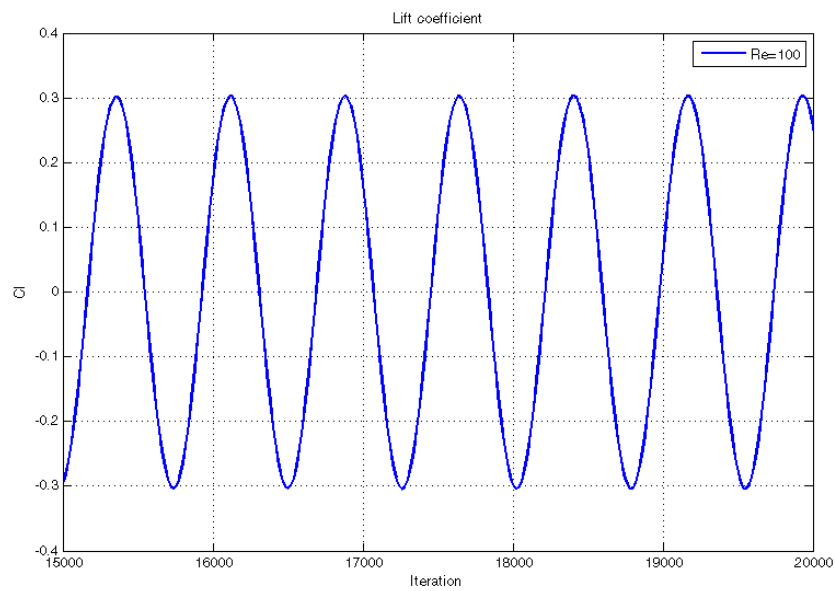

Figure 5.8. *Lift coefficient for circular cylinder between 15000-20000 iteration for Re=100.*

64

As another numerical experiment, Reynolds number is set at $Re = 200$ while the corresponding relaxation parameter τ is equal to 0.53. The corresponding vorticity contours at a predifined time is shown in Fig. 5.9.
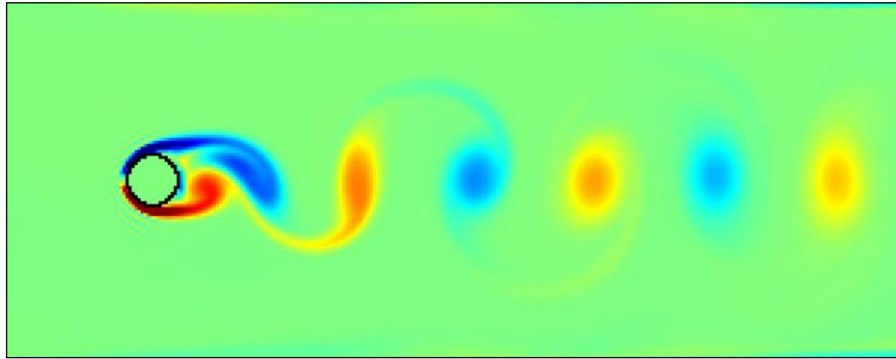

Figure 5.9. Vorticity contours of flow past a circular cylinder for Re=200

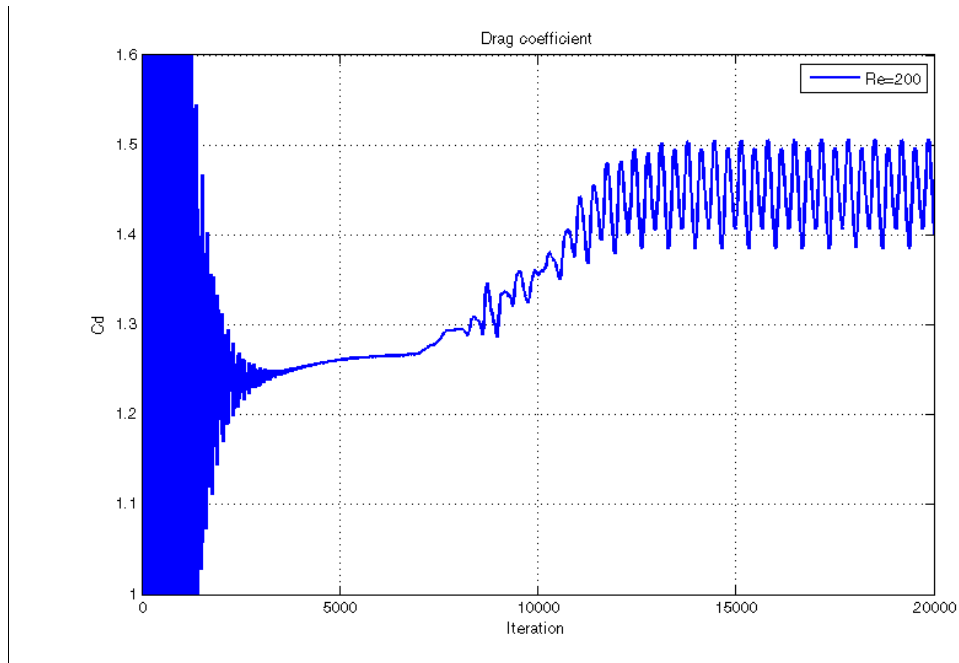Similarly, the developing and developed time series of the drag and lift coefficients are shown in Figs. 5.10 to 5.13.

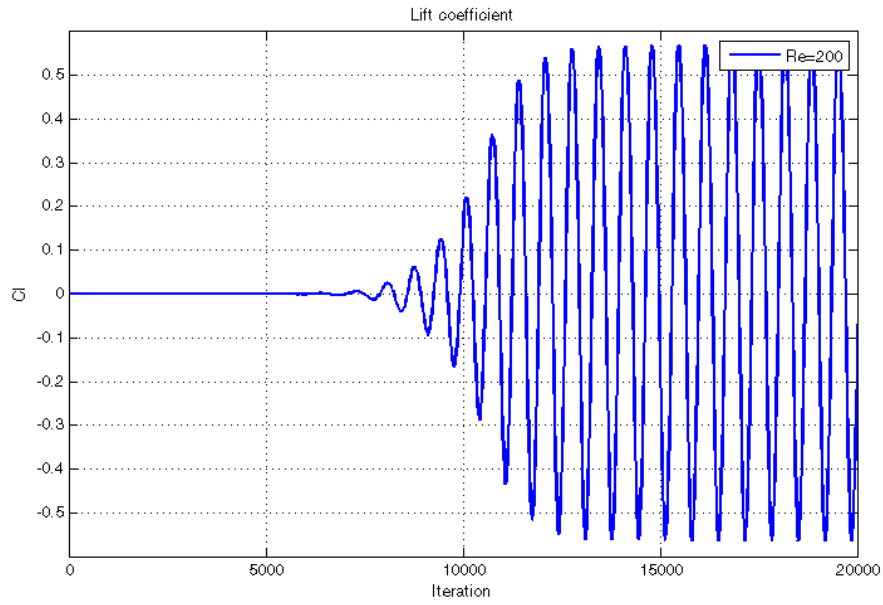*Figure 5.10. Time history of drag coefficient for circular cylinder for Re=200.*

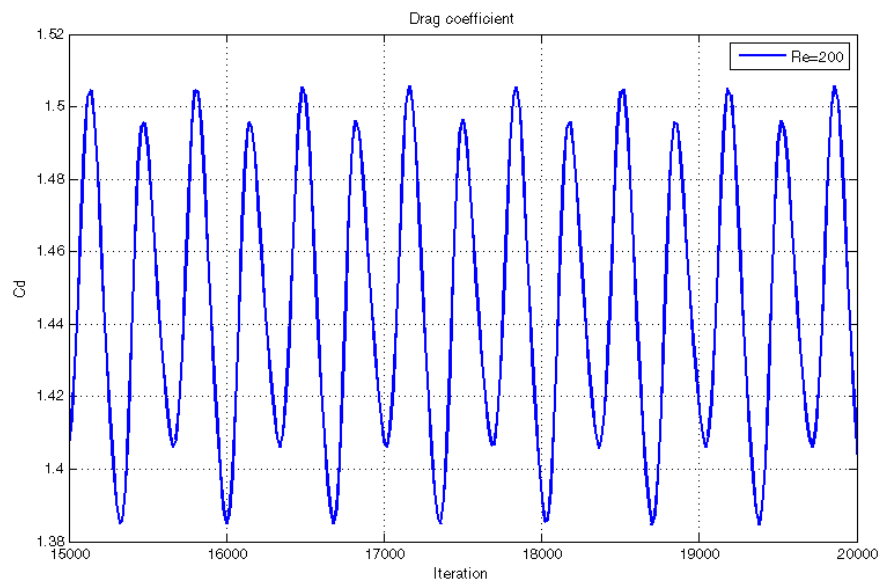*Figure 5.11.* *Time history of lift coefficient for circular cylinder for Re=200.*

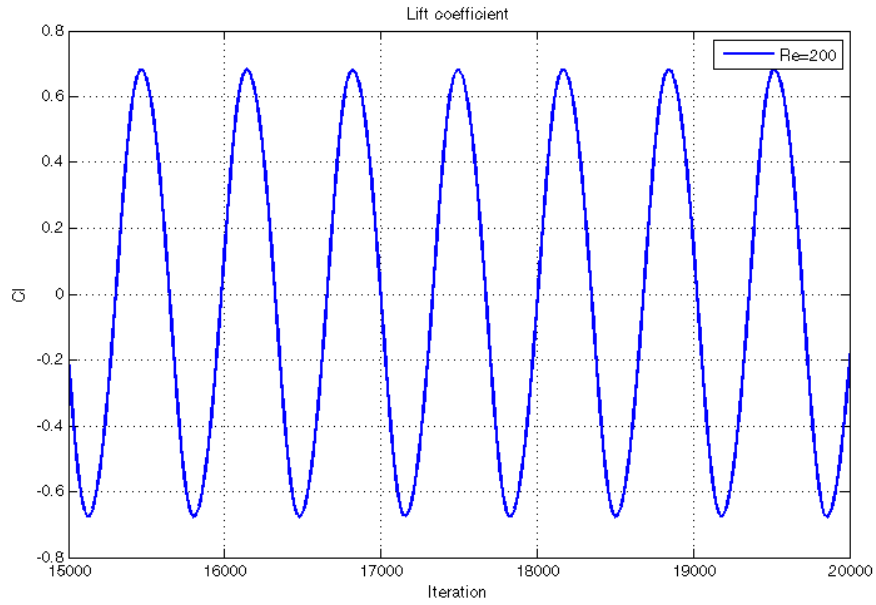*Figure 5.12.* *Drag coefficient for circular cylinder between 15000-20000 iteration for Re=200.*

66

Figure 5.13. Lift coefficient for circular cylinder between 15000-20000 iteration for Re=200.

Karman vortices demonstrated clearly with both cases $Re = 100$ and $Re = 200$. At the rear of the obstacle, drag and lift coefficients data show periodic vortex shedding alternating between the top and the bottom of the wake region. With increasing the Reynolds number, drag and lift coefficients and Strouhal number values are increased as expected.

In order to determine the dominant frequency in the vortex shedding phenomena, a frequency analysis of the time series data of the lift coefficient is performed. This is done using the FFT (fast Fourier transform) function of MATLAB. Using the frequency information, the Strouhal number is computed.

Frequency spectra are shown in Figs. 5.14 and 5.15 for Re=100 and Re=200, respectively.
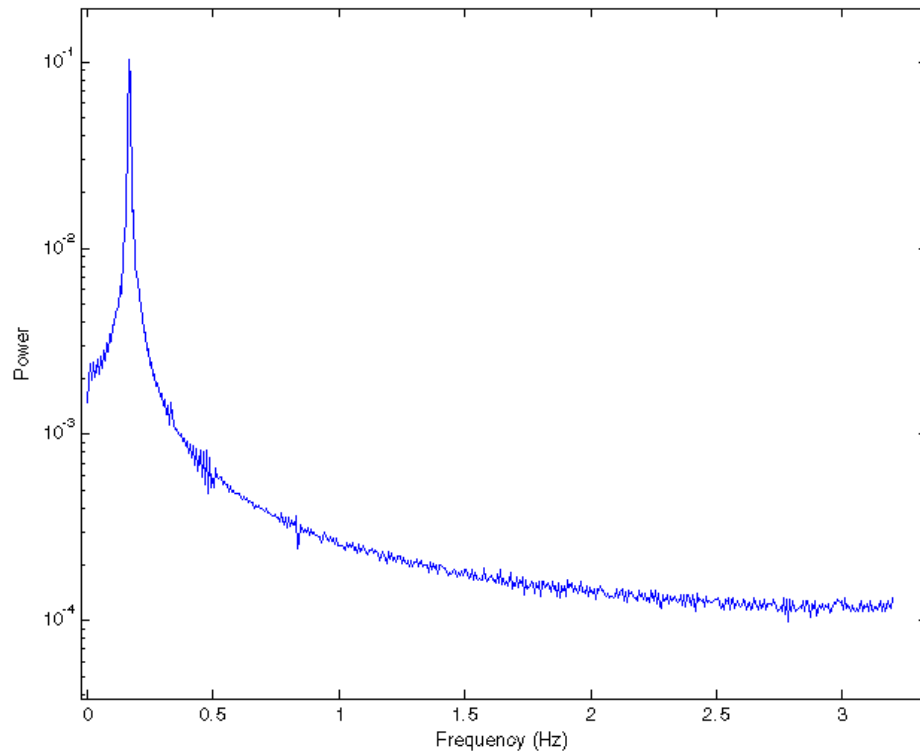
Figure 5.14. Frequency spectrum of the lift coefficient for flow past a circular cylinder for Re=100

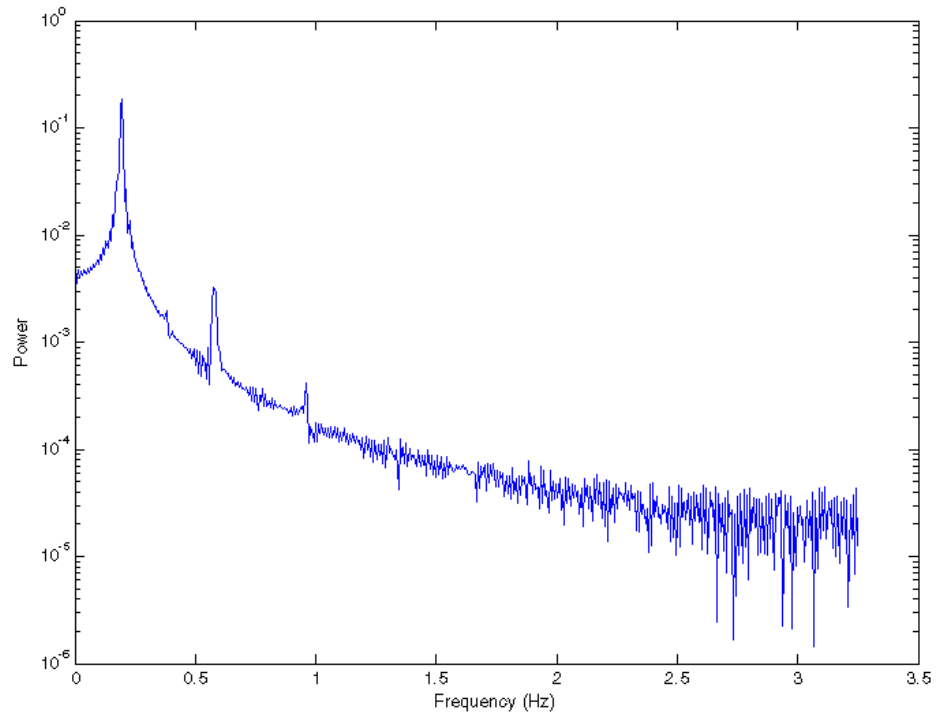*Figure 5.15. Frequency spectrum of the lift coefficient for flow past a circular cylinder for Re=200*

Our simulation results for the drag and lift coefficients and Strouhal number values for both cases can be seen in Table 5.1. In this table, mean and fluctuating components of these coefficients are shown in comparison to the other studies in literature for $Re = 100$ and $Re = 200$.

Table 5.1. *Flow parameters for flow field around single circular cylinder at Re=100 and 200.*

Parameters	Drag coefficient (C_D)		Lift coefficient (C_L)		Strouhal number (St)	
	Re=100	Re=200	Re=100	Re=200	Re=100	Re=200
Meneghini et. al. (2001)	1.370±0.010	1.30±0.05	-	-	0.165	0.196
Ding et al. (2007)	1.356±0.010	1.348±0.05	±0.287	±0.659	0.166	0.196
Braza et al. (1986)	1.364±0.015	1.40±0.05	±0.250	±0.750	0.160	0.200
Tritton (1959)	1.320±0.010	-	-	-	0.160	-
Wiesenberger (1923)	1.326±0.010	-	-	-	0.1608	-
Gresho et al. (1978)	1.816±0.010	-	-	-	0.18	-
Harichandan & Roy(2010)	1.352±0.010	1.32±0.05	±0.278	±0.602	0.161	-
Present study	1.396±0.019	1.44±0.06	±0.303	±0.680	0.166	0.195

In circular cylinder case, the flow parameters match reasonably well with the other studies in literature as can be seen in Table 5.1 considering the relative ease of the LBM simulation.

5.2. Simulation of Flow Past a Square Cylinder

Varioue studies on the flow development in the wake of a bluff body and vortex shedding behind the square cylinder have been performed both experimentally and numerically (Arnal et al.,1991), (Sohankar et al.,1998).

Reynolds number controls the transition to different flow regimes. For small Reynolds number, viscous forces keep the flow adhere to the obstacles. Flow seperation does not occur. By increasing the Reynolds number, von Karman periodic vortices occurs behind the obstacle around Re=60 and for Re<300. The vortex shedding is generally

a two dimensional phenomena (Breuer et al., 2000). In this study, Reynolds numbers are choosen within these limits.

For square cylinder case, we again use a 2D channel with a steady Poiseuille flow and applied D2Q9 lattice configuration. In this simulation, the ratio of size D of the square cylinder to the height of the channel is 1/6 and this gives a blockage ratio equal to 0.166. Furthermore, the channel length is 15D and the square obstacle is placed at the center along the y direction. We initialise the system by setting $f_a(x, t = 0) = f_a^{eq}(\rho = 1, \boldsymbol{u} = 0)$. The maximum velocity of the inlet profile set as $u_{max} = 0.1$ which is the maximum velocity per unit lattice for each time step.

In these cases, 150 grid points in x-direction and 60 grid points in y-direction are used with time step of 0.04.

In order to find the relaxation parameter, Eqn. 4.27 is used, where the value of c_s is taken equal to $\frac{1}{\sqrt{3}}$ (see Eqns. 4.3 and 4.4). Relaxation parameter τ is calculated to be 0.56 where the viscosity of the fluid is equal to 0.02. With these values, optimal stability condition, $\tau/\Delta t \geq 1$, is satisifed for this case (see Section 4.6). By using Eqn 5.12, Reynolds number is set at $Re = 100$.

Bounce-back BCs are applied on the square cylinder as well at the upper and lower no slip walls of the channel. At the inlet, parabolic velocity profile is imposed for simulating a fully developed laminar velocity profile. The inlet region was chosen to be long enough to improve convergence performance. At the outlet, constant pressure is applied. When appyling bounce back scheme, Eqns. 5.8 to 5.11 are used for this case as before.

In square cylinder case, we had to deal with corners. Despite these corners cover a few points in the domain, they should be treated carefully for an accurate numerical simulation. In order to do this, bounce back scheme is applied for straight walls and for corners in the same way. The unknown corner populations are determined by the full reflection of the incoming known populations by using Eqn. 4.13. Applying bounce back rule at the corner has the same advantages and disadvantages as in the case of planar surfaces. The positive aspects remain to be the simplicity of implementation, strict conservation of mass and good stability characteristics. However, posibility for the lower accuracy and the viscosity dependent errors remain to be the major disadvantages of this model.

If we take the left bottom corner of the obstacle, for example, after the streaming step f_3, f_4 and f_7 are known, and density is specified, the bounce back rule for non equilibrium part of the particle distribution function can be used to determine f_1, f_2, f_5, f_6 and f_8 as follows:

$$f_1 = \left(f_1^{eq} - f_3^{eq} \right) + f_3 = f_3 \qquad (5.13)$$

$$f_2 = \left(f_2^{eq} - f_4^{eq} \right) + f_4 = f_4 \qquad (5.14)$$

and by inserting the values of f_1 and f_2 from Equetions 4.13 and 4.16b,

$$f_5 = f_7 \qquad (5.15)$$

$$f_6 = f_8 = \frac{1}{2}[(f_0 + f_1 + f_2 + f_3 + f_4 + f_5 + f_7) - \rho]. \qquad (5.16)$$

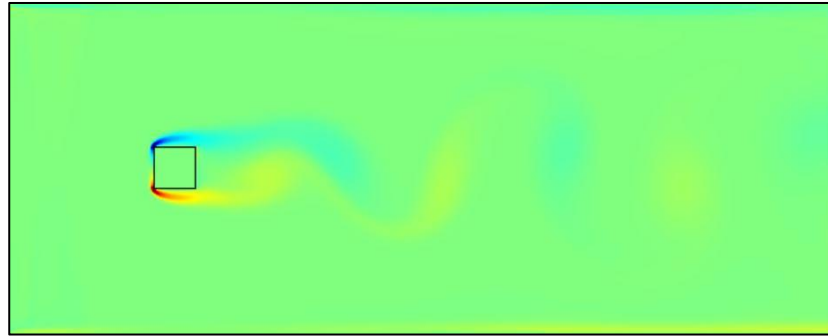For $Re = 100$, the vorticity contours are given in Fig. 5.16

Figure 5.16. Vorticity contours of flow past a square cylinder for Re=100.

In order to understand the behaviour of the fluid, drag and lift coefficient values are shown Figs. 5.17 and 5.18 as they develop from the beginning of the simulation.
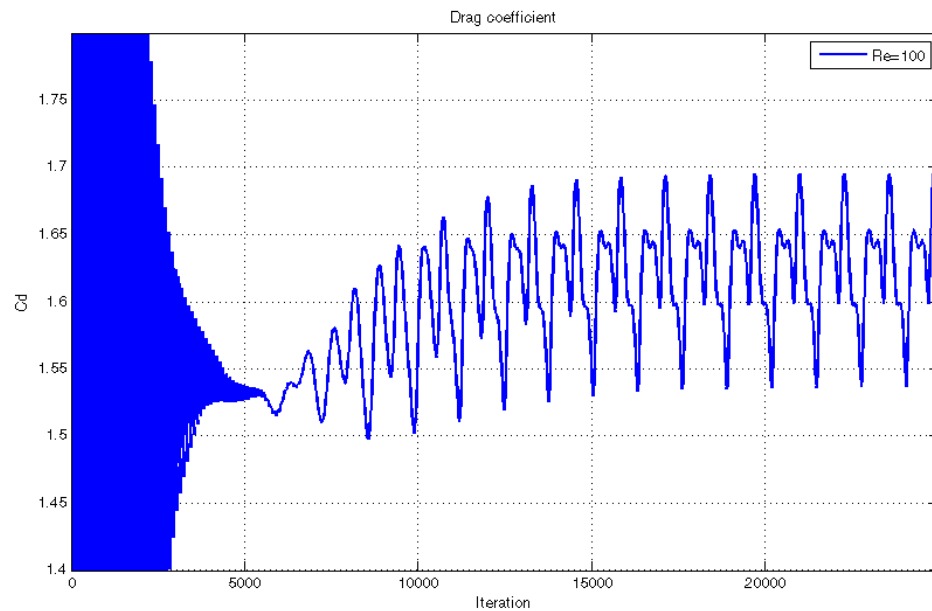

Figure 5.17. Time history of drag coefficient for square cylinder for Re=100.
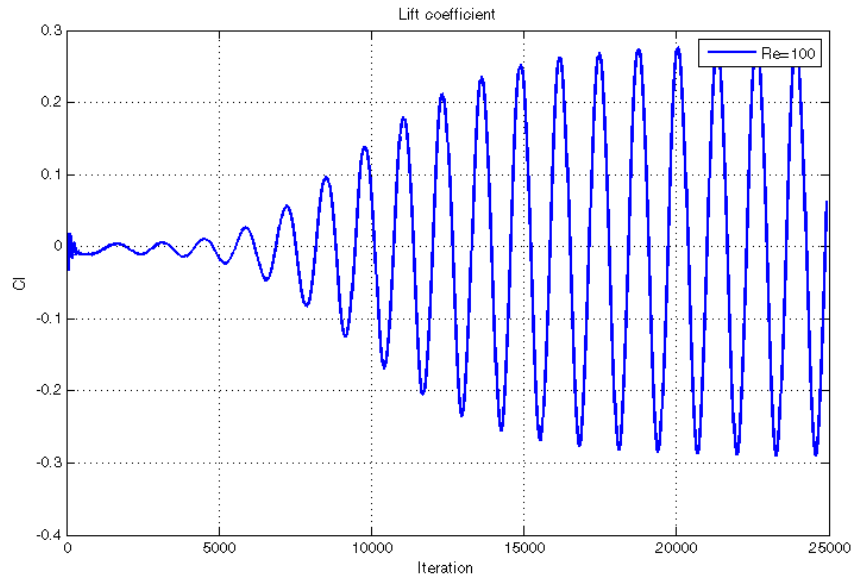
73

Figure 5.18. *Time history of lift coefficient for square cylinder for Re=100.*

After the flow develops, drag and lift coefficient values are shown in Figs. 5.19 and 5.20.

Figure 5.19. *Drag coefficient for square cylinder between 15000-20000 iteration for Re=100.*

Figure 5.20. Lift coefficient for square cylinder between 15000-20000 iteration for Re=100.

Next, Reynolds number is set at $Re = 200$ while the relaxation parameter τ is taken as 0.53 using Eqn. 5.12. Corresponding flow field is shown in Fig. 5.21.
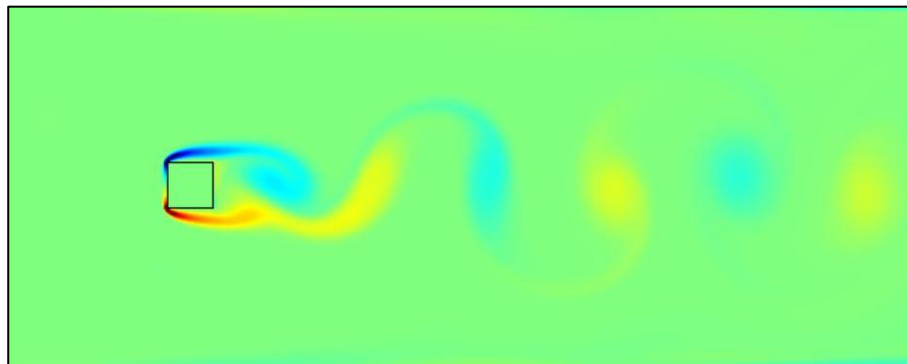
Figure 5.21. Vorticity contours of flow past a square cylinder for Re=200.

75

Similarly, the development of the drag and lift coefficient values are shown Figs. 5.22 and 5.23 from the beginning of the simulation.
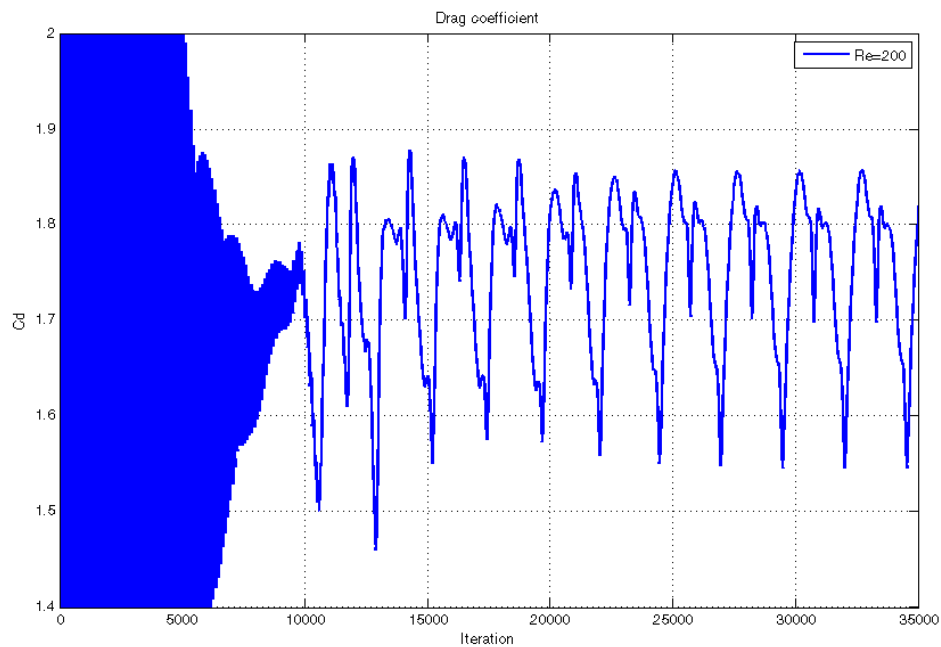
Figure 5.22. *Time history of drag coefficient for square cylinder for Re=200.*

Figure 5.23. *Time history of lift coefficient for square cylinder for Re=200.*

The developed drag and lift coefficient values are shown in Figs. 5.24 and 5.25.
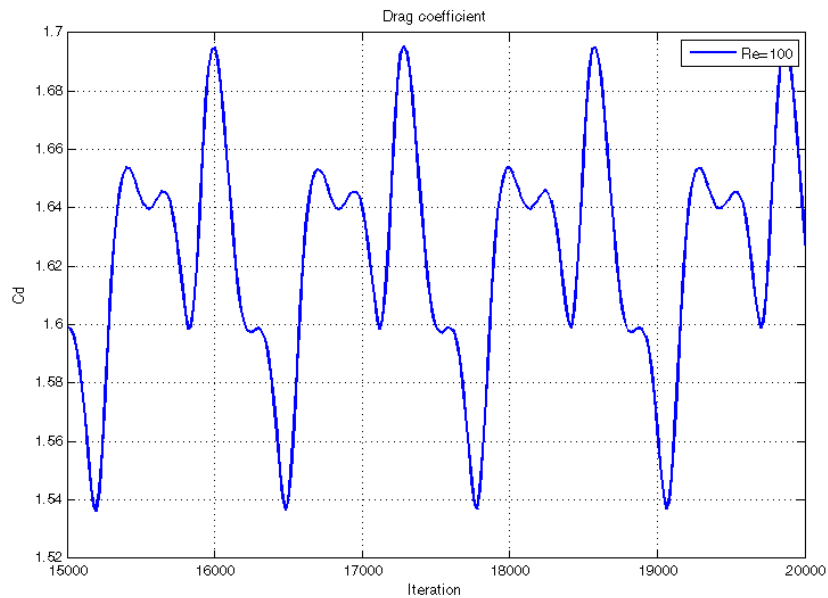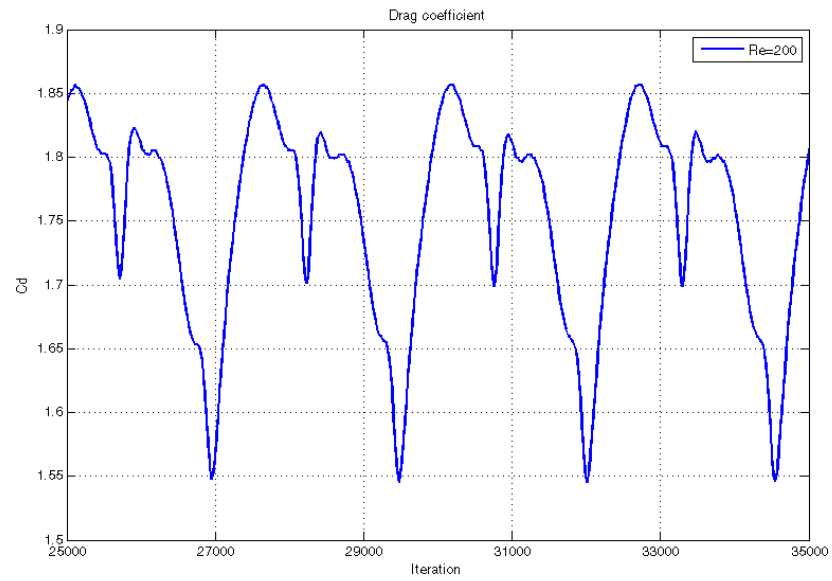

Figure 5.24. *Drag coefficient for square cylinder between 25000-35000 iteration for Re=200.*
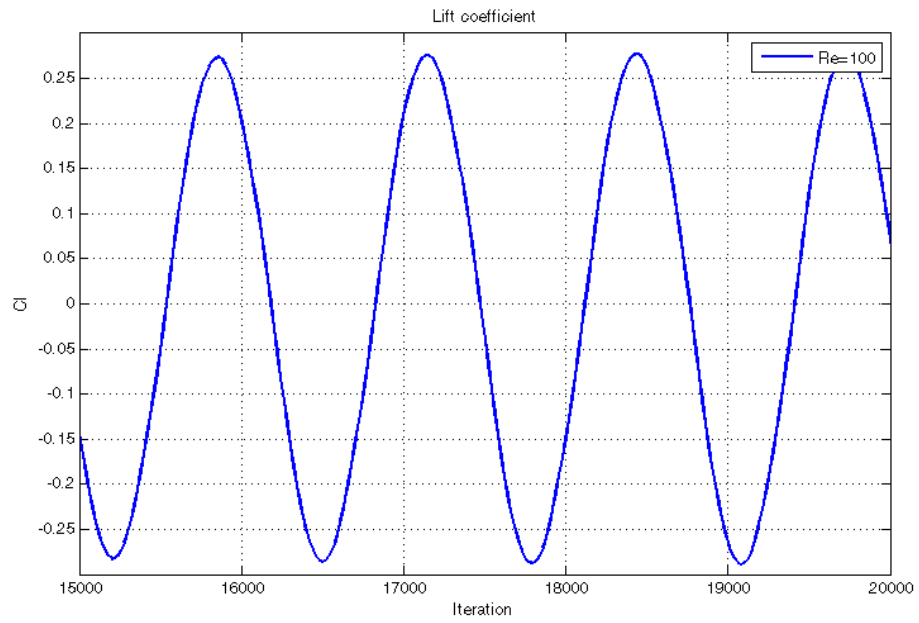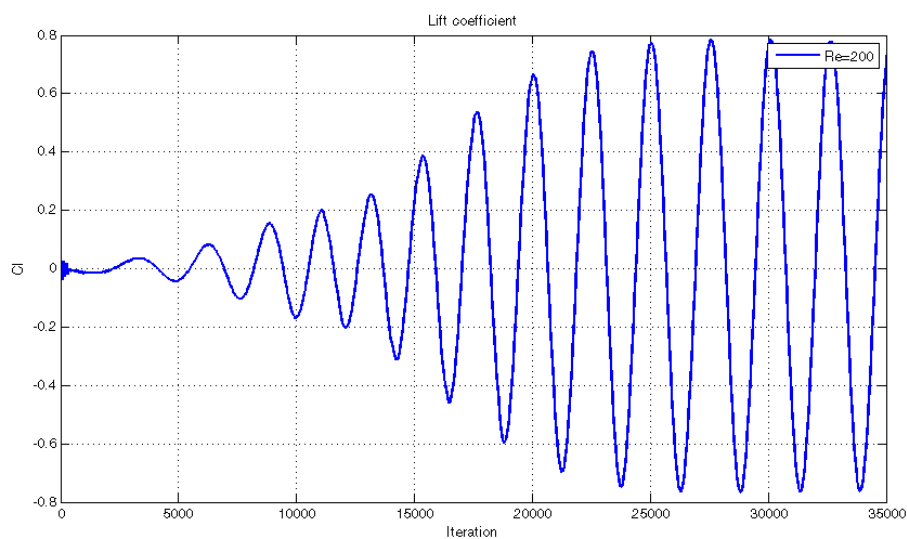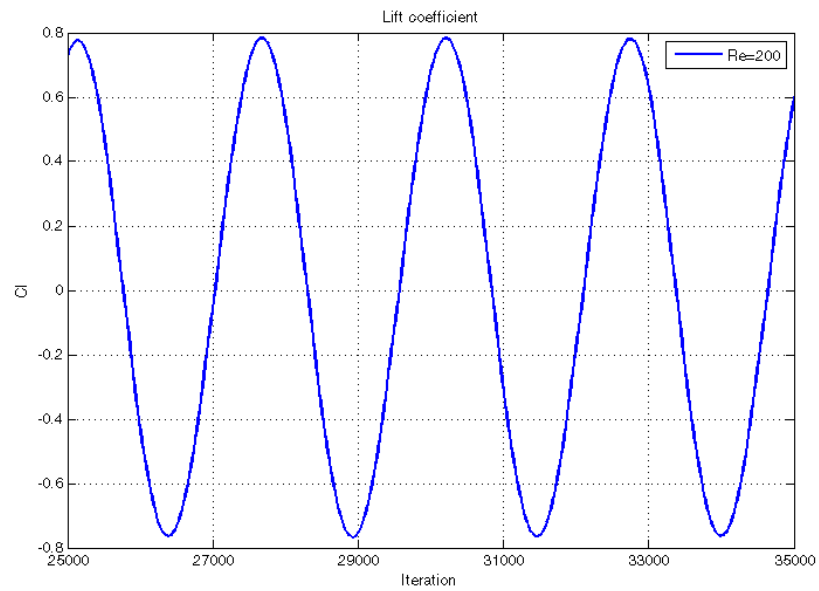

Figure 5.25. *Lift coefficient for square cylinder between 25000-35000 iteration for Re=200.*

Behind the obstacle, drag and lift coefficient data show periodic vortex shedding. Furthermore, the drag coefficient shows some small variations about the mean value, because of the unsteadiness of the flow. By increasing the Reynolds number, drag and lift coefficients and Strouhal number values increase. At prescribed Reynolds numbers, counter vortices are uniformly positioned downstream of the obstacles. The strength from these vortices decreases along the downstream from the obstacle due to dissipation.

Performing a frequency analysis of the time series data is necessary to identify the dominant frequency in the periodic flow in the wake. In the frequency spectrum, distinct dominating frequency shows the vortex shedding frequency. To get this frequency, FFT analysis is performed by again using FFT function in MATLAB as mentioned in Section 5.1.

The corresponding frequency spectra are shown in Figs. 5.26 and 5.27 for Re=100 and Re=200 respectively.

Figure 5.26. Frequency spectrum of the lift coefficient for flow past a square cylinder for Re=100

Figure 5.27. Frequency spectrum of the lift coefficient for flow past a circular cylinder for Re=200

Comparison of our results, that includes drag and lift coefficients and Strouhal numbers for both cases can be seen in Table 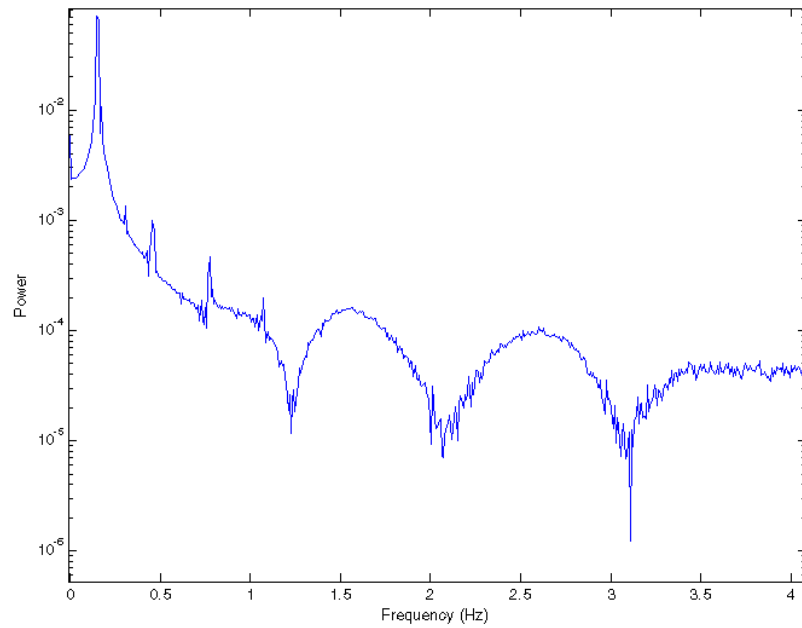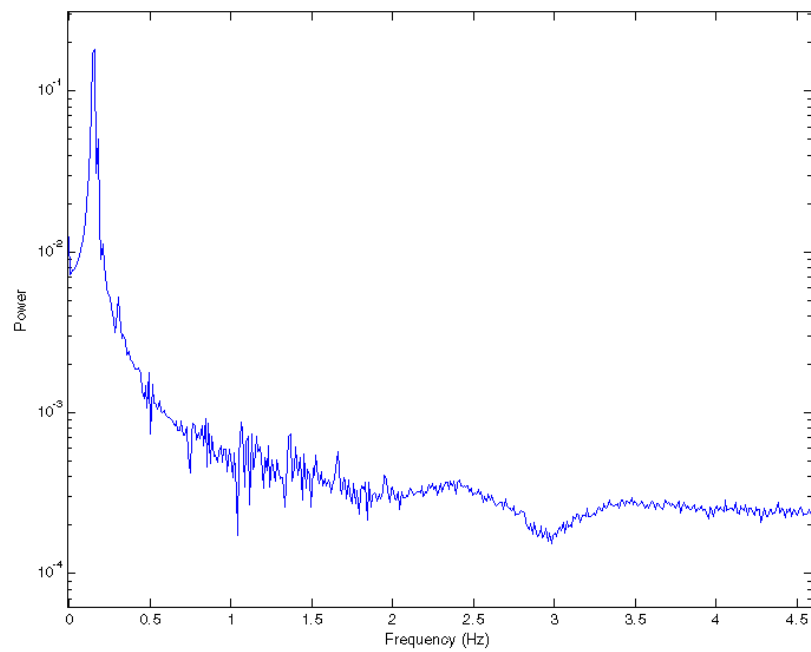5.2. In this table, mean and fluctuating components of these coefficients are shown in comparison to the previous studies at $Re = 100$ and $Re = 200$.

Table 5.2. *Flow parameters for flow field around single square cylinder at Re=100 and 200.*

Parameters	Drag Coefficients (C_D)		Lift coefficient (C_L)		Strouhal number (St)	
	Re=100	Re=200	Re=100	Re=200	Re=100	Re=200
Arnal et al. (1991)	1.41	1.52	-	-	0.152	0.156
Daviset. et. al. (1982)	1.64	1.72	-	-	-	-
Treidler (1991)	1.68	1.74	-	-	0.15	0.154
Sohankar et al. (1998)	1.76	1.78	-	-	0.142	0.156
Harichandan & Roy(2010)	1.72	1.86	-	-	0.152	0.158
Present study	1.62	1.76	0.008	0.039	0.150	0.158

In square cylinder case, our results of the flow parameters compare reasonably well with the other studies in literature as can be seen in Table 5.2.

5.3. Simulation of Flow Past an Array of Two Cylinders

Flow around arrays of circular cylinders has numerous applications in real life, such as landing gears of the aircrafts in flight and underwater pipes (Fernández, 2014). In addition to these examples, there are other applications of the flow around cylindrical structures, like, offshore risers, bridge piers, periscopes, chimneys, towers, antennae and wires (Norberg, 2003). Also rod structure of the nuclear reactors, heat exchangers for electronic components and heat exchangers which use pin fins for micro-devices are the other examples of cylinder arrays (Fornarelli et al., 2015). These examples make this subject very attractive for researchers to investigate.

For this case, a staggered arrangement of two cylinders each having a diameter D is employed in a channel as an extension of the case in Section 5.1. The domain is taken as 6D high and 15D long as before, and the two circular cylinders are placed at 4D and 11D distances away from the upstream and downstream boundaries relative to the midpoint between the two cylinders, repectively (see Fig. 5.29). We initialise the system by adjusting $f_a(\boldsymbol{x}, t = 0) = f_a^{eq}(\rho = 1, \boldsymbol{u} = 0)$. The maximum velocity of the inlet profile is set as $u_{max} = 0.1$ which is the maximum velocity per unit lattice for each time step. For this case time step value set at 0.04.

Starting with a steady Poiseuille flow in the channel, bounce-back BCs are applied at upper and lower no slip walls and curved boundary conditions applied on the cylinder surfaces as mentioned in Section 5.1.

A literature search for a reference study that carries the main features of our problem as closely as possible yielded a study conducted by Johnson et al. (1993) that studies the flow over two staggered cylinders as a representative unit domain of a periodic array of cylinders as shown in Fig. 5.28.
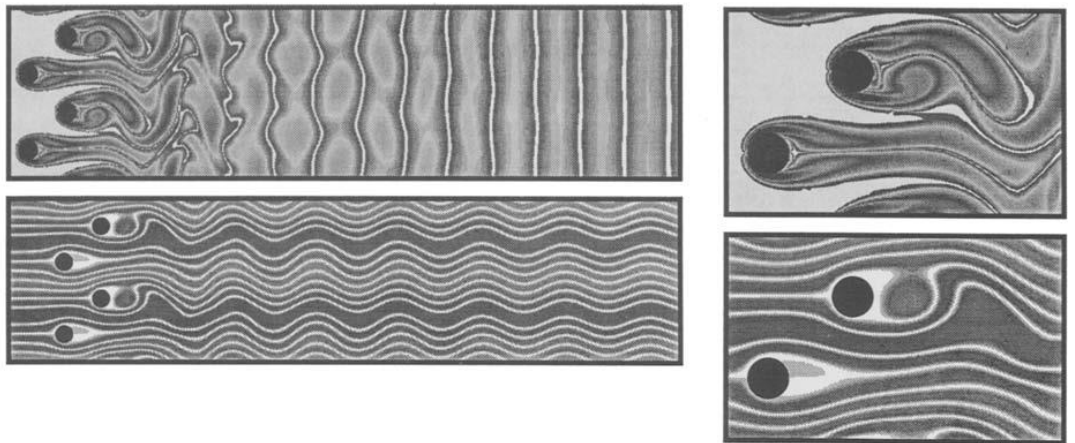
Figure 5.28. *Uniperiodic flow past two cylinders: vorticity and stream with FVM (Johnson et al., 1993)*

For the simulation at $Re = 100$, velocity contours are given for the two staggered cylinder arrangement in Fig. 5.29.
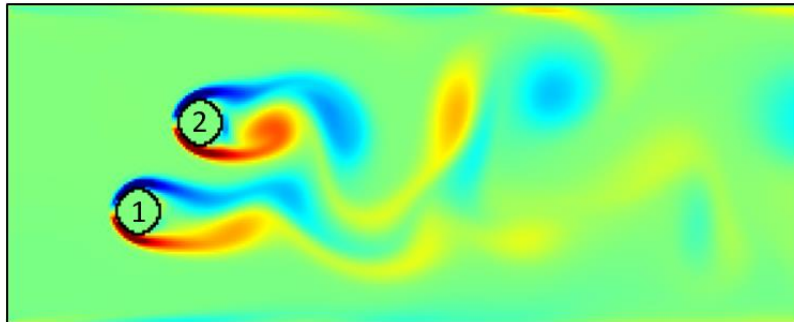
Figure 5.29. *Flow past two cylinders vorticity contours with LBM*

The drag and lift coefficients are shown developing in Figs. 5.30-5.33 for cylinder 1 and 2 as indicated.
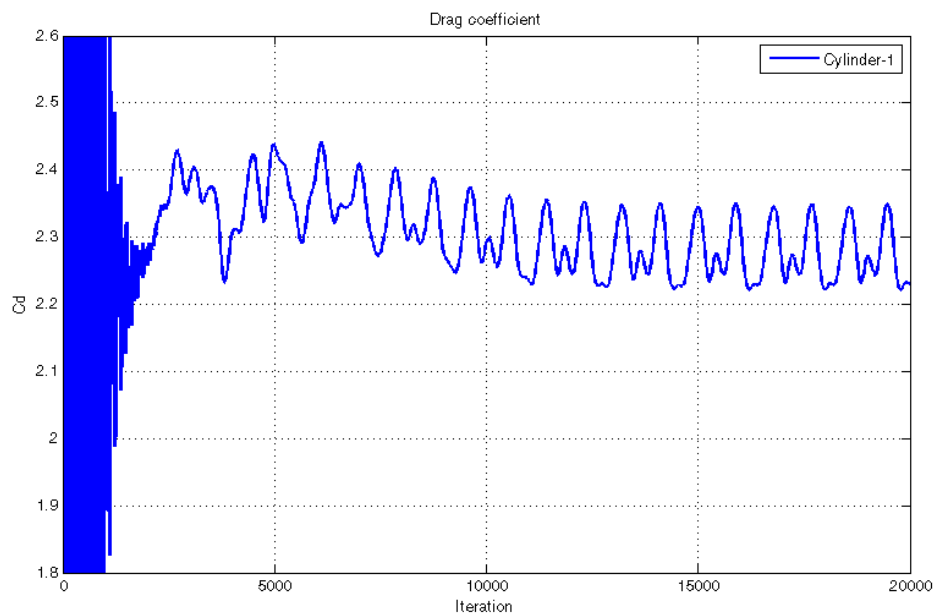
Figure 5.30. *Time history of drag coefficient for cylinder 1 for Re=100.*
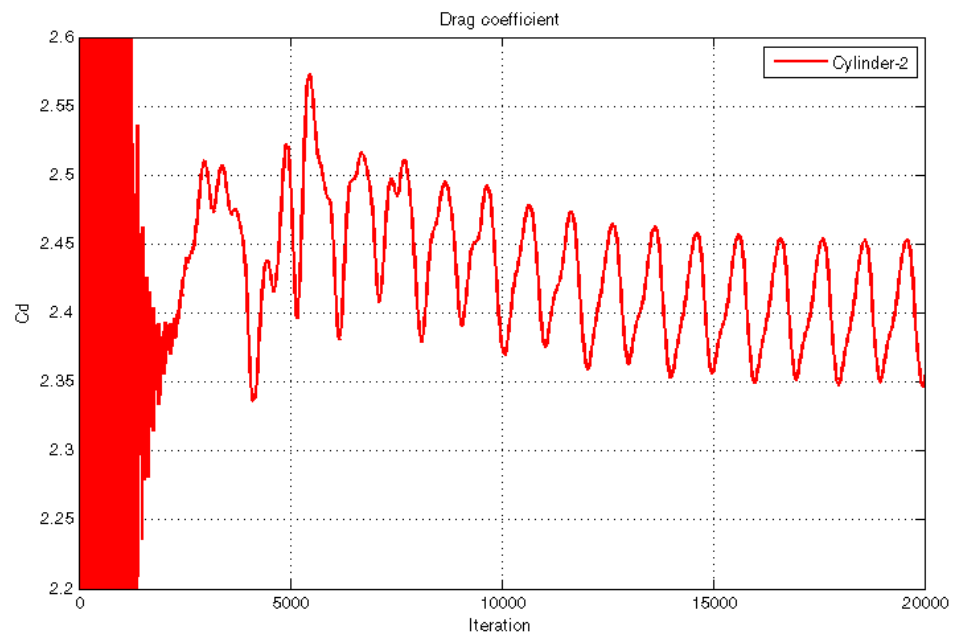
Figure 5.31. *Time history of drag coefficient for cylinder 2 for Re=100.*
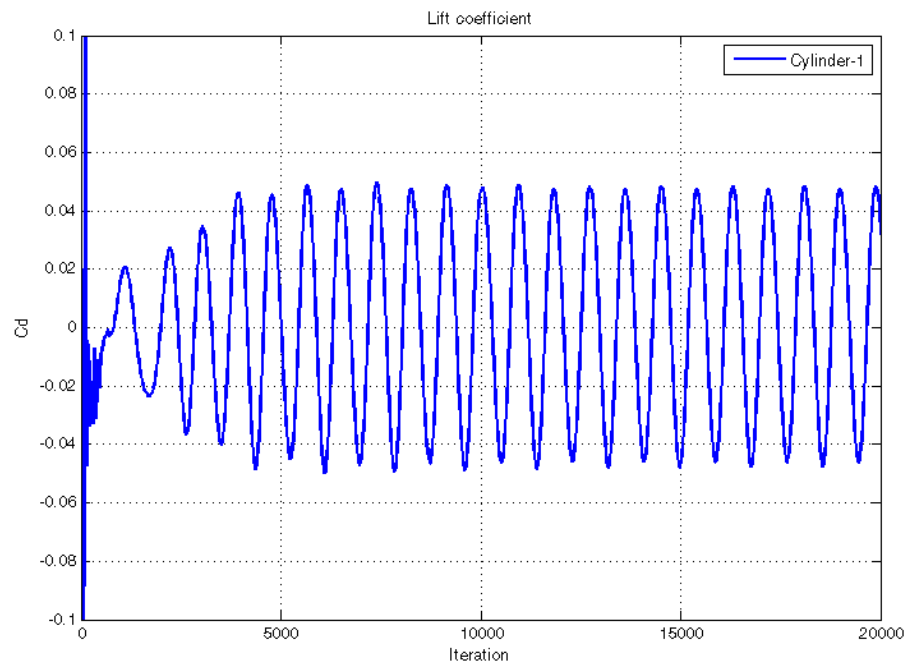
Figure 5.32. *Time history of lift coefficient for cylinder 1 for Re=100.*

83
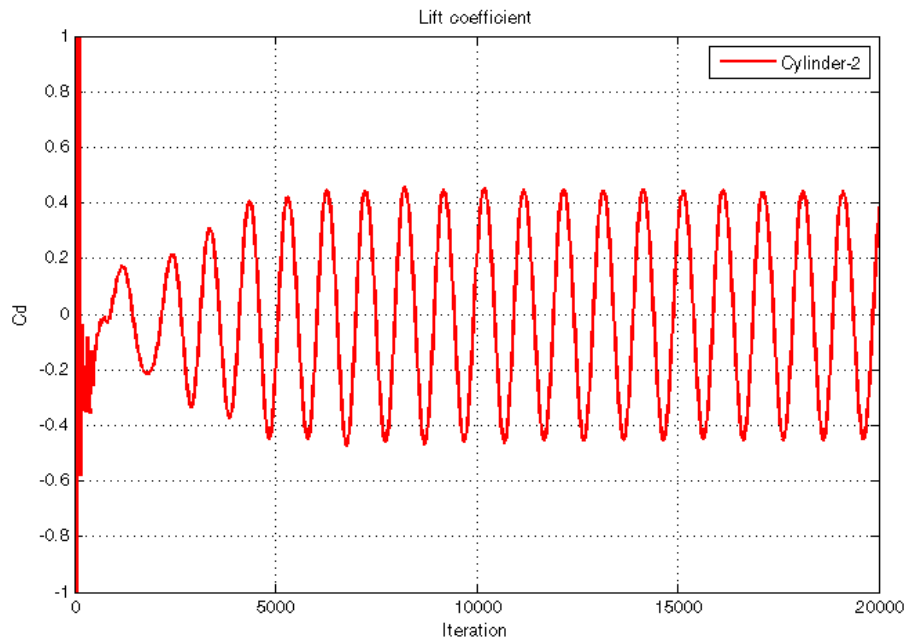
Figure 5.33. Time history of lift coefficient for cylinder 2 for Re=100.

After the flow gets developed, the evolution of the drag and lift coefficient values are shown in Figs. 5.34 and 5.37 for both cylinders as indicated.
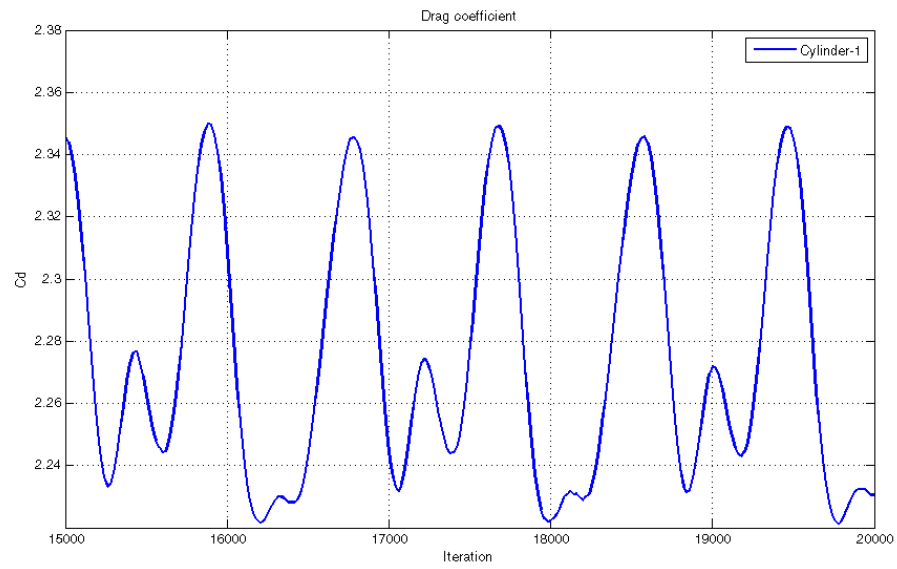
Figure 5.34. *Drag coefficient for cylinder 1 between 15000-20000 iteration for Re=100.*
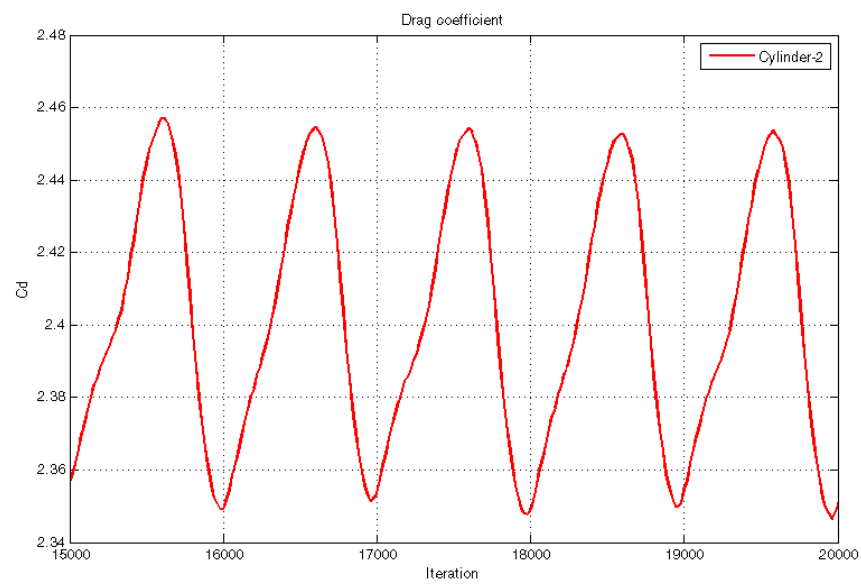
Figure 5.35. *Drag coefficient for cylinder 2 between 15000-20000 iteration for Re=100*

85
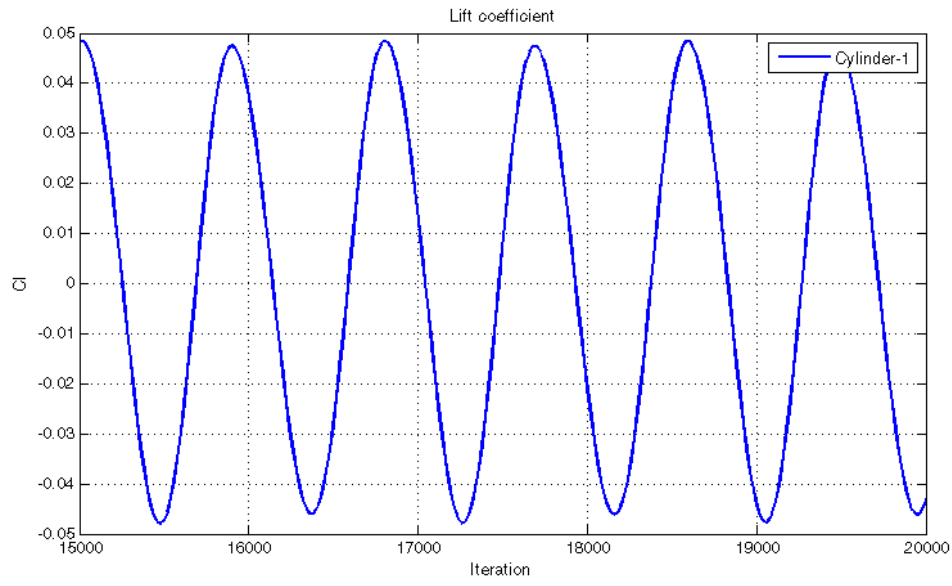
Figure 5.36. *Lift coefficient for cylinder 1 between 15000-20000 iteration for Re=100.*
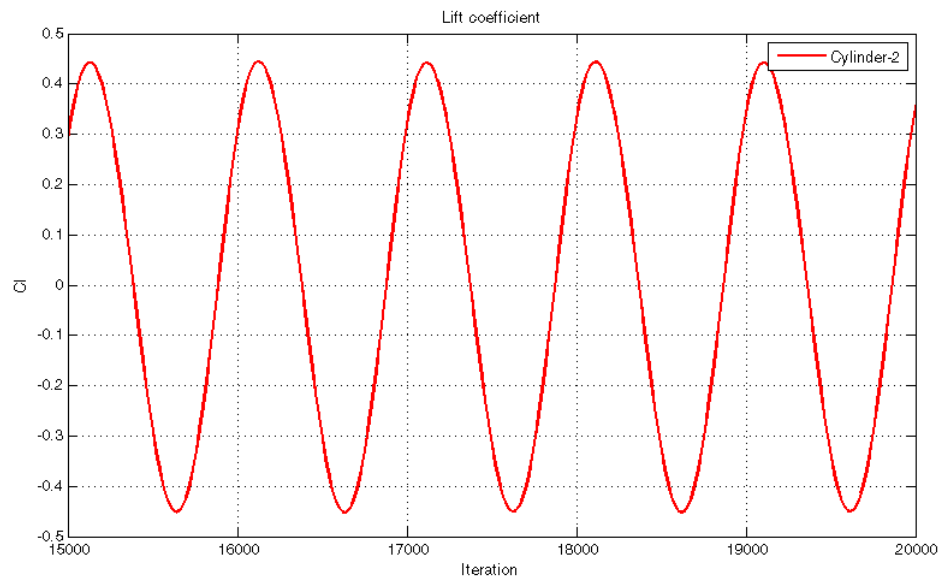
Figure 5.37. *Lift coefficient for cylinder 2 between 15000-20000 iteration for Re=100.*

As shown in Figs. 5.34 and 5.35, after the start of the vortex shedding, the mean value of the drag coefficient for cylinder 2 settles to be higher than that for cylinder 1. Plausibly, this is due to cylinder 2 being affected by the wake of the cylinder 1. Moreover, for the cylinder 2, which is placed downstream of cylinder 1, the lift coefficient exhibits relatively larger amplitude of fluctuations. This may be explained by the asymmetric pressure fluctuations in the wake of cylinder 1 affecting cylinder 2. The same trend is also observed in the numerical simulation conducted by Johnson et al. (1993).

The drag and lift coefficient data for this problem are given in Table 5.3 in comparison to those in Johnson et al. (1993) that the two cylinder configuration is placed in a uni-perodic domain representing a caharacteristic unit cell of an array of cylinders (see Fig. 5.28).

Table 5.3. *Flow past two cylinders comparison: drag and lift coefficients*

Parameters	Drag coefficient (C_D)		Lift coefficient (C_L)	
	Cylinder 1	Cylinder 2	Cylinder 1	Cylinder 2
Johnson et al. (1993)	2.28±0.001	2.56±0.057	±0.045	±0.749
Present study	2.27±0.05	2.40±0.055	±0.048	±0.45

The comparison shows some agreement between our study and that of Johnson et al. (1993). The discrepancy may be explained by the difference in the configuration of the computational domain. Johnson et al. (1993) have used periodic boundary conditions in the upper and lower boundaries of the computational domain where it is taken as a unit cell when stacked vertically represents an array of cylinders. In our study, the cylinders are placed in a channel bounded by the no-slip upper and lower walls as an extension of our numerical simulations in Sections 5.1 and 5.2. The slowing down effect of the wall boundaries are reflected by the data in Table 5.3 obtained by the present study.

CHAPTER 6

DISCUSSION

For those working with CFD who knows the difficulties associated with numerically attacking Navier-Stokes equations (Zeytounian, 2014), the simplicity of LBM both as a theoretical and a numerical tool in simulating hydrodynamics is surprising. Advection of a distribution function in mesoscopic scale governed by Boltzmann equation which is basically a simple hyperbolic partial differential equation is a relatively new paradigm in numerical modelling in the field of hydrodynamics that is classically dominated by macroscopic scale modelling. In comparison to the nonlinearity of the Navier-Stokes equations by the notorious advection term, the nonlinearity in LBM only appears in the collision term that is already greatly simplified by the introduction of the BGK collision operator replacing the classical highly complex nonlinear Boltzmann collision integral operator. The local implementation of LBM on a square lattice makes it simple to code and to parallelize, if needed, which is not pursued in this study.

Even though it is not in the scope of this thesis, the promising applicability of LBM to numerically model flows in porous media, multiphase and multicomponent flows may be included amongst the advantages. Actually, the promise of being able to simulate these types of flows that are very hard otherwise using Navier-Stokes equations, constitutes our original motivation to explore the basic numerical approaches to Boltzmann equation that is undertaken in this thesis. Other allures of LBM for us are the promising prospects of simulation inherently mesoscopic phenomena such as modelling rheology of ferrofluids, microfluidics, capillarity, condensation and evaporation to name a few (Huang et al., 2015; Satoh, 2017)

The objective of this study is the examination and the validation of the LBM method. Developed LBM code is applied to 2D flow models and tested on some configurations ranging from elementary to complex. First of all, for the Poiseuille flow, that is an attractive flow configuration because of having a closed form analytic representation, LBM simulation produced very accurate results in comparison to the analytic solutions obtained from the NS equations. Further, LBM simulations are performed for flow past a circular and square cylinders for different Reynolds numbers. The validation of these simulations are sought in terms of some characteristic flow parameters like drag and lift coefficients and Strouhal numbers. These parameters are found to be similar to relevant studies in literature. A further simulation is performed for a two circular cylinders configuration. In this case, the two cylinders are staggered and have equal radii. In this problem, we computed the flow parameters for both cylinders as before. Time evolution of the drag and lift coefficients as well as the means and fluctuations of their oscillatory behaviour due to the vortex shedding are computed. The comparison with a closest possible study found in literature (to the best of our efforts) showed some agreement. The observed discrepancy is expected based on the physics as a consequence of the differences in the configurations.

LBM is still developing in many aspects. As a user of the conventional CFD techniques, however, the somewhat vagueness in the implementation of the boundary conditions, the approach to incompressibility in the weak sense, having limitations on specifying viscosity, and other intensive properties have been disconcerting. A good perspective on LBM is given in Nourgaliev, et al. (2003).

This study has served as a helpful starting point for understanding and documenting fundamental ideas behind the numerical approaches to the Boltzmann equation regarding hydrodynamics. In order to focus on the fundamentals, however, the flow configurations are selected as basic 2D geometries ranging from channel flow to the fluid flow past different types of basic obstacles. The next step in mastering the computational tool of LBM should involve 3D flow configurations together with

parallelization efforts. The ultimate objective, in fact, should be to study flow configurations that are hard in the framework of conventional CFD techniques such as multiphase and multicomponent flows. In the light of this exploration, various new techniques, such as multi-relaxation-time (MRT) collision operators modifying BGK collision operator, entropic LBM with improved stability characteristics (Boghosian, 2001), will be further pursued.

REFERENCES

Alim, U. R., Entezari, A., & Mller, T. (2009). The lattice-boltzmann method on optimal sampling lattices. *IEEE Transactions on Visualization and Computer Graphics*, *15*(4), 630–641. http://doi.org/10.1109/TVCG.2008.201

Amati, G., Succi, S., & Benzi, R. (1997). Turbulent channel flow simulations using a coars-grained extension of the lattice Boltzmann method. *Fluid Dynamics Research*, *19*(5), 289–302.

Arnal, M., J. Goering, D., & A. C. Humphrey, J. (1991). *Vortex Shedding From a Bluff Body Adjacent to a Plane Sliding Wall*. *Journal of Fluids Engineering-transactions of The Asme - J FLUID ENG* (Vol. 113). https://doi.org/10.1115/1.2909508

Bao, Y., & Meskas, J. (2011). Lattice Boltzmann Method for Fluid Simulations. *Cfd*, (2), 1–16. Retrieved from http://www.math.nyu.edu/~billbao/report930.pdf

Bhatnagar, P. L., Gross, E. P., & Krook, M. (1954). A model for collision processes in gases. I. Small amplitude processes in charged and neutral one-component systems. *Physical Review*, *94*(3), 511–525. https://doi.org/10.1103/PhysRev.94.511

Boix, C. (2013). Application of the Lattice Boltzmann Method to Issues of Coolant Flows in Nuclear Power Reactors, 132.

Boyd, J. P. (2000). Chebyshev and Fourier Spectral Methods. *New York*, *7*, 688. http://doi.org/10.1007/978-0-387-77674-3

Braza, M., Chassaing, P., & Minh, H. H. (1986). Numerical study and physical analysis of the pressure and velocity fields in the near wake of a circular cylinder. *Journal of Fluid Mechanics*, *165*, 79–130. https://doi.org/DOI: 10.1017/S0022112086003014

Breuer, M., Bernsdorf, J., Zeiser, T., & Durst, F. (2000). Accurate computations of the laminar flow past a square cylinder bases on two different methods: Lattice-{B}oltzmann and Finitie-Volume. *Int. J. Heat and Fluid Flow*, *21(2)*, 186–196.

Canuto, D., & Taira, K. (2017). Two-dimensional compressible viscous flow around a circular cylinder, (1956). https://doi.org/10.1017/jfm.2015.635

Cao, N., Chen, S., Jin, S., & Martínez, D. (1997). Physical symmetry and lattice symmetry in the lattice Boltzmann method. *Physical Review E - Statistical Physics, Plasmas, Fluids, and Related Interdisciplinary Topics*, *55*(1), R21–R24. https://doi.org/10.1103/PhysRevE.55.R21

Chapman, S., Cowling, T. G. (1970). The Mathematical Theory of Non-Uniform Gases. Cambridge University Press

Chen, H., Chen, S., & Matthaeus, W. H. (1992). Recovery of the Navier-Stokes equations using a lattice-gas Boltzmann method. *Physical Review A*. https://doi.org/10.1103/PhysRevA.45.R5339

Chen, L., Kang, Q., Mu, Y., He, Y. L., & Tao, W. Q. (2014). A critical review of the pseudopotential multiphase lattice Boltzmann model: Methods and applications. *International Journal of Heat and Mass Transfer*, *76*, 210–236. https://doi.org/10.1016/j.ijheatmasstransfer.2014.04.032

Chen, N. X., & Sun, B. H. (2017). Note on Divergence of the Chapman-Enskog Expansion for Solving Boltzmann Equation∗. *Chinese Physics Letters*, *34*(2), 1–3. https://doi.org/10.1088/0256-307X/34/2/020502

Chen, S., & Doolen, G. D. (1998). Lattice Boltzmann method for fluid flows. *Annual Review of Fluid Mechanics*, *30*(1), 329–364. Retrieved from http://www.annualreviews.org/doi/abs/10.1146/annurev.fluid.30.1.329

Cushman-Roisin, B., & Epps, B. P. (2018). From Boltzmann Kinetics to the Navier-Stokes Equations, 1–14.

Ding, H., Shu, C., Yeo, K. S., & Xu, D. (2007). Numerical simulation of flows around two circular cylinders by mesh-free least square-based finite difference methods. *International Journal for Numerical Methods in Fluids*, *53*(2), 305–332. https://doi.org/10.1002/fld.1281

Fahner, G. (1991). A Multispeed Model for Lattice-Gas Hydrodynamics v v, 5, 1–14.

Fernández, L. (2014). Direct numerical simulation of the flow around an array of cylinders.

Fornarelli, F., Oresta, P., & Lippolis, A. (2015). Flow patterns and heat transfer around six in-line circular cylinders at low reynolds number. *JP Journal of Heat and Mass Transfer*, *11*(1), 1–24. https://doi.org/10.17654/JP2015_001_028

Frisch, U., Hasslacher, B., & Pomeau, Y. (1986). Lattice-gas automata for the Navier-Stokes equation. *Physical Review Letters*. https://doi.org/10.1103/PhysRevLett.56.1505

Gallivan, M. a, Noble, D. R., Georgiadis, J. G., & Buckius, R. O. (1997). An evaluation of the bounce-back boundary condition for lattice Boltzmann simulations. *International Journal for Numerical Methods in Fluids*, *25*(3), 249–263. https://doi.org/10.1002/(SICI)1097-0363(19970815)25:3<249::AID-FLD546>3.3.CO;2-Z

Gergova, M. (2002). Evaluation of Improved Boundary Conditions for the Lattice Boltzmann Approach: Investigation of the Laminar Vortex Street behind a Circular Cylinder, (December), 54.

Grad, H. (1949a). Note on N- dimensional hermite polynomials. *Communications on Pure and Applied Mathematics*, *2*(4), 325–330. https://doi.org/10.1002/cpa.3160020402

Grad, H. (1949b). On the kinetic theory of rarefied gases. *Communications on Pure and Applied Mathematics*, *2*(4), 331–407. https://doi.org/10.1002/cpa.3160020403

Harichandan, A. B., & Roy, A. (2010). Numerical investigation of low Reynolds number flow past two and three circular cylinders using unstructured grid CFR scheme. *International Journal of Heat and Fluid Flow*, *31*(2), 154–171. https://doi.org/10.1016/j.ijheatfluidflow.2010.01.007

He, X., & Doolen, G. (1997). Lattice Boltzmann Method on Curvilinear Coordinates System: Flow around a Circular Cylinder. *Journal of Computational Physics*, *134*(2), 306–315. https://doi.org/10.1006/jcph.1997.5709

He, X., Luo, L.-S., & Micah Dembo. (1996). Some Progress in Lattice Boltzmann Method. Part I. Nonuniform Mesh Grids. *Journal of Computational Physics*, *129*, 357–363.

Henderson, R. D. (1995). Details of the drag curve near the onset of vortex shedding. *Physics of Fluids*, *7*(9), 2102–2104. https://doi.org/10.1063/1.868459

Higuera, F. J., & Jimenez, J. (1989). Boltzmann approach to lattice gas simulations. *Epl*, *9*(7), 663–668. https://doi.org/10.1209/0295-5075/9/7/009

Hirsch, C. (2007). *Numerical Computation of Internal & External Flows: Volume 1 (Fundamentals of Computational Fluid Dynamics)*. https://doi.org/10.1007/978-3-540-85056-4

Ho, C.-F., Chang, C., Lin, K.-H., & Lin, C.-A. (2009). Consistent Boundary Conditions for 2D and 3D Lattice Boltzmann Simulations. *Cmes-Computer Modeling In Engineering Camp; Sciences*, *44*(2), 137–155. https://doi.org/10.3970/cmes.2009.044.137

Huang, H., & Sukop, M. (2015). *Multiphase lattice Boltzmann Methods* (Vol. 53). https://doi.org/10.1017/CBO9781107415324.004

Johnson, A. A., Tezduyar, T. E., & Liou, J. (1993). Numerical simulation of flows past periodic arrays of cylinders. *Numerical Simulation of Flows Past Periodic Arrays of Cylinders*, *11*, 371–383. https://doi.org/https://doi.org/10.1007/BF00350094

Józsa, T. I., Szőke M., Teschner, T., Könöszy L., Moulitsas I., (2016). Validation and Verification of a 2D Lattice Boltzmann Solver for Incompressible Fluis Flow, *ECCOMAS Congress.*

Kadanoff, L. (1986). On Two Levels. *Physics Today*.

Koda, Y. (2013). Lattice Boltzmann Method for Simulating Turbulent Flows.

Krüger, T., Kusumaatmaja, H., Kuzmin, A., Shardt, O., Silva, G., & Viggen, E. M. (2016). *The Lattice Boltzmann Method - Principles and Practice*. https://doi.org/10.1007/978-3-319-44649-3

Latt, J., Chopard, B., Malaspinas, O., Deville, M., & Michler, A. (2008). Velocity boundaries in the lattice Boltzmann method. *Physical Review. E, Statistical, Nonlinear, and Soft Matter Physics*, *77*(5 Pt 2), 056703. https://doi.org/10.1103/PhysRevE.77.056703

Li, Y., Leboeuf, E. J., & Basu, P. K. (2005). Least-squares finite-element scheme for the lattice Boltzmann method on an unstructured mesh. *Physical Review E - Statistical, Nonlinear, and Soft Matter Physics*, *72*(4). https://doi.org/10.1103/PhysRevE.72.046711

Lim, H. A. (1990). Lattice-gas automaton simulations of simple fluid dynamical problems. *Mathematical and Computer Modelling*, *14*(C), 720–727. https://doi.org/10.1016/0895-7177(90)90276-S

M. Gresho, P., L. Lee, R., & Sani, R. (1978). *On the time-dependent FEM solution of the incompressible Navier-Stokes equations in two- and three-dimensions. Recent Advances in Numerical Methods in Fluids*.

McNamara, G. R., & Zanetti, G. (1988). Use of the boltzmann equation to simulate lattice-gas automata. *Physical Review Letters*, *61*(20), 2332–2335. https://doi.org/10.1103/PhysRevLett.61.2332

Mei, R., & Shyy, W. (1998). On the Finite Difference-Based Lattice Boltzmann Method in Curvilinear Coordinates. *Journal of Computational Physics*, *143*(2), 426–448. https://doi.org/10.1006/jcph.1998.5984

Mele, I. (2013). Lattice Boltzmann method. *University of Ljubljana*, (March). https://doi.org/10.1146/annurev-fluid-011212-140634

Meneghini, J. R., Saltara, F., Siqueria, C. L. R., & Ferrari Jr, J. A. (2001). NUMERICAL SIMULATION OF FLOW INTERFERENCE BETWEEN TWO CIRCULAR CYLINDERS IN TANDEM AND SIDE-BY-SIDE ARRANGEMENTS. *Journal of Fluids and Structures*, *15*(2), 327–350. https://doi.org/https://doi.org/10.1006/jfls.2000.0343Get

Mohamad, A. A. (2011). Lattice Boltzmann Method-Fundamentals and Engineering Applications with Computer Codes. https://doi.org/10.1007/978-0-85729-455-5

Nie, X. B., Chen, S. Y., E, W. N., & Robbins, M. O. (2004). A continuum and molecular dynamics hybrid method for micro- and nano-fluid flow. *Journal of Fluid Mechanics*, *500*(2004), 55–64. https://doi.org/10.1017/S0022112003007225

Norberg, C. (1987). Effects of Reynolds number and a low-intensity freestream turbulence on the flow around a circular cylinder. *Thesis*, (May 1987). Retrieved from http://www.ht.energy.lth.se/fileadmin/ht/Publikation-87-2.pdf

Norberg, C. (2003). Fluctuating lift on a circular cylinder: Review and new measurements. *Journal of Fluids and Structures*, *17*(1), 57–96. https://doi.org/10.1016/S0889-9746(02)00099-3

Nourgaliev, R. R., Dinh, T. N., Theofanous, T. G., & Joseph, D. D. (2003). The lattice boltzmann equation method: theoretical interpretation, numerics and implications. *Int. J. Multiphase Flow*, *29*, 117–169.

Pontrelli, G., Halliday, I., & Melchionna, S. (2007). The Lattice Boltzmann Method and Multiscale Hemodynamics : Recent Advances and Perspectives, (January). https://doi.org/10.11128/sne.23.on.10181

Portinari, M. (2015). 2D and 3D VERIFICATION AND VALIDATION OF THE LATTICE BOLTZMANN METHOD.

Qian, Y. H., D'Humèries, D., & Lallemand, P. (1992). Lattice BGK Models for Navier - Stokes equation. *Europhysics Letters*, *17*(6), 479–484. https://doi.org/10.1209/0295-5075/17/6/001

Roache, P. J. (1998). Verification and Validation in COmputational Science and Engineering. *Hermosa publishers, New Mexico.*

Roshko, A. (1954). On The Development of Turbulent Wakes From Vortex Streets. *National Advisory Comittee for Aeronautics*.

Satoh, A. (2011). *Introduction to Practice of Molecular Simulation Molecular Dynamics, Monte Carlo, Brownian Dynamics, Lattice Boltzmann, Dissipative Particle Dynamics*.

Satoh, A. (2017). Modeling of Magnetic Particle Suspensions for Simulations, 368. https://doi.org/https://doi.org/10.1201/9781315166094

Sen, S., Mittal, S., & Biswas, G. (2009). Steady separated flow past a circular cylinder at low Reynolds numbers. *Journal of Fluid Mechanics*, *620*, 89–119. https://doi.org/10.1017/S0022112008004904

Shan, X., & He, X. (1998). Discretization of the velocity space in the solution of the boltzmann equation. *Physical Review Letters*, *80*(1), 65–68. http://doi.org/10.1103/PhysRevLett.80.65

Shan, X., Yuan, X. F., & Chen, H. (2006). Kinetic theory representation of hydrodynamics: A way beyond the Navier-Stokes equation. *Journal of Fluid Mechanics*, *550*, 413–441. https://doi.org/10.1017/S0022112005008153

Sohankar, A., Norberg, C., & Davidson, L. (1998). Low-Reynolds-number flow around a square cylinder at incidence: Study of blockage, onset of vortex shedding and outlet boundary condition. *Doktorsavhandlingar Vid Chalmers*

Tekniska Hogskola, *26*(1371), 39–56. https://doi.org/10.1002/(SICI)1097-0363(19980115)26:1

Succi, S. (2001). The Lattice Boltzmann Equation for Fluid Dynamics and Beyond, Oxford Science Publications.

Sukop, M. C., & Thorne, D. T. (2006). *Lattice Boltzmann Modeling. Physical Review E - Statistical, Nonlinear and Soft Matter Physics* (Vol. 79). https://doi.org/10.1007/978-3-540-27982-2

Tahir Saeed Khan. (2011). *Stabilizing Lattice Boltzmann Simulation of Floes Past Bluff Bodies by Intoductions of Ehrenfests' Limiters*.

Tölke, J., Krafczyk, M., Schulz, M., & Rank, E. (2000). Discretization of the Boltzmann equation in velocity space using a Galerkin approach. *Computer Physics Communications*, *129*(1), 91–99. https://doi.org/10.1016/S0010-4655(00)00096-5

Treidler, E. B. (1991). *An Experimental and Numerical Investigation of Flow Past Ribs in a Channel*.

Tritton, D. J. (1959). Experiments on the flow past a circular cylinder at low Reynolds numbers. *Journal of Fluid Mechanics*, *6*, 547–567. https://doi.org/10.1017/S0022112059000829

von Kármán, T. (1911). Kármán, Th. von. *Nachrichten von Der Gesellschaft Der Wissenschaften Zu Göttingen, Mathematisch-Physikalische Klasse*, *1911*, 509–517. Retrieved from http://resolver.sub.uni-goettingen.de/purl?PPN252457811_1911/dmdlog57

von Neumann, J. (1966). Theory of self-reproducing automata. *Theory of Self-Reproducing Automata*. https://doi.org/10.1016/0020-0271(69)90026-6

W. Davis, R., & F. Moore, E. (1982). *A numerical Study of vortex shedding from rectangles*. *Journal of Fluid Mechanics* (Vol. 116). https://doi.org/10.1017/S0022112082000561

Weimar, J. R., & Boon, J.-P. (1993). A New Class of Cellular Automata for Reaction-Diffusion Systems. *Physical Review E*, *49*(2), 4. https://doi.org/10.1103/PhysRevE.49.1749

Wiesenberger, C. (1923). Neuere Feststellungen Uber die Gesetze des Flussigkeits. und Luftwiderstands. *Physikalische Zeitschrift*, *22*, 321–328. Retrieved from https://ci.nii.ac.jp/naid/10013462567/en/

Wolf-Gladrow, D. a. (2000). Lattice-Gas Cellular Automata and Lattice Boltzmann Models - An Introduction. *PoLAR*, 308. https://doi.org/978-3-540-66973-9

Wolfram, S. (1986). Cellular automaton fluids 1: Basic theory. *Journal of Statistical Physics*, *45*(3–4), 471–526. https://doi.org/10.1007/BF01021083

Xi, H., Peng, G., & Chou, S. H. (1999). Finite-volume lattice Boltzmann method. *Physical Review E - Statistical Physics, Plasmas, Fluids, and Related Interdisciplinary Topics*, *59*(5), 6202–6205. https://doi.org/10.1103/PhysRevE.59.6202

Xia, B., & Sun, D. W. (2002). Applications of computational fluid dynamics (CFD) in the food industry: A review. *Computers and Electronics in Agriculture*, *34*(1–3), 5–24. https://doi.org/10.1016/S0168-1699(01)00177-6

Yepez, J. (1993). AFOSR Initiative Element : Lattice-Gas Automata and Lattice Boltzmann Methods as a Novel Parallel Computing Strategy. *Simulation*.

Zeytounian, R. K. (2014). *Five Decades of Tackling Models for Stiff Fluid Dynamics Problems. Five Decades of Tackling Models for Stiff Fluid Dynamics Problems*. https://doi.org/10.1007/978-3-642-39541-3

Zhang, J. (2011). Lattice Boltzmann method for microfluidics: Models and applications. *Microfluidics and Nanofluidics*, *10*(1), 1–28. https://doi.org/10.1007/s10404-010-0624-1

Zou, Q., & He, X. (1997). On pressure and velocity boundary conditions for the lattice Boltzmann BGK model. *Physics of Fluids*, *9*(6), 1591–1598.

APPENDICES

A. Hermite Polynomial and Gauss-Hermite Qudrature

<u>One-Dimensional Case</u>:

Hermite polynomial of degree n can be generated by the Rodrigues' formula

$$H^{(n)}(x) = \frac{(-1)^n}{\omega(x)} \frac{d^n}{dx^n} \omega(x) \tag{A1}$$

for integer $n \geq 0$ where $\omega(x)$ is the weight function

$$\omega(x) = \frac{1}{\sqrt{2\pi}} \exp(-x^2/2). \tag{A2}$$

Some Hermite polynomials are listed below:

$$H^{(0)}(x) = 1, \ \ H^{(1)}(x) = x, \ \ H^{(2)}(x) = x^2 - 1, \ \ H^{(3)}(x) = x^3 - 3x. \tag{A3}$$

They are orthogonal with respect to $\omega(x)$:

$$\int_{-\infty}^{\infty} \omega(x) H^{(n)}(x) H^{(m)}(x) dx = n! \, \delta_{nm}^2 \tag{A4}$$

where δ_{nm}^2 is the usual Kronecker delta. They form a complete basis so that any sufficiently well-behaved continuous function $f(x)$ can be represented as a series of Hermite polynomials

$$f(x) = \omega(x) \sum_{n=0}^{\infty} \frac{1}{n!} a^{(n)} H^{(n)}(x), \qquad a^{(n)} = \int_{-\infty}^{\infty} f(x) H^{(n)}(x) dx. \tag{A5}$$

Gauss-Hermite quadrature allows accurate numerical integration of a function $f(x)$ multiplied by the weight function $\omega(x)$ by a finite series of the function values $f(x_i)$ at certain points x_i, called abscissae (node):

$$\int_{-\infty}^{\infty} \omega(x)f(x)dx \approx \sum_{i=1}^{q} w_i f(x_i) \tag{A6}$$

where x_i are q roots of the Hermite polynomial of order q, $H^{(q)}(x_i) = 0$ and the quadrature weights w_i can be computed by

$$w_i = \frac{q!}{\left(qH^{(q-1)}(x_i)\right)^2}. \tag{A7}$$

It is guaranteed that for $f(x)$ a polynomial of degree $N \leq 2q - 1$, the quadrature integral (A1) is exact. Here is a summary of some Gauss-Hermite quadrature nodes and weights:

Table A.1. *Gauss-Hermite quadrature nodes and weights*

q	$N \leq 2q - 1$	Nodes, x_i	Weights, w_i
1	1	0	1
2	3	± 1	1/2
3	5	0	2/3
		$\pm\sqrt{3}$	1/6

<u>d-Dimensional Case</u>:

Hermite polynomials can constructed in d spatial dimensional space as follows

$$\boldsymbol{H}^{(n)}(\boldsymbol{x}) = \frac{(-1)^n}{\omega(\boldsymbol{x})} \boldsymbol{\nabla}^{(n)} \omega(\boldsymbol{x}), \qquad \omega(\boldsymbol{x}) = \frac{1}{(2\pi)^{d/2}} \exp(-\boldsymbol{x} \cdot \boldsymbol{x}/2) \quad \text{(A8)}$$

where $\boldsymbol{H}^{(n)}$ and $\boldsymbol{\nabla}^{(n)}$ are tensors of rank n having d^n components $H^{(n)}_{\alpha_1\alpha_2\ldots\alpha_n}$ and

$$\nabla^{(n)}_{\alpha_1\alpha_2\ldots\alpha_n} = \frac{\partial}{\partial x_{\alpha_1}} \frac{\partial}{\partial x_{\alpha_2}} \cdots \frac{\partial}{\partial x_{\alpha_n}}. \qquad \text{(A9)}$$

Here, $\{\alpha_1, \alpha_2 \ldots \alpha_n\}$ are n indices with each index ranging from 1 to d, such as, $\alpha_i \in \{x, y\}$ or $\{x, y, z\}$ in 2D ($d = 2$) or 3D ($d = 3$), respectively. In 2D, for example

$$\nabla^{(2)}_{xx} = \frac{\partial}{\partial x} \frac{\partial}{\partial x}, \qquad \nabla^{(2)}_{xy} = \nabla^{(2)}_{yx} = \frac{\partial}{\partial x} \frac{\partial}{\partial y}, \qquad \nabla^{(2)}_{yy} = \frac{\partial}{\partial y} \frac{\partial}{\partial y}. \qquad \text{(A10)}$$

resulting in the Hermite polynomials

$$H^{(0)}(\boldsymbol{x}) = 1, \qquad \text{(A11)}$$

$$H^{(1)}_x(\boldsymbol{x}) = -\frac{1}{\exp(-(x^2 + y^2)/2)} \frac{\partial}{\partial x} e^{-(x^2+y^2)/2} = x, \qquad \text{(A12)}$$

$$H^{(1)}_y(\boldsymbol{x}) = -\frac{1}{\exp(-(x^2 + y^2)/2)} \frac{\partial}{\partial y} e^{-(x^2+y^2)/2} = y, \qquad \text{(A13)}$$

$$H^{(2)}_{xx}(\boldsymbol{x}) = -\frac{1}{\exp(-(x^2 + y^2)/2)} \frac{\partial}{\partial x} \frac{\partial}{\partial x} e^{-(x^2+y^2)/2} = x^2 - 1, \qquad \text{(A14)}$$

$$H^{(2)}_{xy}(\boldsymbol{x}) = H^{(2)}_{yx}(\boldsymbol{x}) = -\frac{1}{\exp(-(x^2 + y^2)/2)} \frac{\partial}{\partial x} \frac{\partial}{\partial y} e^{-(x^2+y^2)/2} = xy, \quad \text{(A15)}$$

$$H^{(2)}_{yy}(\boldsymbol{x}) = -\frac{1}{\exp(-(x^2 + y^2)/2)} \frac{\partial}{\partial y} \frac{\partial}{\partial y} e^{-(x^2+y^2)/2} = y^2 - 1, \qquad \text{(A16)}$$

or in a more compact form (Grad, 1949a)

$$H^{(0)}(\boldsymbol{x}) = 1, \qquad \text{(A17)}$$

$$H^{(1)}_{\alpha_1}(\boldsymbol{x}) = x_{\alpha_1}, \qquad \text{(A18)}$$

$$H^{(2)}_{\alpha_1\alpha_2}(\boldsymbol{x}) = x_{\alpha_1} x_{\alpha_2} - \delta^2_{\alpha_1\alpha_2}, \qquad \text{(A19)}$$

$$H^{(3)}_{\alpha_1\alpha_2\alpha_3}(x) = x_{\alpha_1}x_{\alpha_2}x_{\alpha_3} - x_{\alpha_1}\delta^2_{\alpha_2\alpha_3} - x_{\alpha_2}\delta^2_{\alpha_1\alpha_3} - x_{\alpha_3}\delta^2_{\alpha_1\alpha_3}. \quad \text{(A20)}$$

The number of basis elements in each set $\{H^{(n)}(x)\}$ in d dimensions is

$$\binom{d+n-1}{n} = \frac{(d+n-1)!}{(d-1)!\,n!}. \quad \text{(A21)}$$

The orthogonality can also be generalized to d dimensions:

$$\int_{-\infty}^{\infty} \omega(x)H^{(n)}_{\alpha}(x)H^{(n)}_{\beta}(x)dx = \prod_{i=1}^{d} n_i!\,\delta^2_{nm}\delta^{(n+m)}_{\alpha\beta} \quad \text{(A22)}$$

where $\delta^{(n+m)}_{\alpha\beta}$ is a generalized Kronecker symbol which is 1 only if $\boldsymbol{\alpha} = (\alpha_1, \alpha_2 \dots \alpha_n)$ is a permutation of $\boldsymbol{\beta} = (\beta_1, \beta_2 \dots \beta_n)$ and 0 otherwise. In 3D, for example, (x, y, x, z) is a permutation of (y, x, x, z), but not of (x, y, z, y). n_x, n_y and n_z are the number of occurences in x, y and z in $\boldsymbol{\alpha}$. In (x, y, x, z), for example, $n_x = 2$ and $n_y = n_z = 1$.

Hermite polynomial representation of a function $f(x)$ in d dimensions is:

$$f(x) = \omega(x)\sum_{n=0}^{\infty}\frac{1}{n!}\boldsymbol{a}^{(n)}\cdot\boldsymbol{H}^{(n)}(x), \qquad \boldsymbol{a}^{(n)} = \int_{-\infty}^{\infty} f(x)\boldsymbol{H}^{(n)}(x)dx. \quad \text{(A23)}$$

The expansion coefficients $\boldsymbol{a}^{(n)}$ are also tensors of rank n, and the dot product $\boldsymbol{a}^{(n)} \cdot \boldsymbol{H}^{(n)}$ is representing full contraction $a^{(n)}_{\alpha_1\alpha_2\dots\alpha_n}H^{(n)}_{\alpha_1\alpha_2\dots\alpha_n}$, i.e. summation over all possible indices. The number of basis elements in a given set of N Hermite polynomial basis set, $\{\boldsymbol{H}^{(n)}(x)\}_{n=0}^{N}$ in d dimensions is

$$\binom{d+N}{N} = \frac{(d+N)!}{d!\,N!}. \quad \text{(A24)}$$

In multi-dimensions, no Gauss quadrature theory is known, however, a production formulae can be constructed from 1D case. A polynomial $p(x)$ of degree n in d-dimensions can be written as:

$$p(\pmb{x}) = \sum_{n_1+\ldots+n_d \le n} c_{n_1 n_2 \ldots n_d} \prod_{i=1}^{d} x_i^{n_i}. \tag{A25}$$

The weighted integral of each individual term of $p(\pmb{x})$ can be performed separately and for each integral one-dimensional degree n quadrature formula can be applied to get:

$$\int_{-\infty}^{\infty} \omega(\pmb{x}) \prod_{i=1}^{d} x_i^{n_i} d\pmb{x} = \frac{1}{(2\pi)^{d/2}} \int_{-\infty}^{\infty} \exp(-\pmb{x} \cdot \pmb{x}/2) \prod_{i=1}^{d} x_i^{n_i} d\pmb{x} \tag{A26}$$

$$= \prod_{i=1}^{d} \frac{1}{(2\pi)^{1/2}} \int_{-\infty}^{\infty} \exp(-x_i^2/2) \, x_i^{n_i} dx_i$$

$$= \prod_{i=1}^{d} \left(\sum_{j=1}^{n} w_j x_j^{n_i} \right) = \sum_{k_1=1}^{n} \cdots \sum_{k_d=1}^{n} w_{k_1} \cdots w_{k_d} x_{k_1}^{n_1} \cdots x_{k_d}^{n_d}$$

due to each $n_i \le n$ where w_j and x_j are the Gauss-Hermite quadrature weights and nodes, respectively. By defining the product $w_{k_1 \cdots k_d} = w_{k_1} w_{k_2} \cdots w_{k_d}$ and the vector $\pmb{x}_{k_1 \cdots k_d} = (x_{k_1}, x_{k_2}, \cdots, x_{k_d})$, d-dimensional Gauss-Hermite quadrature formula based on the one-dimensional formula can be written as

$$\frac{1}{(2\pi)^{d/2}} \int_{-\infty}^{\infty} \exp(-\pmb{x} \cdot \pmb{x}/2) \, p(\pmb{x}) d\pmb{x} = \sum w_{k_1 \cdots k_d} p(\pmb{x}_{k_1 \cdots k_d}). \tag{A27}$$

The summation has $q = n^d$ terms that translates into the lattice notation $DdQq$ with the well-known cases $D2Q9$ and $D3$